An investigation into the electronic structure of light-harvesting macrocycles using UV-Vis and MCD spectroscopy as well as DFT and TDDFT computational methods

A THESIS SUBMITTED TO THE FACULTY OF THE UNIVERSITY OF MINNESOTA BY

Hannah Marie Rhoda

IN PARTIAL FULFILLMENT OF THE REQUIREMENTS FOR THE DEGREE OF MASTER OF SCIENCE

Advised by Dr. Victor N. Nemykin

May 2016

Acknowledgements

I would like to thank Dr. Nemykin for all that he has done for me and all the patience and guidance he as granted me. I would also like to thank the entire Nemykin lab for their great support and friendship; I would not have gotten through this program without them. I would also like to thank my family and Casey for all of the unwaivering support they have given me. I can honestly say I would have not gotten through the last two years without any of these peoples support and it means a lot to me that I have it.

Abstract

An electronic structure investigation was done on three separate types of light-harvesting macrocycles using UV-visible (UV-vis) and magnetic circular dichroism (MCD) spectroscopy as well as density functional theory (DFT) and time-dependent DFT (TDDFT) computational methods. The choice of the macrocycle compounds was such that a large range of non-traditional porphyrin analogues was covered including subpthalocyanines, corroles, and reduced porphyrins. It has been found that small changes in structure of these result in large changes in the optical and redox properties of these compounds.

Table of Contents

List of Tables

Chapter Three Tables:

Chapter One Supporting Information Tables:

Supporting information Table 3. TDDFT predicted energies and expansion coefficients for **4d** .

Chapter Two Supporting Information Tables:

Supporting Information Table 1: TDDFT predicted energies and expansion coefficients for **Sample $1H_2$**

Supporting Information Table 2: TDDFT predicted energies and expansion coefficients for **Sample $10H_2$:**

Supporting Information Table 3: TDDFT predicted energies and expansion coefficients for **Sample 8Ni:**

Supporting Information Table 4: TDDFT predicted energies and expansion coefficients for **Sample $9H_2$:**

Supporting Information Table 5: TDDFT predicted energies and expansion coefficients for **Sample $2H_2$:**

Supporting Information Table 6: TDDFT predicted energies and expansion coefficients for **Sample 8Zn:**

Supporting Information Table 7: TDDFT predicted energies and expansion coefficients for **Sample $12H_2$:**

Supporting Information Table 8: TDDFT predicted energies and expansion coefficients for **Sample $11H_2$:**

Supporting Information Table 9: TDDFT predicted energies and expansion coefficients for **Sample $13H_2$:**

Supporting Information Table 10: TDDFT predicted energies and expansion coefficients for **Sample $8H_2$:**

Supporting Information Table 11: TDDFT predicted energies and expansion coefficients for **Sample 11Ni:**

Supporting Information Table 12: TDDFT predicted energies and expansion coefficients for **Sample $5H_2$:**

Supporting Information Table 13: TDDFT predicted energies and expansion coefficients for **Sample 5Ni:**

Chapter Three Supporting Information Tables:

List of Figures

Chapter One Figures:

ligand, see Supporting Information Figure 5. Energy of the second excited state of low intensity is shown as blue vertical bar.

Figure 14: Experimental (top) and TDDFT predicted for hexacoordinated cobalt corrole **3a**. For TDDFT-predicted UV-vis spectra of **3** with different orientations of the axial pyridine ligand, see Supporting Information Figure 6. Energy of the second excited state of low intensity is shown as blue vertical bar.

Figure 15: Experimental (top) and TDDFT predicted for pentacoordinated cobalt corrole **3e**. For TDDFT-predicted UV-vis spectra of **3e - 3g** with different orientations of the axial pyridine ligand, see Supporting Information Figure 7. Energies of the several important excited states of low intensity are shown as blue vertical bars.

Figure 16: Experimental (top) and TDDFT predicted for iron(III) corrole **4a**. For TDDFT-predicted UV-vis spectra of **4** with different orientations of the axial pyridine ligand, see Supporting Information Figure 8. Energies of the several important excited states of low intensity are shown as blue vertical bars.

Chapter Two Figures:

Figure 1: The macrocycle structures of the porphyrinoids indicated; the bold outlines indicate their 18 π-aromatic chromophore

Figure 2: UV-visible and MCD spectra of compounds **$1H_2$** (left) and **$10H_2$** (right)

Figure 3: UV-visible and MCD spectra of compounds **8Ni** (top left), **8Zn** (top right), and **11Ni** (bottom).

Figure 4: UV-visible and MCD spectra of compounds **$2H_2$** (top left), **$12H_2$** (top right), **$11H_2$** (bottom left), and **$9H_2$** (bottom right).

Figure 5: UV-visible and MCD spectra of compounds **$13H_2$** (left) and **$8H_2$** (right).

Figure 6: UV-visible and MCD spectra of compounds **5Ni** (left) and **6Ni** (right).

Figure 7: UV-visible and MCD spectra of compounds **$5H_2$** (top left), **$6H_2$** (top right), and **$7H_2$** (bottom).

Figure 8: UV-visible and MCD spectroscopy of compound **4Zn**.

Figure 23: Experimental (top) and TDDFT (bottom) predicted UV-vis spectra for compounds **5Ni** (left) and **6Ni** (right)

Figure 24: Experimental (top) and TDDFT (bottom) predicted UV-vis spectra for compounds **5H$_2$** (top left), **6H$_2$** (top right), and **7H$_2$** (bottom)

Figure 25: Experimental (top) and TDDFT (bottom) predicted UV-vis spectra for compound **4Zn**

Chapter Three Figures:

Figure 1: Structure of subphthalocyanine and its derivatives used in this paper.

Figure 2: Labeled CAMERON diagrams for X-ray structures of **2** (left) and **4** (right). Hydrogen atoms are omitted for clarity. The thermal ellipsoid probability level is 50%.

Figure 3: ORTEP and MERCURY diagrams for X-ray structure of **4@C$_{60}$**. Hydrogen atoms are omitted for clarity. (**A**) prospective view of the unit cell; (**B**) "concave" 1 : 2 motif; (**C**) one out of three "sitting atop" motifs; (**D**) one out of three fullerene : 2 thiophenol non-covalent interactions motif.

Figure 4: Partial ESI (positive mode) spectra of subphthalocyanine **1** in the presence of C_{60} fullerene.

Figure 5: Partial CSI (positive mode) spectra of subphthalocyanine **1** in the presence of C_{60} and C_{70} fullerenes.

Figure 6: UV-vis (green, top) and MCD (brown, bottom) spectra of compounds **1** (**A**), **2** (**B**), **3** (**C**), and **4** (**D**).

Figure 7: UV-vis (**A**, **C**) and difference (**B**, **D**) spectra of titration of subphthalocyanine **4** with C_{60} (**A**, **B**) and C_{70} (**C**, **D**) fullerenes.

Figure 8: Steady-state fluorescence titration of subphthalocynaine **4** with C_{60} and C_{70} fullerenes.

Figure 9: Transient absorption spectra of subphthalocyanine **4** in toluene. (a) The visible potion of the spectrum. (b) The near-IR portion of the spectrum. (c) A comparison of **4** with the addition of C_{60} at a ratio of 1:10 demonstrating enhancement of the transient

absorption around 1060 nm. The pump-probe delay is 200 ps. The inset shows the ratio of integrated difference signal in the regions 1060-1100 nm to 920-980 nm as a function of pump-probe delay.

Figure 10: Transient absorption of **4** probed at 1160 nm. The fit consists of the sum of a Heaviside function and an exponential rise with a time constant of 1.4 +/- 0.8 ns (confidence interval reported at 68.2%).

Figure 11: DFT-predicted geometries for compounds **1** - **4** and their adducts with C_{60} fullerene.

Figure 12: DFT-predicted energy diagram for individual compounds **1** - **4** and C_{60} fullerene.

Figure 13: DFT-calculated charge density isosurfaces for 1 : 1 (top) and 2 : 1 non-covalent complexes between **1** (**A**), **2** (**B**), **3** (**C**), and **4** (**D**) and C_{60} fullerene.

Figure 14: DFT-predicted frontier orbitals of compounds **1** - **4**, C_{60} fullerene and their non-covalent complexes.

Figure 15: DFT-predicted energy diagram for non-covalent 1 : 1 (left) and 1 : 2 (right) complexes.

Chapter One Supporting Information Figures:

Supporting information Figure 1: DFT predicted MOs for corroles **2a-2c** .

Supporting information Figure 2: DFT predicted MOs for corroles **3a-3d** .

Supporting information Figure 3: DFT predicted MOs for corroles **4a-4d** . Top: a-set; bottom: b-set.

Supporting information Figure 4. Experimental (top) and TDDFT predicted UV-vis spectra of corroles **2a-2c** in cm^{-1} scale**:**

Supporting information Figure 5. Experimental (top) and TDDFT predicted UV-vis spectra of corroles **3a-3d** in cm^{-1} scale**:**

Supporting information Figure 6. Experimental (top) and TDDFT predicted UV-vis spectra of corroles **4a-4d** in cm^{-1} scale**:**

Chapter Two Supporting Information Figures:

Chapter Three Supporting Information Figures:

Chapter One: Combined MCD/DFT/TDDFT Study of the Electronic Structure of Axially Pyridine Coordinated Metallocorroles

SUMMARY:

A series of metallocorroles were investigated by UV-visible and magnetic circular dichroism spectroscopies. The diamagnetic distorted square-pyramidal main group corrole Ga(tpfc)py (**2**), the diamagnetic distorted octahedral transition-metal adduct $Co(tpfc)(py)_2$ (**3**), and paramagnetic distorted octahedral transition-metal complex $Fe(tpfc)(py)_2$ (**4**) [H_3tpfc = tris(perfluorophenyl)corrole] were studied to investigate similarities and differences in the electronic structure and spectroscopy of the closed- and open-shell metallocorroles. Similar to the free base H_3tpfc (**1**), inspection of the MCD Faraday B terms for all of the macrocycles presented in this report revealed that a $\Delta HOMO < \Delta LUMO$ [$\Delta HOMO$ is the energy difference between two highest energy corrole-centered p-orbitals and $\Delta LUMO$ is the energy difference between two lowest energy corrole-centered π^*-orbitals originating from $M_L \pm 4$ and $M_L \pm 5$ pairs of perimeter] condition is present for each complex, which results in an unusual sign-reversed sequence for π - π^* transitions in their MCD spectra. In addition, the MCD spectra of the cobalt and the iron complexes were also complicated by a number of charge-transfer states in the visible region. Iron complex **4** also exhibits a low energy absorption in the NIR region (1023 nm). DFT and TDDFT calculations were used to elaborate the electronic structures and provide band assignments in UV-vis and MCD spectra of the metallocorroles.

Introduction

First discovered in the 1960s,[1] the corrole macrocycle has continued to attract interest for a wide variety of applications due to its unique chemical and physical properties. Corrole (**1**, Figure 1) is a contracted analogue of porphyrin, comprised of four pyrrollic subunits three bridging meso carbon positions, and a direct bipyrrole linkage. The synthesis and modification of free base corroles has been an active area of research.[2] The omission of one carbon atom from the macrocyclic backbone results in a number of structural changes in corrole relative to porphyrin, including a contracted metal binding core and three ionizable NH groups. Although modified from normal porphyrin, corrole retains an aromatic 18-electron annulene ring structure. Accordingly, the UV-visible spectrum has absorption similar to normal porphyrins, with Soret- and Q-band features that can be described using Gouterman's four orbital model.[3,4] However, the electronic and spectroscopic properties of corrole have features that are notably altered from normal porphryins. With free base corroles, such differences include solvent-dependent absorption and emission behavior as well as increased quantum yields of fluorescence.[5]

The metal binding chemistry of corrole has also been an area of intense investigation and the metal complexes of corrole have been used as catalysts,[6] sensors,[7] and heme model complexes.[8] The contracted core and trianionic character of the macrocycle affect how metal ions bind to corrole, especially with regard to stabilizing high-valent oxidation states. Thus, oxidation states +3 and above are typically observed in corroles. Corroles can bind transition metal and main group ions from across the periodic table, and much work has been carried out developing the metalation chemistry

for this macrocycle. Nonetheless, much fundamental chemistry and properties of corrole and corrole metal complexes remain to be investigated.

To our surprise, the magnetic circular dichrosim (MCD) spectroscopy of the metallocorroles is completely unexplored despite the potential for MCD spectroscopy to provide accurate assignment of the optical transitions observed in such complexes. In this report, we present the first study on the MCD spectra of a series of metallocorroles. Previously, we presented the first study of the MCD spectra of free base corrole macrocycles.[9] Since our initial report, there has been one study on the MCD spectroscopy of a phosphorous corrole.[10] For the present study, we used the readily available tris(pentafluorophenyl)corrole (**1**), which can be produced in decent yields[2,11] and the free base corrole has already been investigated by MCD spectroscopy.[9] We have collected MCD spectra from three different systems that reflect part of the diversity of the metal complexes for this porphyrinoid (Figure 1): a diamagnetic main-group distorted square-pyramidal metal corrole (Ga(III), **2**), a diamagnetic distorted octahedral transition-metal corrole (Co(III), **3**), and a paramagnetic distorted octahedral transition-metal corrole (Fe(III), **4**). All three complexes have a central metal ion in a +3 oxidation state and have an identical axial ligand(s) (pyridine). Compound **2** has one axial pyridine, whereas transition metal complexes **3** and **4** have two pyridines bound to the metal ion. In all three metal adducts, we observe sign reverse (positive-to-negative intensities in ascending energy) features in the Soret- and Q-type band regions. This is the opposite trend as seen in normal porphyrins, but similar behavior was observed in free base corroles[9] as well as the porphyrin isomer N-confused porphyrin.[12] This reverse behavior

in the Faraday B terms indicates that the magnitude of the splitting between the corrole-centered π* LUMO and LUMO+1 (originating from M_L ± 5 pair of the perimeter) is greater than that seen for the corrole-centered p HOMO and HOMO-1 (originating from M_L ± 4 pair of the perimeter).[13] Additionally, using TDDFT methods, we were able to probe the degree of participation of the metal orbitals in the Gouterman-type frontier orbitals, which can provide insight into the non-innocent nature of the corrole ligand as well as the effects of d orbital occupancy on the UV-visible spectra of the corroles.

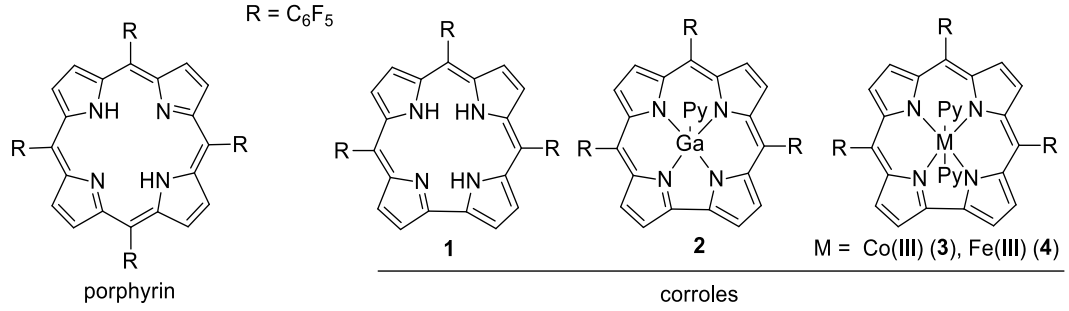

Figure 1. Structures of corroles **1** – **4** and the reference porphyrin macrocycle.

Experimental

Synthesis and Instrumentation. All solvents were purchased from commercial sources and dried using standard approaches prior to experiments. Free-base 5,10,15,25-pentafluorophenyl corrole (**1**) was synthesized as described previously.[2,5,11] The metal complexes **2**, **3**, and **4** were prepared from **1** using published methods. [14]

UV-vis-NIR data were obtained on Jacso V-670 or spectrometer in DCM, pyridine, or toluene as solvents. MCD data were recorded using an OLIS DCM 17 CD spectropolarimeter using a permanent 1.4 T DeSa magnet. The spectra were recorded

twice for each sample, once with a parallel field and again with an antiparallel field, and their intensities were expressed by molar ellipticity per T.[15]

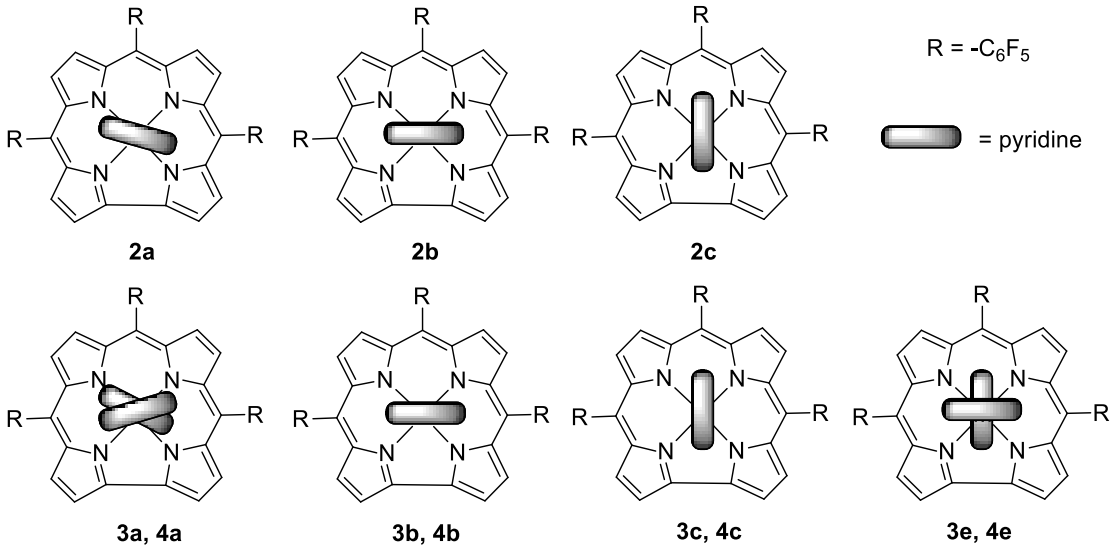

Figure 2. Structures of corroles **2** – **4** used in DFT and TDDFT calculations.

Computational Aspects. All DFT calculations were conducted using the Gaussian 09 software.[16] The starting geometries of the corrole compounds were adopted from the experimental X-ray data; these were optimized at the DFT level using the TPSSh exchange-correlation functional (10% of Hartree-Fock exchange).[17] In the case of gallium corrole **2**, three different geometries were considered (Figure 2): (i) C_1 symmetry without any restrictions (**2a**); (ii) pyridine ligand is parallel to the short corrole C-C bond (C_s symmetry, **2b**); and (iii) pyridine ligand is perpendicular to the short corrole C-C bond (C_s symmetry, **2c**). In the case of cobalt (s = 0, **3**) and iron (s = 1/2, **4**) corroles, four different geometries were considered: (i) C_1 symmetry without any restrictions (**3a** and **4a**); (ii) both pyridine ligands are parallel to the short corrole C-C bond (C_{2v} symmetry,

3b and **4b**); (iii) both pyridine ligands are perpendicular to the short corrole C-C bond (C_{2v} symmetry, **3c** and **4c**); and (iv) one pyridine ligand perpendicular and one pyridine ligand parallel to the short corrole C-C bond (C_s symmetry, **3d** and **4d**). Equilibrium geometries were confirmed by frequency calculations and specifically by the absence of imaginary frequencies. The Wachter's full-electron basis set[18] was utilized for the gallium, cobalt, and iron atoms, while all other atoms were modeled using the 6-31G(d) basis set.[19] For the DFT and TDDFT calculations, solvent effects were calculated using PCM approach[20] and DCM as a solvent. In the TDDFT calculations, the first 60 states were calculated for the cobalt corroles and the first 40 and 80 states were calculated for the gallium and iron corroles, respectively. Molecular orbital contributions were compiled from single point calculations using the QMForge program.[21]

Results and Discussion

UV-Vis and MCD spectra:

The corrole macrocycle can readily bind metal ions, and M(III) complexes are typical for this ligand.[14] The Ga(III) adduct **2** can be produced via reaction of $GaCl_3$ with the free base **1** in pyridine, resulting in a five coordinate complex with a single axial pyridine ligand. The transition metal complexes **3** and **4** are prepared by reaction of $Co(OAc)_2{\cdot}4H_2O$ and $FeCl_2$, respectively, with free base **1** followed by recrystallization in the presence of pyridine. Compounds **3** and **4** have nearly identical structures, with equatorial corrole coordination and two axial pyridines comprising the six coordinate metal ion coordination spheres. As a result of structural similarities for all three metal

adducts, we can directly compare the effect of the identity and spin state of the metal ions on the spectroscopy of corrole.

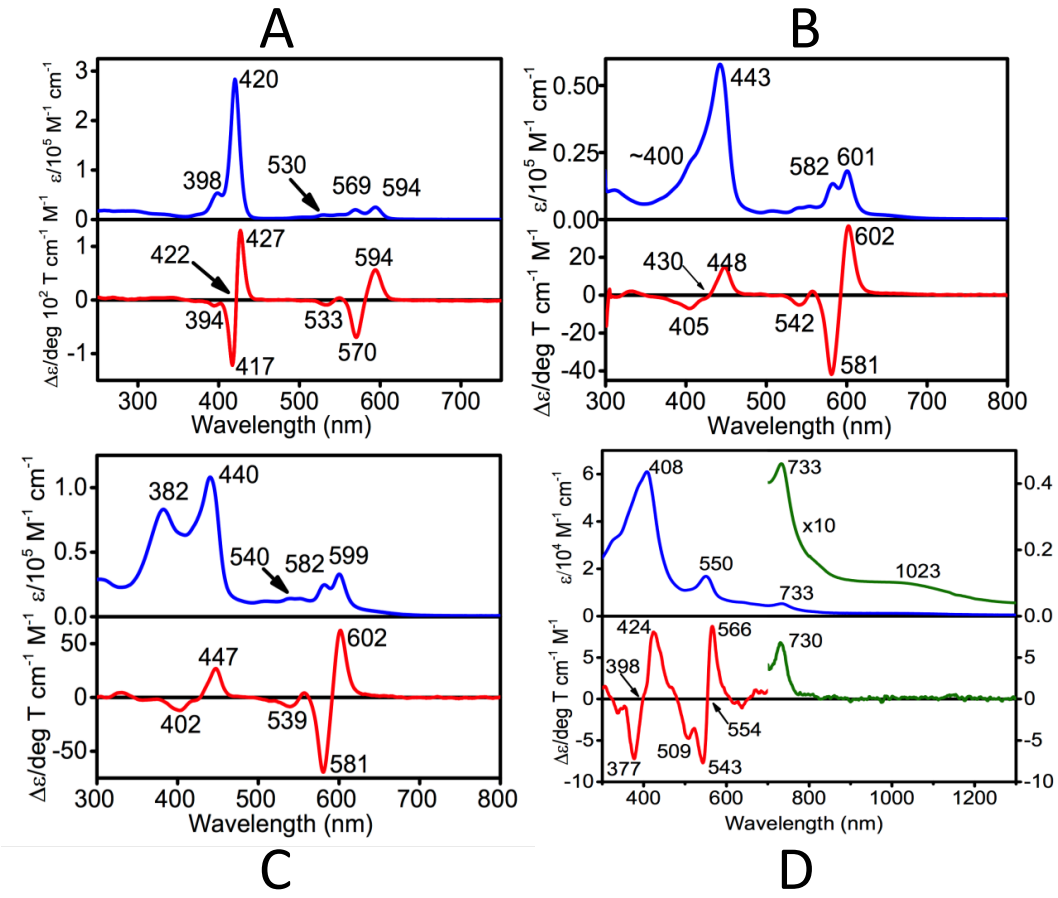

Figure 3. UV-visible and MCD spectra of compounds **2 - 4**. (A): gallium corrole **2** in DCM with a drop of pyridine; (B): cobalt corrole **3** in pyridine; (C): cobalt corrole **3** in DCM; (D): iron corrole **4** in toluene with a drop of pyridine.

In our previous work,[9] we investigated the MCD spectra of free base corroles and were able to deduce from our measurements the relative energy levels and gaps between the frontier orbitals of the 18 electron annulene ring system. The MCD spectra of all so

far studied free-base corroles exhibit what has been considered as unusual sign-reverse (positive-to-negative intensities in ascending energy) features in the Soret- and Q-type band regions[9] similar to those seen in N-confused porphyrin[12] and in a small number of other porphyrinoids.[22] The sign-reverse features, as supported by our calculations, are consistent with an unusual $\Delta HOMO < \Delta LUMO$ relationship between the π and π^* MOs in the corrole ring. The UV-visible spectra, MCD spectra and emission spectra of free base corroles are highly solvent dependent, we have investigated and discussed this aspect of corrole chemistry.[5,9] This solvent dependence is no longer observed upon metalation due to the loss of the internal protons, possible hydrogen bonding with the corrole as well as variable tautomerization states.[9]

The UV-visible and MCD spectra of the three metal complexes of free-base corrole **1** are shown in Figure 3. The gallium corrole **2** exhibits an absorption spectrum with an intense Soret band (420 nm) and three lower intensities Q-type bands at 530, 569 and 594 nm (Figure 1A). The increase in intensity observed in the Q band region is similar to that seen in chlorins and in the external tautomer of N-confused porphyrin.[23,24] However, the spectrum of **2** is also very similar to that observed in normal Ga(TPP)Cl in both the energies of the transitions, the relative intensities of the transition and the number of Q bands.[25] The MCD spectrum of corrole **2** exhibits four strong Faraday B terms in 250 - 700 nm range. A positive Faraday B-term at 594 nm and a negative MCD B-term at 570 nm correlate well with 594 and 569 nm bands observed in the UV-vis spectrum of complex **2**. The Soret band region in the MCD spectrum of complex **2** is dominated by positive and negative MCD B-terms observed at 427 and 417 nm. These

two B-terms form a MCD pseudo A-term centered at 422 nm, which is close to the observed Soret band (420 nm) in the UV-vis spectrum of complex **2**. The positive-to-negative (in ascending energy) sequence of the Faraday B-terms in complex **2** is clearly indicative of a situation when ΔHOMO < ΔLUMO [ΔHOMO is the energy difference between two highest energy corrole-centered p-orbitals and ΔLUMO is the energy difference between two lowest energy corrole-centered π*-orbitals].[13] In the analogous phosphorous complex of a carboxymethylphenyl corrole studied by Kobayashi and co-workers, a similar positive to negative Faraday B term behavior was observed.[10] In the phosphorous corrole and in compound **2**, the decrease in symmetry in the macrocycle backbone removes the degeneracy of the corrole-centered LUMO and LUMO+2, and splits them to a greater degree than the corrole-centered HOMO and HOMO-1 levels.

For the cobalt complex of corrole (compound **3**), Gross and coworkers reported that the six coordinate complex exists in equilibrium with a five coordinate complex at low concentrations of pyridine.[26] Earlier, Murakami and co-workers reported that for the octaalkyl cobalt corroles, low pyridine concentration resulted in aggregation and that dimerization could occur in the Co(II) analogues.[27] We also observed different spectra for **3** in dichloromethane versus pure pyridine (Figures 1B and 1C). In the case of pure pyridine solution, UV-vis and MCD spectra of the low-spin cobalt(III) complex **3** look quite similar to those of gallium analogue **2**, except the complex **3** has lower energies of Q- and B-bands as well as larger bandwidths. Specifically, the Q-band region of the MCD spectrum of **3** is dominated by a positive Faraday B-term at 602 nm and a negative Faraday B-term at 581 nm, which correlate well with UV-vis bands at 601 and 582 nm,

respectively. Similarly, a positive Faraday B-term at 448 nm and a negative B-term at 405 nm dominate the Soret band region of MCD spectrum of complex **3**, which correlate with the most intense absorption band of **3** observed in the UV-vis spectrum. It is interesting to note, however, that in the case of cobalt corrole **3**, the MCD B-terms are more intense in the Q-band region, while in gallium corrole **2** they are more intense in the Soret band region. As in the gallium corrole **2**, we observe strong positive to negative Faraday B terms, which as before indicates a $\Delta HOMO < \Delta LUMO$ configuration in **3**. The UV-vis and MCD spectra of complex **3** in pure DCM are different from those observed in pyridine (Figure 1C). Although Q-band region in pyridine and DCM are almost identical, an additional strong absorption band at 382 nm has been observed in UV-vis spectrum of complex **3** in DCM. This new band is associated with a quite weak MCD signature, which could be consistent either with formation of H-type cofacial dimer similar to those observed in the main-group and transition-metal phthalocyanines[28] or with dissociation of one axial pyridine ligand with formation of the pentacoordinated cobalt corrole complex **3**. In the later case, the new weak MCD band can be associated with a charge-transfer transitions, which are absent in the hexacoordinated corrole **3**. Gross and co-workers[6a,d,e] discussed equilibrium between penta- and hexacoordinated cobalt corroles as a function of solvent. We also have seen a clear disappearance of the band at 382 nm in UV-vis spectrum of cobalt corrole **3** upon titration of DCM solution with pyridine (Figure 4). Moreover, excellent agreement between TDDFT predicted for pentacoordinated cobalt corrole **3** and experimental spectrum of this compound in DCM as well as absence of aggregate peaks in APCI and ESI mass spectra of corrole **3** allowed

us to suggest an axial ligand dissociation as a main reason for observable UV-vis and MCD spectra in DCM. Our proposed reaction chemistry that describes this pyridine-dependent behavior is shown in Scheme 1. In order for such dimerization to occur in the bis(axially) coordinated complex **3**, one of the axial pyridine ligands should dissociate. Although mechanistically, such axial ligand dissociation is trivial, complex **3** is formally a d^6 system, which should be kinetically very inert.[29] Axial ligand dissociation in complex **3** will be explained below on the basis of DFT calculations.

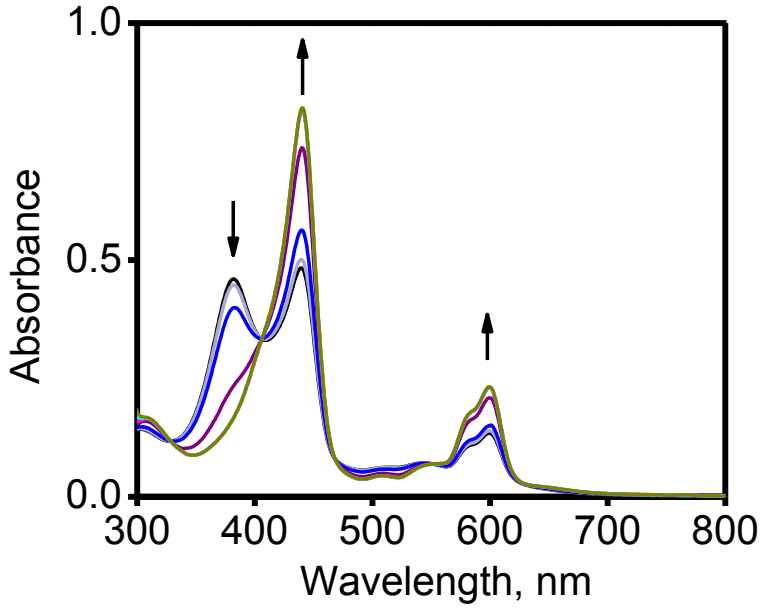

Figure 4. Transformation of the UV-vis spectrum of cobalt corrole **3** in DCM upon stepwise addition (0 - 10 mL) of pyridine.

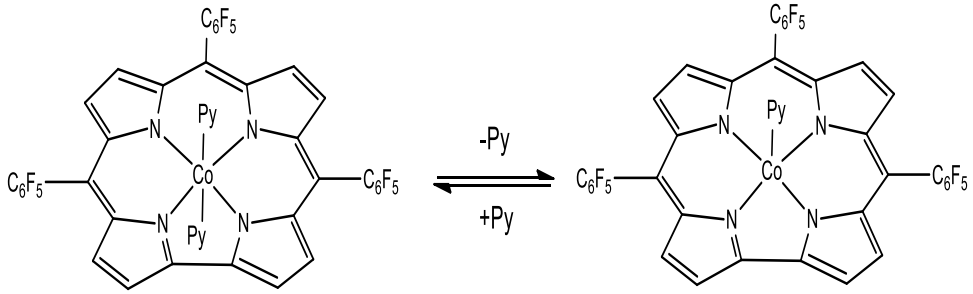

Scheme 1. Proposed transformation of the hexacoordinated cobalt corrole **3** into a pentacoordinated form.

The UV-visible and MCD spectra of the iron complex **4** in pyridine/toluene mixture are strikingly different from free base corroles, the main group corrole **2** or even the diamagnetic transition metal corrole **3**. Gross and co-workers reported that complex **4** exhibits NMR and EPR features that correspond to a low spin (s = ½) Fe(III) metal complex, which is expected for the relatively strong ligand field environment of the trianionic corrole macrocycle and axial pyridines.[26] The features in the UV-visible spectrum are rather broad, with a Soret-type absorption centered at 408 nm, and Q band features at 550 nm and 733 nm. We also observed a very low energy absorption in the near infra-red (NIR) region around 1023 nm, which can be seen in Figure 1D. The same region in the cobalt complex **3** shows no such absorption in the NIR region. However, Fe(III) porphyrins do exhibit low energy ligand to metal charge transfer (LMCT) bands resulting from low spin (s = ½) configurations.[30] The MCD spectrum exhibits features consistent with the UV-vis spectrum of complex **4**. Indeed, the Soret-type band in MCD spectrum of complex **4** is represented by a positive (424 nm) and negative (377 nm) signals centered at 398 nm. The intensity of this feature is close to the intensity of another

pseudo C-term, which is centered at 554 nm and consists of positive (566 nm) and negative (543 nm) B-term components. It is interesting to note that the relatively weak but easily detectable positive Faraday B-term at 730 nm in MCD spectrum of **4** can be clearly associated with the 733 nm band in its UV-vis spectrum, while no clear MCD signal was observed for the 1023 nm band at room temperature even at high concentrations of sample.

DFT and TDDFT Calculations:

To obtain insight into the electronic structures of corroles **2** - **4** and to interpret their observed UV-vis and MCD spectra, we conducted DFT and TDDFT calculations on these systems. In general, the metal complexes of corrole have received much attention from a computational standpoint as a result of their unique reactivities and the observed "non-innocence" of the macrocycle.[31] In particular, calculations have focused on understanding the relationship between the corrole macrocycle and stabilization of the central metal high-valent oxidation states.[31] Several research groups presented DFT calculations on gallium,[32] cobalt(III),[33] and iron(III)[34] corroles, but in many of those calculations pyridine axial ligands were not considered. Although truncation of the axial pyridine ligand can be (to some extent) justified for gallium corrole, axial pyridine ligands should be always considered in the case of cobalt(III) and iron(III) corroles as they directly influence spin state and the energies of the charge-transfer transitions. Having this consideration in mind, we conducted DFT calculations axial pyridine ligand(s). In all cases, DFT predicted geometries are n good agreement with known X-ray

crystal structures for Ga(III) and Fe(III) corroles (Supporting Information Table 1).[35] As discussed below, DFT predicts only small energy differences for different orientations of the axial pyridine ligand(s) thus confirming small rotational barrier for this group. Because of such small rotational barrier, however, one cannot only consider crystallographically observed geometries as in solution axial ligand(s) can adopt variety of orientations. More important, different orientations of the axial pyridine ligand(s) in transition-metal corroles **3** and **4** can easily change the degree of interaction with the metal-centered d-manifold thus changing energies and compositions of the metal-centered MOs. For these reasons all specific orientations of the pyridine ligand(s) in target corroles are discussed below.

There are also two recent TDDFT calculations on the π - π^* transition energies in metal-free[9] and phosphorus-containing[10] corroles. Indeed, we recently presented TDDFT calculations on a series of meso substituted free base corroles, and noted a correlation between the ΔLUMO and ΔHOMO and the sign-reverse features observed in the MCD spectra.[9] The TDDFT calculations that are most relevant to the current work were presented recently by Kobayashi and co-workers on the oxyphosphorous 5,10,15-tris(p-methoxycarbonylphenyl)corrole system.[10] In this report, the unsubstituted phosphorous(V) macrocycle along with the tris(phenyl) and tris (p-methoxycarbonylphenyl) substituted variants were studied. In each case, the same trends were observed as seen in the free base corroles. The ΔLUMO remains larger than the ΔHOMO (resulting in the reverse sign Faraday B terms in the corresponding MCD

spectra), but the presence of the phenyl rings and ester functional groups does increase the ΔHOMO, although not enough to alter the reverse sign Faraday B term.

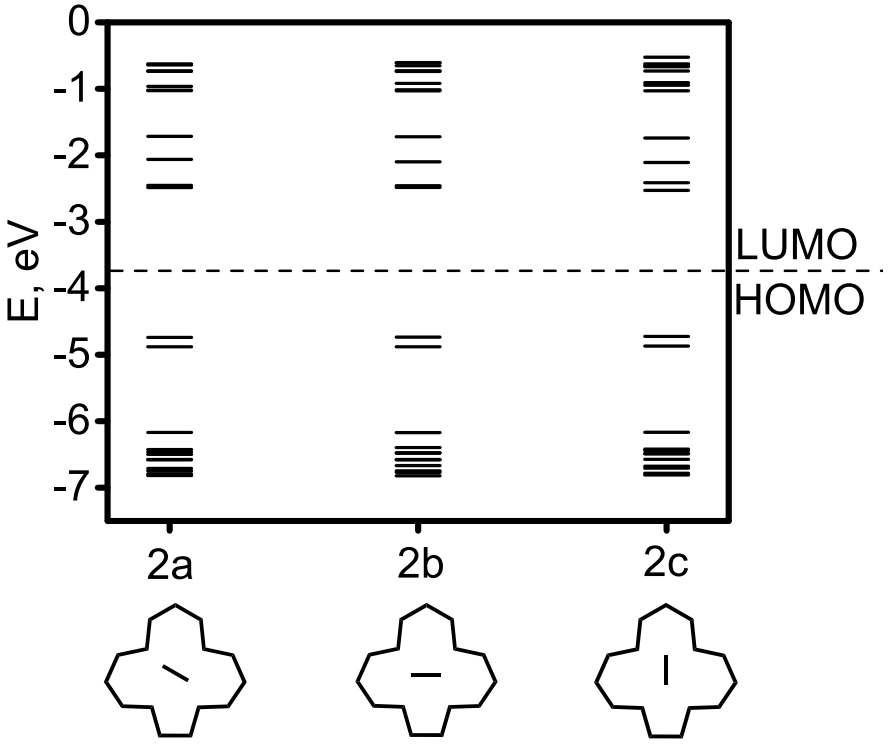

Figure 5. Frontier orbitals energy diagram for gallium corrole **2** predicted at DFT level. The diagrams at the bottom of the chart show the orientations of the pyridine ring with regard to the macrocycle.

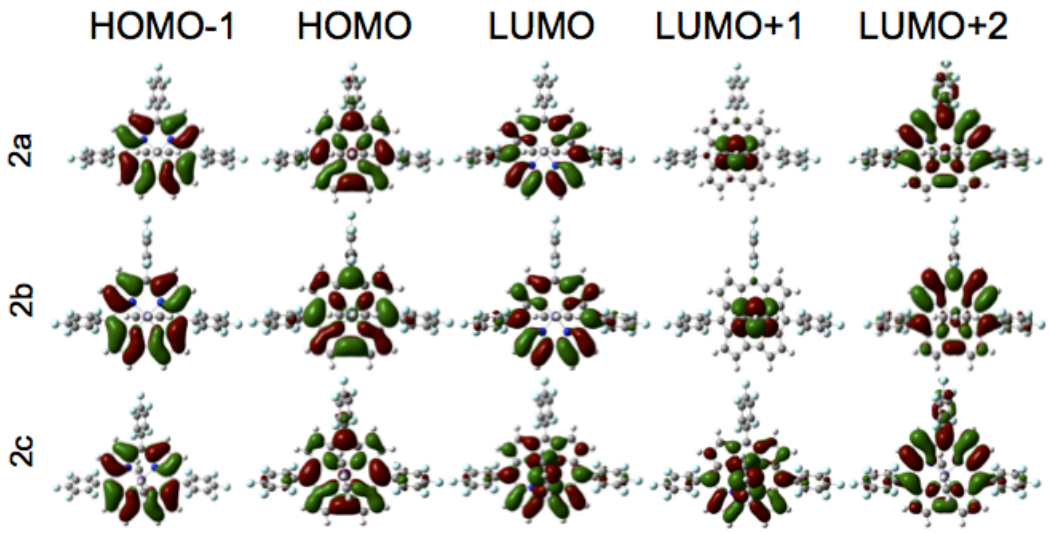

Figure 6. Frontier orbitals for gallium corrole **2** predicted at the DFT level for different orientations of the axial pyridine ligand.

Because of the presence of the closed shell main-group metal ion, it is expected that the electronic structure and properties of the excited states in complex **2** would be the easiest to analyze. Molecular orbital energies for complex **2** with different orientations of the axial pyridine ligand are shown in Figure 5, their profiles are pictures in Figures 6 and Supporting Information Figure 1, while orbital compositions are listed in Supporting Information Table 1. For compound **2**, as a complex with a closed shell main-group metal ion, Ga(III), we expected minimal perturbation caused by the axial pyridine position to the frontier orbital energies and compositions. Geometry optimization without any symmetry restrains results in axial ligand orientation very close to the parallel with respect of the corrole C-C bond (Figure 6). The energy difference between this and the idealized C_s geometry is virtually zero, while the energy of the idealized geometry with the axial pyridine ligand perpendicular to the corrole C-C bond is slightly (0.34 kcal/mol)

higher. As we had surmised, there is little metal orbital involvement in the frontier orbitals of compound **2** (Supporting Information Table 2). The nature of the HOMO and HOMO-1 is very similar for all orientations and correlate well with the previous DFT calculations.[31] In particular, the HOMO is dominated by the contributions from the nitrogen atoms, *meso*-carbon atoms, and the short corrole C-C bonds (Figure 6). Although not identical(because of the lack of one *meso*-carbon), the HOMO resembles, to some extent, Gouterman's a_{2u} type orbital.[4] Similarly, pyrrolic a- and b-carbon atoms are predominant contributors into the HOMO-1 (Figure 6), which resembles, to some extent, Gouterman's a_{1u} type orbital.[4] For the symmetry with parallel pyridine ligand, the LUMO and LUMO+1 both exhibit significant amounts of pyridine ligand character. For the C_1 and the C_s symmetries with pyridine ligand parallel to the corrole C-C bond (**2a** and **2b**), the LUMO and LUMO+2 have π^* character and are dominated by contribution from the corrole core, while the LUMO+1 is primarily pyridine in character. In the case of the perpendicular orientation of the axial pyridine ligand (**2c**), both LUMOs have a large contribution, while LUMO+1 is dominated by the contribution of the axial pyridine ligand (Supporting Information Table 2). The LUMO+2 remains pure corrole-centered orbital. Overall, DFT calculations on complex **2** reveal that the corrole based ΔLUMO (not including the predominantly pyridine-based LUMO+1) is larger (0.385 - 0.423 eV) than the ΔHOMO (0.142 - 0.146 eV), which is in agreement with the reverse sign Faraday B term observation in its MCD spectrum.

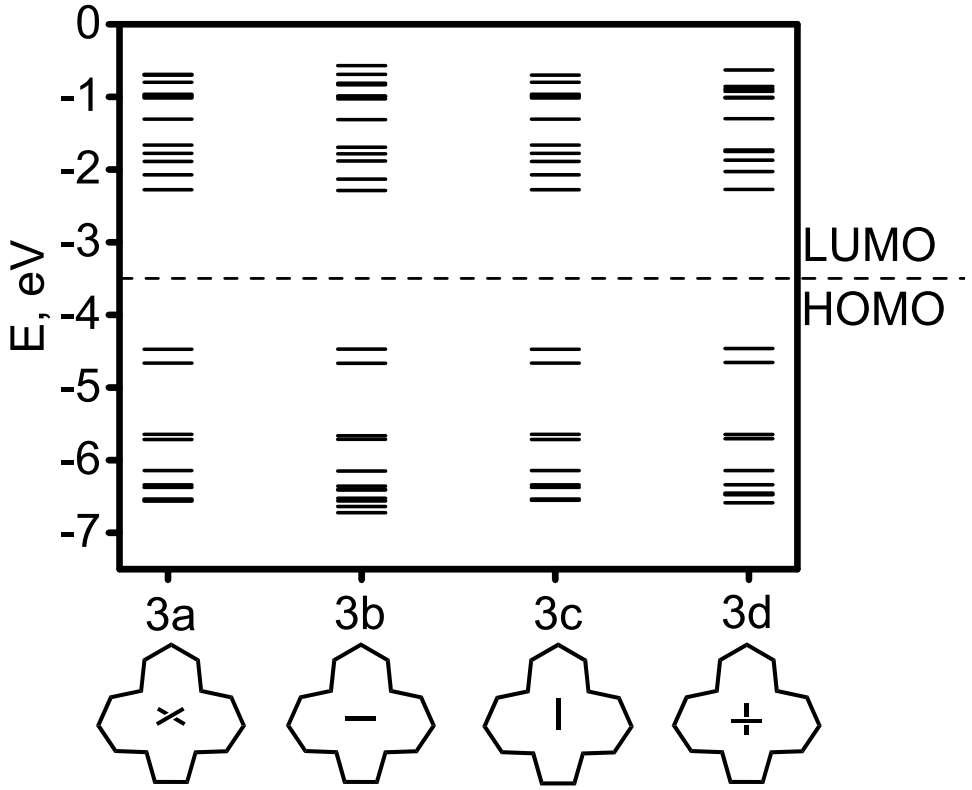

Figure 7. Frontier orbitals energy diagram for cobalt corrole **3** predicted at the DFT level. The diagrams at the bottom of the chart show the orientations of the pyridine rings with regard to the macrocycle.

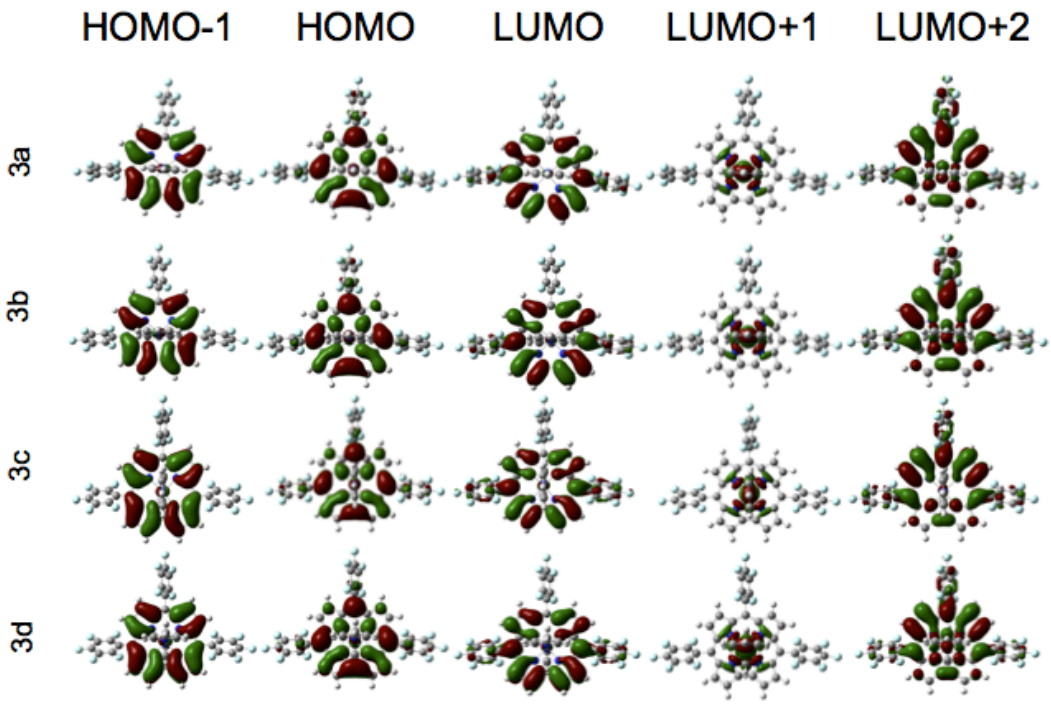

Figure 8. Frontier orbitals for cobalt corrole **3** predicted at the DFT level for different orientations of the two axial pyridine ligands.

In the case of diamagnetic low-spin cobalt corrole **3**, both axial pyridine ligands were used in DFT calculations to mimic an actual ligand field environment around cobalt center. Once again, we calculated four different structures based on the orientations of the pyridine rings: a C_1 symmetry, **3a**, with no geometric restrictions, a C_{2v} symmetry with both pyridine ligands parallel to the short corrole C-C bond (**3b**), a C_{2v} symmetry with the pyridines perpendicular to the short corrole C-C bond (**3c**), and an intermediate C_s symmetry with the pyridine ligands in orthogonal orientations (**3d**). The relative orbital energies for **3a-d** based on their symmetries are shown in Figure 7. The relative energies of **3a** - **3c** are very close to each other, while the energy difference between **3a**

and **3d** is 2.61 kcal/mol. In all cases, the HOMO and HOMO-1 are similar to those observed in gallium corrole **2** (Figure 8). Indeed, nitrogen atoms contribute ~25% into the HOMO, while a- and b-pyrrolic carbons contribute the most into the HOMO-1 (Supporting Information Table 3). Unlike in gallium analogue **2**, cobalt d_{xz} and d_{yz} orbitals have a large contribution into the HOMO-2 and HOMO-3. Again, similar to the gallium complex **2**, the LUMO and the LUMO+2 are predominantly corrole-centered p* orbitals, which used in our ΔLUMO calculations. The LUMO+1 in cobalt corroles **3a-d** has almost equivalent contributions from cobalt d_{z2} orbital and two pyridine axial ligands (Supporting Information Table 3, Figure 8 and Supporting Information Figure 2). Once again our calculations indicate that the ΔLUMO (0.391 – 0.406 eV) > ΔHOMO (0.191 – 0.195 eV) condition occurs in **3**, producing the observed MCD Faraday B terms sequence.

Cobalt(III) corrole complex **3** is formally a d^6 system, which are well-known to be kinetically very stable toward dissociation of ligands.[29] Previous[26,27] and current data on this complex, however, are clearly suggestive of the presence of a non-negligible $L_2Co(tpfc) \rightleftarrows LCo(tpfc) + L$ axial ligand dissociation process in solution. Such axial ligand dissociation can be at least partially explained by the possible presence of a valence isomer in **3**. Indeed, taking into consideration non-innocent redox properties of the corrole ligand, one might expect the presence of two resonance structures for complex **3**: $L_2Co^{III}(tpfc^{3-}) \leftrightarrow L_2Co^{II}(tpfc^{2-})$. The later formally has a d^7 configuration, and would exhibit much higher kinetic mobility of the axial ligand. In order to test such a possibility, we conducted single-point calculation on the $L_2Co^{II}(tpfc^{2-})$ valence isomer using broken-

symmetry calculation approach in which low-spin (s=1/2) cobalt(II) center is antiferromagnetically coupled to the one-electron oxidized corrole ligand. Broken-symmetry calculations resulted in significantly higher energy (~71 kcal/mol) for the $L_2Co^{II}(tpfc^{2-})$ valence isomer. Moreover, optimization of the resulting wavefunction leads to its convergence to the $L_2Co^{III}(tpfc^{3-})$ valence isomer. Although calculated energy differences are expected to have a strong exchange-correlation functional dependence, it seems that the $L_2Co^{III}(tpfc^{3-})$ valence isomer is the only one present in solution, and the question of the increased lability of the axial ligand remains unclear.

For the pentacoordinated cobalt corrole complex, we calculated three different structures based on the orientations of the pyridine rings: a C_1 symmetry, **3e**, with no geometric restrictions, a C_s symmetry with both pyridine ligands parallel to the short corrole C-C bond (**3f**), and a C_s symmetry with the pyridines perpendicular to the short corrole C-C bond (**3g**). During geometry optimization, the C_1 geometry (**3e**) converged close to the C_s symmetry observed for **3f**. The relative orbital energies for **3e-f** based on their symmetries are shown in Figure 9. The relative energies of **3e - 3f** are close to each other with the largest energy difference between **3e** and **3f** is 0.4 kcal/mol. In all cases, the HOMO and HOMO-1 are corrole-centered p-orbitals followed by HOMO-2 and HOMO-3 with a significant contribution from the cobalt d_{xz} and d_{yz} orbitals corrole nitrogen atoms (Supporting Information Table 3, Figure 10). The major consequence of the axial ligand dissociation from the hexacoordinated cobalt corrole is a strong stabilization of the unoccupied cobalt d_{z2} orbital. As a result of such stabilization, the LUMO in pentacoordinated corrole **3** is dominated by the cobalt d_{z2} (~44%) and pyridine

p* (~24%) contributions. The LUMO+1 and the LUMO+3 are predominantly corrole-centered p* orbitals, which used in our ΔLUMO calculations. The LUMO+2 is predicted to be almost pure pyridine centered p* orbital (Supporting Information Table 4, Figure 10 and Supporting Information Figure 3). Once again our calculations indicate that the ΔLUMO (0.381 – 0.393 eV) > ΔHOMO (0.107 – 0.117 eV) condition occurs in pentacoordinated **3e-g**, producing the observed MCD Faraday B terms sequence.

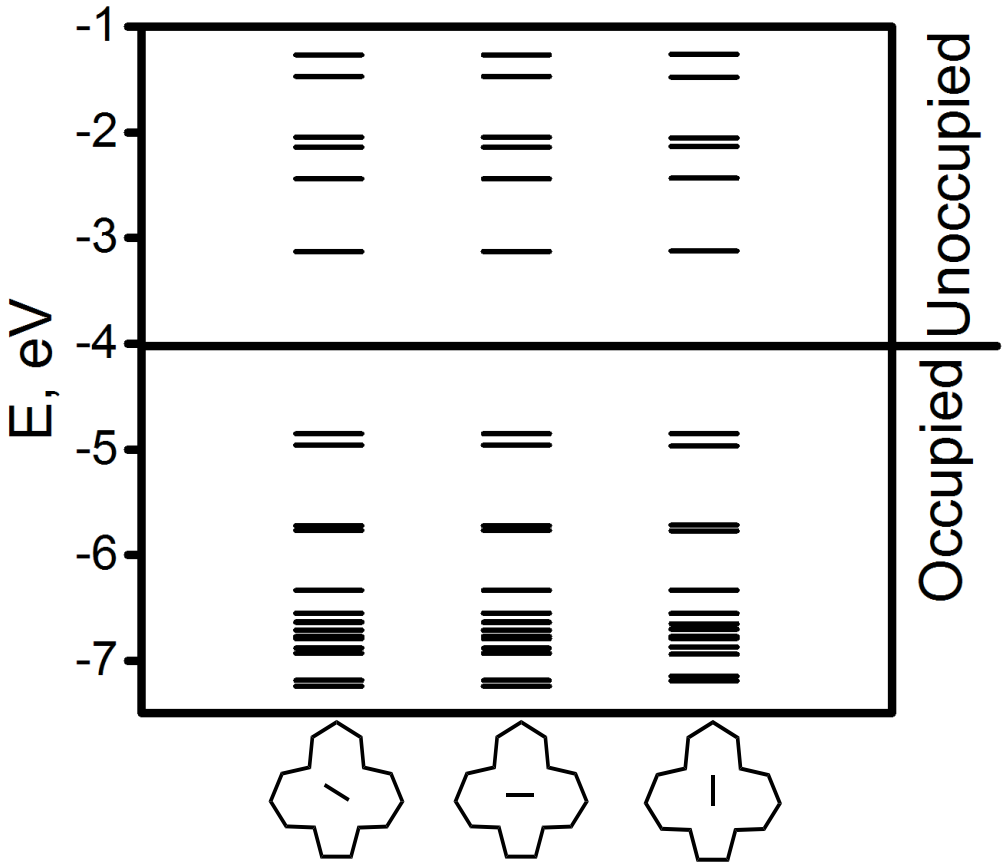

Figure 9. Frontier orbitals energy diagram for pentacoordinated cobalt corrole **3** predicted at the DFT level. The diagrams at the bottom of the chart show the orientations of the pyridine ring with regard to the macrocycle.

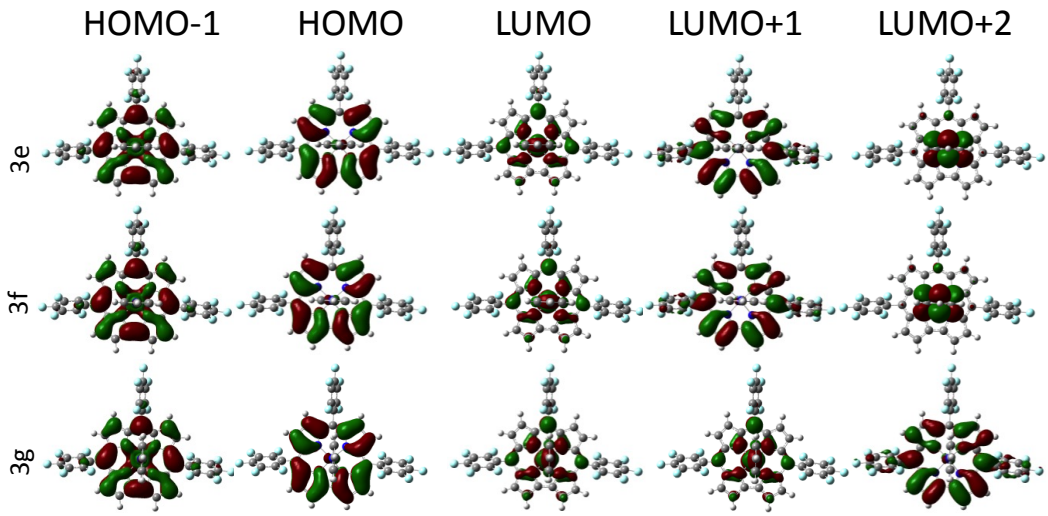

Figure 10. Frontier orbitals for pentacoordinated cobalt corrole **3** predicted ay the DFT level for different orientations of the axial pyridine ligand.

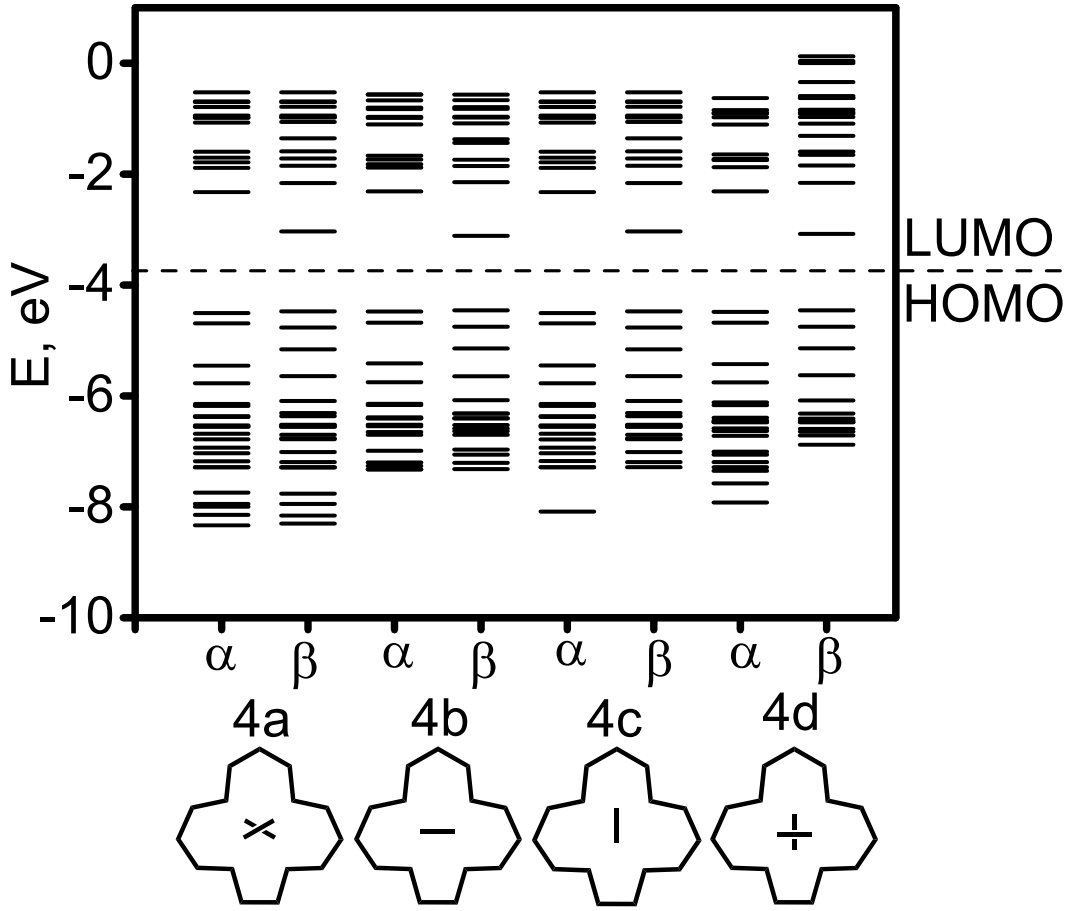

Figure 11. Frontier orbitals energy diagram for iron corrole **4** predicted at the DFT level. The diagrams at the bottom of the chart show the orientations of the pyridine rings with regard to the macrocycle.

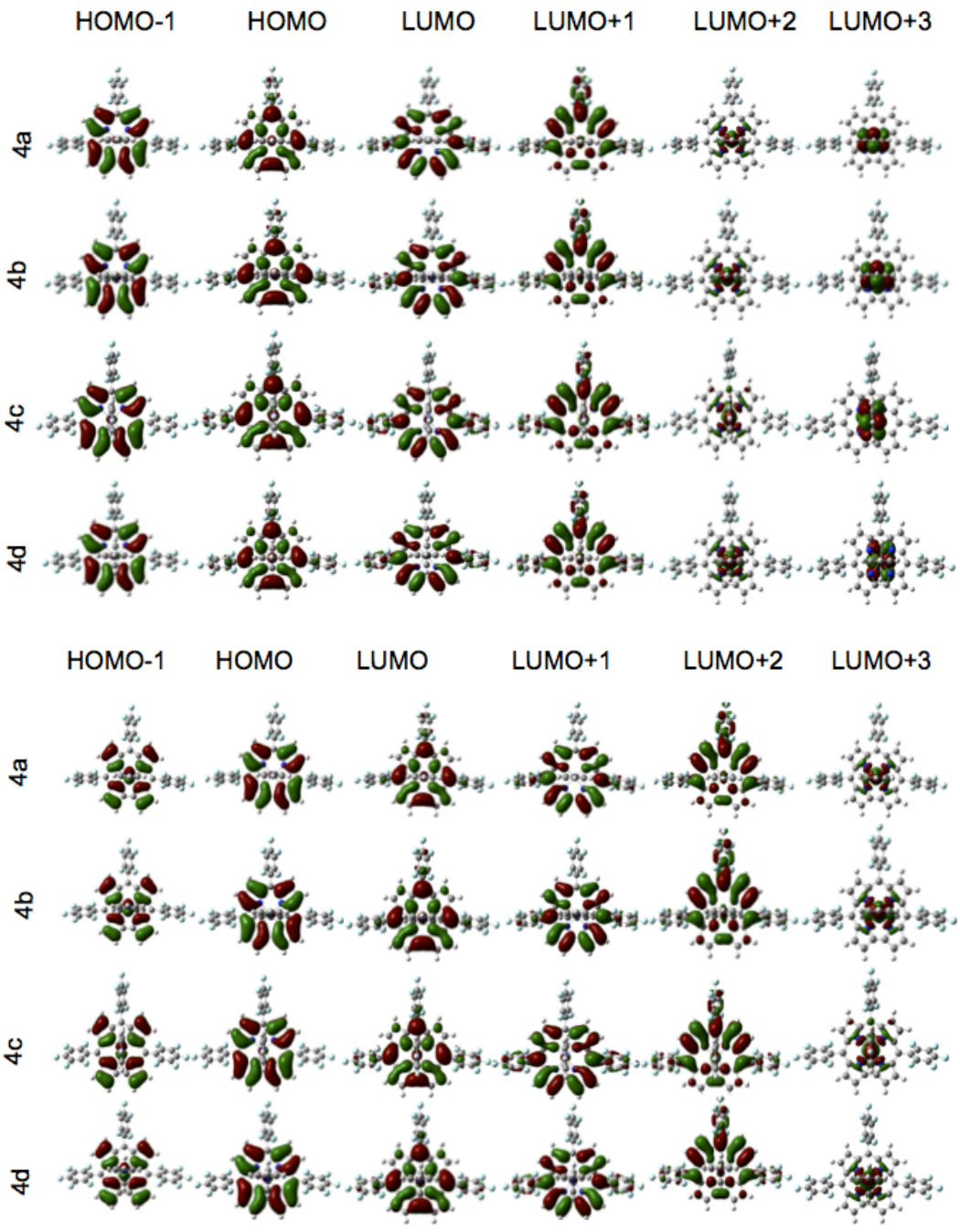

Figure 12. Frontier orbitals (top: a-set; bottom: b-set) for iron corrole **4** predicted at DFT level for different orientations of the two axial pyridine ligands.

For the paramagnetic iron corrole **4**, which is isostructural to the bis-pyridine form of cobalt corrole **3**, we used the same set of the axial pyridine ligands arrangements. Again, the relative energies of **4a** - **4c** are very close to each other, while the energy difference between **4a** and **4d** is 2.01 kcal/mol. The energy diagram of the open-shell molecular orbitals is shown in Figure 11, the relative contributions to the orbitals are shown in Supporting Information Table 5 and their profiles are presented in Figure 12 and in Supporting Information Figure 4. In all geometries of the pyridine ligands, unpaired electron density was found on the central iron atom (Supporting Information Table 5). The a-set of MOs in iron complex **4** is very close to DFT predicted MOs in gallium and cobalt corroles **2** and **3**. Indeed, the HOMO resembles Gouterman's a_{2u} type orbital with substantial contribution from the nitrogen atoms, *meso*-carbon atoms, and the direct pyrrole-pyrrole bond, while the HOMO-1 is dominated by contribution from pyrrolic a- and b-carbons and resembles Gouterman's a_{1u} MO. In addition, HOMO-2 and HOMO-3 have significant iron d_{xz} and d_{yz} character, while HOMO-4 is predominantly an iron-centered d_{xy} orbital. The LUMO and LUMO+1 are similar to the LUMO and LUMO+2 in gallium and cobalt complexes **2** and **3** and are corrole-core centered π^* MOs. In both a- and b-sets of MOs for **4a-d**, the pyridine π^* orbitals are of higher energy than the immediate (LUMO and LUMO+1) frontier orbitals. This is in contrast with the gallium and cobalt corroles **2** and **3** in which pyridine π^* orbitals contribute significantly into the LUMO+1. As expected, the LUMO in the β-set of MOs has significant iron character and the overall spin densities for all possible axial pyridine ligands geometries **4a-d** is clearly suggestive of localization of the unpaired electron on iron center

(Supporting Information Table 5). Again, in all cases **4a-d**, we observe a ΔLUMO (0.431 – 0.438 eV) > ΔHOMO (0.188 – 0.201 eV) relation that is in a good agreement with the MCD experiments.

The electronic structure calculations on corroles **2** - **4** at DFT level suggest two distinct cases. In the first case (gallium corrole **2**), no metal-centered orbitals were predicted in the frontier orbitals region. Thus, it is expected that its UV-vis and MCD spectra could be entirely described by intense π-π* transitions. Taking into account that the LUMO+1 in corrole **2** is dominated by the axial pyridine ligand, expected π-π* transitions could originate either from corrole-to-corrole or corrole-to-pyridine excitations. In the second case (corroles **3** and **4**), metal-centered MOs have significant contribution into frontier orbitals region. Thus, in addition to the mentioned above π-π* transitions, a set of metal-to-ligand and/or ligand-to-metal charge-transfer transitions are expected to appear in their UV-vis and MCD spectra. In order to correlate electronic structure of corroles **2** - **4** with the experimentally observed UV-vis and MCD spectra, we have conducted TDDFT calculations on all possible orientations of axial ligands in complexes **2** - **4**.

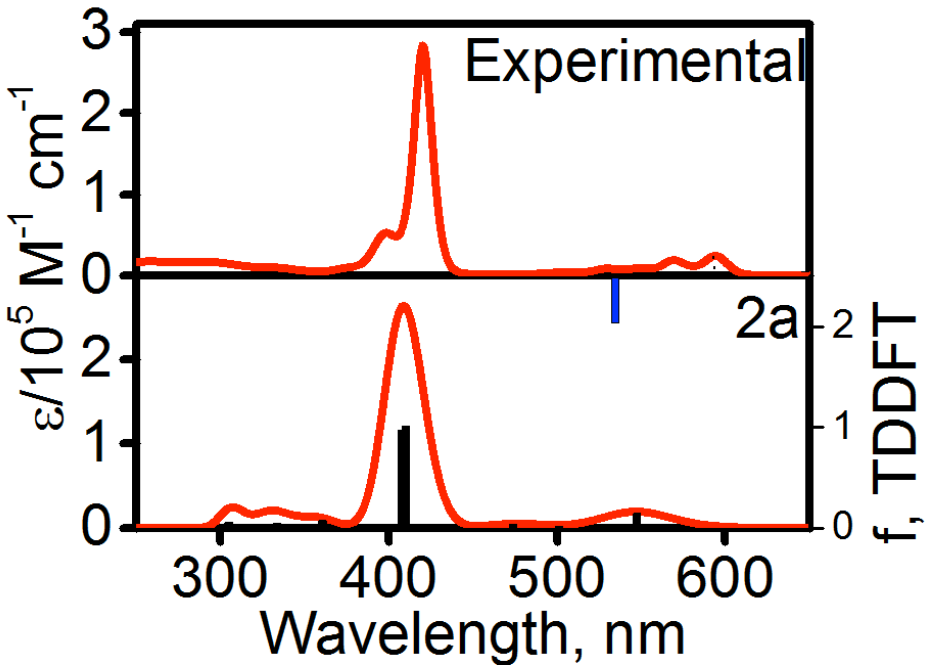

Figure 13. Experimental (top) and TDDFT predicted for gallium corrole **2a**. For TDDFT-predicted UV-vis spectra of **2** with different orientations of the axial pyridine ligand, see Supporting Information Figure 5. Energy of the second excited state of low intensity is shown as blue vertical bar.

As expected, TDDFT predicted UV-vis spectra of corrole **2** (Figure 13 and Supporting Information Figure 5) are dominated by π-π* transitions and predicted excited states energies are almost insensitive to the orientation of the axial pyridine ligand. In general, we observed an excellent agreement between experimental and TDDFT predicted UV-vis spectra of the gallium corrole **2** with the typical TDDFT errors at ~0.1eV level. TDDFT predicts that the whole UV-vis spectrum of gallium corrole **2** can be described by the first six excited states (Supporting Information Table 6). The Q-band region can be described by the first four low intensity excited states. TDDFT predicts

that the first two excited states are dominated by corrole-centered HOMO → LUMO and HOMO-1 → LUMO transitions with a large contribution of the HOMO-1 → LUMO+1 and HOMO → LUMO+1 single electron excitation, respectively. The energy difference between the first and the second excited states are in excellent agreement with the energy difference for the first two low-energy bands in UV-vis and MCD spectra of corrole **2**, although TDDFT predicted intensity of the second band is underestimated. The third and fourth excited states in the visible range predominantly originate from the corrole-centered HOMO → LUMO+2 and HOMO-1 → LUMO+2 transitions, respectively. TDDFT calculations predict that the Soret band region of corrole **2** originates from two excited states (states 5 and 6), which have high oscillator strengths. These two excited states have contributions from the HOMO → LUMO, HOMO-1 → LUMO+2, HOMO-1 → LUMO+2, HOMO → LUMO+2, HOMO → LUMO+1, and HOMO-1 → LUMO+1 major excitations and are π-π* in nature.

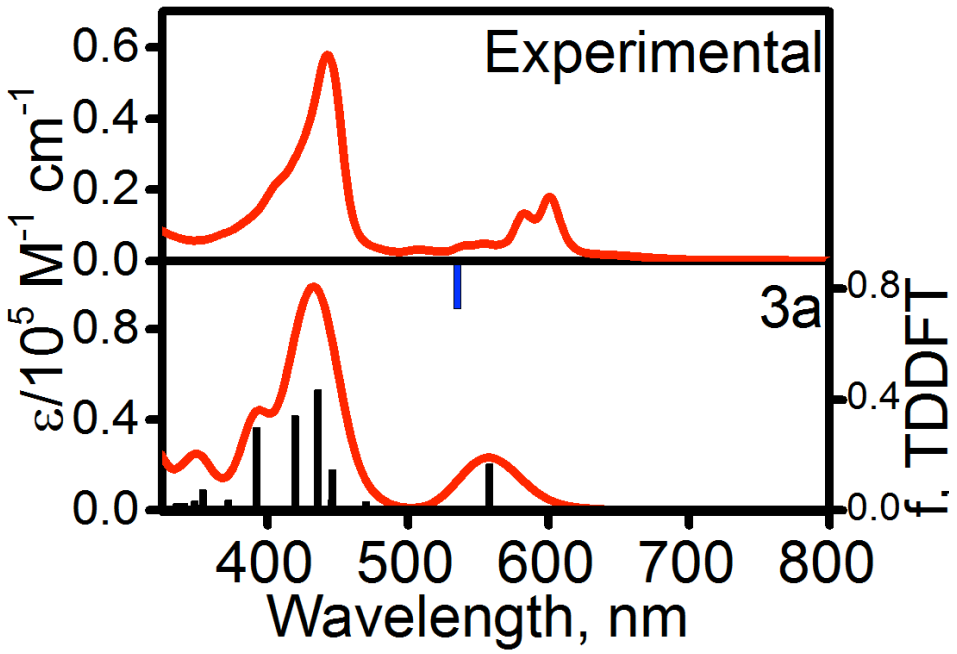

Figure 14. Experimental (top) and TDDFT predicted for hexacoordinated cobalt corrole **3a**. For TDDFT-predicted UV-vis spectra of **3** with different orientations of the axial pyridine ligand, see Supporting Information Figure 6. Energy of the second excited state of low intensity is shown as blue vertical bar.

In the case of the diamagnetic low-spin cobalt(III) corrole **3**, the LUMO+1 orbital is close in energy to the LUMO and has ~40% of cobalt ion and ~40% of the axial pyridine ligands character. Thus, it could be expected that the single-electron excitations from the corrole-centered HOMO and HOMO-1 to LUMO+1 would result in formation of the low-energy excited states with significant LMCT character. Indeed, TDDFT calculations predict that the first two excited states in corrole **3** should be dominated by HOMO → LUMO+1 (excited state 1, 598 nm) and HOMO-1 → LUMO+1 (excited state 2, 577 nm) single-electron transitions and thus, these excited states should have significant LMCT character (Figure 14, Supporting Information Figure 6, Supporting Information Table 7). In addition, TDDFT predicted excited state 5 (483 nm) and excited state 8 (464 nm) are dominated by the single-electron excitations to the LUMO+1 and also have significant LMCT character. According to TDDFT calculations, all of these LMCT states, however, should have a low-intensity. TDDFT predicts that the Q-band region in UV-vis spectrum of corrole **3** should be dominated by the intense π- π* transition (excited state 3), which has the prominent corrole-core centered HOMO → LUMO character. This p-p* transition is closely followed by less intense π-π * band originating from the HOMO → LUMO+2 and HOMO-1 → LUMO excitations. The

energy difference between these two excited states is in good agreement with the energies and energy differences of two most intense bands experimentally observed in Q-band region of complex **3**. In addition, four low-intensity bands at 481, 480, 448, and 447 nm with corrole-to-pyridine charge transfer character were also predicted in the Q-band region of complex **3**. TDDFT predicts that most of the Soret band intensity in UV-vis spectrum of corrole **3** should originate from two predominantly π - π* transitions (excited states 12 and 13), which have large contributions from single-electron excitations involving corrole-centered HOMO, HOMO-1, LUMO, and LUMO+2. The energies and intensities of these excited states have clear dependence on orientation of the axial ligands (Supporting Information Figure 6). The general agreement between TDDFT predicted and experimental UV-vis spectra of corrole **3** is very good and explains a slightly broader absorption in UV and visible regions.

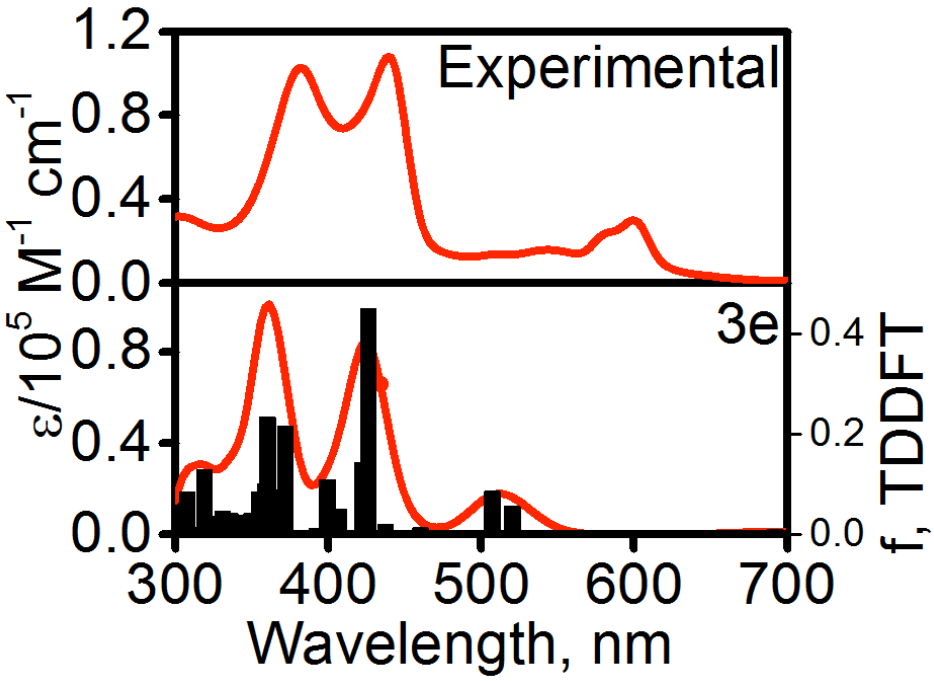

Figure 15. Experimental (top) and TDDFT predicted for pentacoordinated cobalt corrole **3e**. For TDDFT-predicted UV-vis spectra of **3e - 3g** with different orientations of the axial pyridine ligand, see Supporting Information Figure 7. Energies of the several important excited states of low intensity are shown as blue vertical bars.

In the case of pentacoordinate cobalt corrole **3**, TDDFT predicts four low-intensity LMCT from predominantly corrole-centered π-orbitals to LUMO (excited states 1 – 4). According to our TDDFT calculations, two major transitions contribute in the visible region intensity (excited states 5 and 6), which are predominantly associated with corrole-centered π - π* single electron excitations from HOMO or HOMO-1 to LUMO+1 (Figure 15, Supporting Information Figure 7, and Supporting Information Table 8). Unlike in the hexacoordinate complex, both of these transitions have reasonable intensities and correlate well with two transitions observed in the visible region in DCM solution of corrole **3**. In addition, two other, almost independent of the axial ligand orientation, prominent absorption profiles were predicted by TDDFT in 400 – 450 nm and 350 – 380 nm regions (Figure 15, Supporting Information Figure 7, Supporting Information Table 3). The first region is dominated by excited states 11 and 12, which are very similar in composition to those observed in the hexacoordinate cobalt analogue. The second region (350 – 380 nm) is dominated several excited states (excited states 15, 20, 24, and 25), which mostly originate from the LMCT and MLCT single-electron transitions. This region is close to the experimentally observed additional band in UV-vis

spectrum of cobalt corrole **3** recorded in DCM, while its charge-transfer nature can explain the weak MCD signal associated with this experimental band.

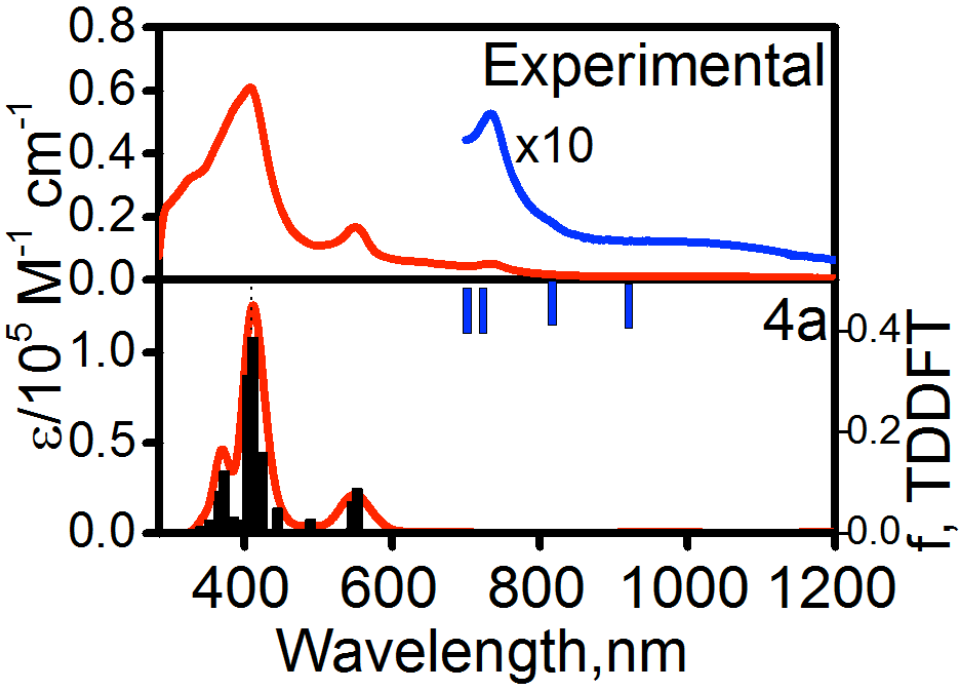

Figure 16. Experimental (top) and TDDFT predicted for iron(III) corrole **4a**. For TDDFT-predicted UV-vis spectra of **4** with different orientations of the axial pyridine ligand, see Supporting Information Figure 8. Energies of the several important excited states of low intensity are shown as blue vertical bars.

The open-shell electronic structure of the iron corrole **4** allows low-energy transitions from corrole-centered MOs to the half-filled iron-centered orbital as well as low energy transitions with significant d-d character. In agreement with these expectations, the first two excited states are predicted to have very low energies, near

zero intensities, and significant d-d character (Figure 16, Supporting Information Figure 8, Supporting Information Table 9). The first two non-zero intensity excited states predicted by TDDFT (excited states 3 and 4) were calculated close to the experimentally observed 1023 nm band and could be assigned to the transitions with significant LMCT character. Next, TDDFT predicted two low-intensity excited states (excited states 6 and 7) with predominant π- π^* character, which correlate well with the experimentally observed band at 733 nm. In addition, two more intense excited states 10 and 11 predicted by TDDFT at 553 and 546 nm also have predominant π - π^* character and correlate very well with the experimentally observed band at 550 nm associated with positive and negative MCD B-terms at 566 and 543 nm, respectively. TDDFT predicts 36 excited states in the 415 and ~2000 nm range, which correlate well with the general broad character of the UV-vis and rich character of the MCD spectra of corrole **4**. In the Soret band region of iron corrole **4**, TDDFT predicts two intense predominantly π - π^* transitions calculated at 411 and 405 nm, which correlate well with UV-vis maximum at 408 nm. Similar to hexacoordinated cobalt corrole **3**, TDDFT predicted transitions in the Soret band region of iron(III) corrole 4 have small dependence on the axial ligands orientation (Supporting Information Figure 8). Overall correlation between experimental UV-vis spectrum of corrole **4** and TDDFT predicted spectra of **4a-d** is excellent (Figure 16).

Conclusions

In our initial report on the magnetic circular dichroism of free base corroles, we showed that these macrocycles exhibit both similarities and differences from normal free base porphyrins. The metallocorroles exhibit similar similarities and differences from the metalloporphyrins and their electronic structures can be understood via Gouterman's four orbital model. Similar to the free base H_3tpfc (**1**), inspection of the MCD Faraday B terms for all of the macrocycles presented in this report revealed that the same $\Delta HOMO < \Delta LUMO$ condition is present for each complex, which results in sign-reversed sequence for π - π * transitions in their MCD spectra. In addition, the MCD spectra of the open d shell cobalt and the iron complexes **3** and **4** were also complicated by dynamics in solution and by the number of the charge-transfer states in visible region. For the cobalt complex **3**, we observed spectra that are dependent on the concentration of pyridine in solution; at low pyridine concentrations we hypothesize that both penta- and hexacoordinate cobalt corroles exist in solution. Additionally, the iron complex **4** exhibits a low energy absorption in the NIR region (1023 nm) similar to those seen in Fe(III) porphyrin systems. DFT and TDDFT calculations were used to elaborate the electronic structures and provide band assignments in UV-vis and MCD spectra of metallocorroles. These calculations showed that there is a significant degree of d orbital involvement in the frontier orbitals for the open d shell corroles **3** and **4**. We are continuing our investigations into porphyrin and phthalocyanine analogs and the relationships between modifications to the macrocycle backbone and electronic structure.

Chapter Two: Magnetic Circular Dichroism Spectroscopy of meso-Tetraphenylporphyrin-derived Hydroporphyrins and Pyrrole-modified Porphyrins

SUMMARY:

A large set of free base and transition metal 5,10,15,20-tetraphenyl substituted chlorins, bacteriochlorins, and isobacteriochlorins, and their pyrrole-modified analogues were investigated by combined UV-visible spectroscopy, Magnetic Circular Dichroism (MCD), Density Functional Theory (DFT), and time-dependent DFT (TDDFT) approaches and compared to the spectral characteristics of the parent compounds, free base tetraphenylporphyrin **$1H_2$** and chlorin **$2H_2$**. It was shown that the nature of pyrroline substituents in the chlorin derivatives dictates their specific UV-vis and MCD spectroscopic signatures. In all hydroporphyrin-like cases, MCD spectroscopy suggests that the Δ HOMO is smaller than the Δ LUMO for the macrocycle-centered frontier molecular orbitals. DFT and TDDFT calculations were able to explain the large broadening of the UV-vis and MCD spectra of the chlorin diones and their derivatives compared to the other hydroporphyrins and hydroporphyrin analogues. The study contributes to the further understanding of the electronic effects of replacing a pyrrole in porphyrins by pyrrolines or other five-membered heterocycles (oxazoles and imidazoles).

Introduction

Porphyrins and hydroporphyrins–chlorins, bacteriochlorins, and isobacteriochlorins (Figure 1) are key members of the 'pigments of life'.[1] They are named thusly because of the crucial roles they play in the metabolism in all kingdom of life: For instance, the iron porphyrin-based heme proteins are ubiquitously found in electron and oxygen transport chains, oxygen storage and activation, or in peroxide deactivation. The iron complexes of isobacteriochlorins are the prosthetic groups in bacterial multi-electron reduction enzymes, the sulfite and nitrite reductases.[2,3]

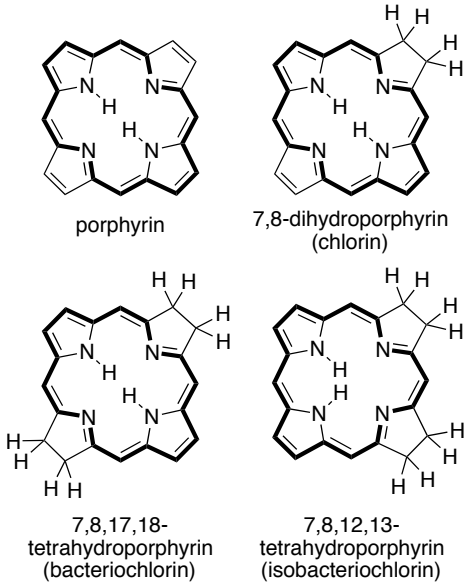

Figure 1: The macrocycle structures of the porphyrinoids indicated; the bold outlines indicate their 18 π-aromatic chromophore

Most prominently, algae and higher plants utilize the green magnesium complexes of chlorins, the chlorophylls, as their key light harvesting pigments.[4] Light-harvesting is not limited to chlorins, however, as the light-harvesting chromophores of phototrophic purple bacteria, heliobacteria, or sulfur bacteria are bacteriochlorin magnesium complexes.[5]

Multiple other roles of porphyrins and hydroporphyrins are known, spanning their use as colorants, sex differentiating hormone, to cytotoxins, while the role of others remain unkown. [6-8]

The natural functions of the porphyrins and hydroporphyrins have long inspired their study, though the knowledge about these compounds is uneven. Porphyrins and the chlorophylls are very well studied, but much less is known about bacteriochlorins and isobacteriochlorins.[9] The general electronic structure of the porphyrinoids can be rationalized using Gouterman's four-orbital model.[10]

Porphyrins and porphyrin analogues also found numerous technical and biomedical applications, some of which utilize the porphyrin in a biomimetic fashion (catalysis, light-harvesting),[11-13] but many also found uses outside of natural precedents (photodynamic therapy, molecular memories, fluorescent and photoacoustic imaging dyes).[14-18] Thus, diverse methods toward synthetic hydroporphyrins were reported.[19-21] The conversion of a porphyrin, such as *meso*-tetraphenylporphyrin (**$1H_2$**) to the parent chlorin **$2H_2$** by reduction is possible (Scheme 1), but such unsubstituted chlorins are often unstable with respect to their oxidation back to porphyrins.[22,23] The OsO_4-mediated dihydroxylation of **$1H_2$** generates a the more stable dihydroxychlorin **$3H_2$**; coordination with Zn^{2+} or Ni^{2+} furnishes its zinc and nickel complexes **3Zn** and **3Ni**, respectively.[24] Reduction of **3Zn** generates regiospecifically the dihydroxyisobacteriochlorin zinc complex **4Zn**.[25,26]

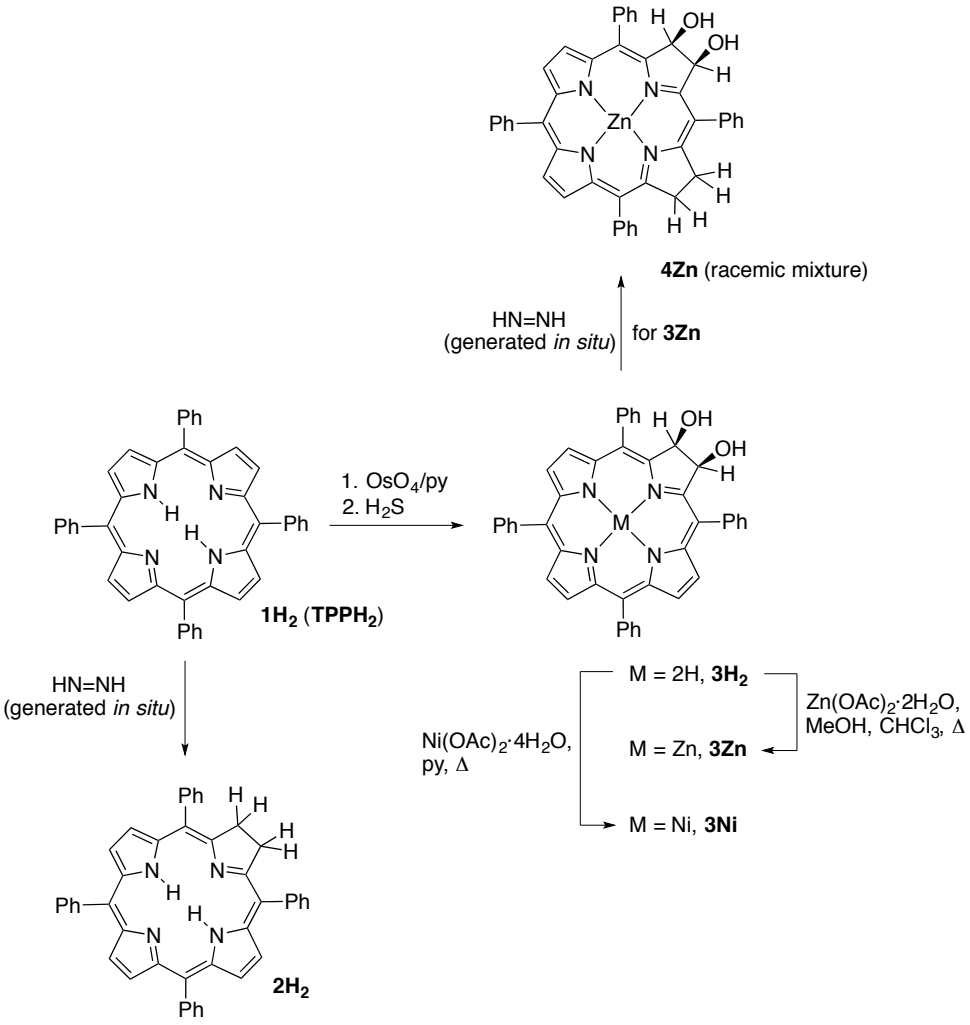

Scheme 1. Synthesis of the chlorin and isobacteriochlorin used in this study.

Importantly, in all of the known porphyrins and hydroporphyrins, including their degradation products,[27] no non-pyrrolic moieties are found, hinting at the particular stability of the tetrapyrrolic porphyrinoid architecture. However, many applications require a fine-tuning of the optical properties of the porphyrinoids used, giving rise to a large effort in the synthesis of porphyrin analogues containing, for example, more than four pyrroles in a macrocyclic arrangement. One particularly class of porphyrin analogs

that are structurally similar to porphyrins and chlorins are the pyrrole-modified porphyrins, chromophores in which one or two of the pyrroles (or pyrrolines) were replaced by non-pyrrolic heterocycles.[28,29]

While many of them are accessible through total synthesis approaches, a large variety of *meso*-tetraphenyl-substituted and b-substituted porphyrin derivatives or pyrrole-modified porphyrins can be made by step-wise functionalization of dihydroxychlorins, utilizing the diol functionality as a synthetic handle (Scheme 2).[29] Thus, oxidation of diols **3H$_2$** or **3Ni** formed the corresponding diones **5H$_2$** or **5Ni**,[30] respectively, that can be converted to mono- (**6H$_2$** and **6Ni**) or bis-oximes (**8H$_2$**).[31] Treating diols **3M** with a different oxidant, MnO_4^-, results in the excision of a carbon from the chlorin framework and the formal replacement of the b,b'-carbon bond by a lactone moiety (**8M**).[32] Other oxidative conditions also generate porpholactones from a variety of porphyrins.[3334] Free base lactone **8H$_2$** can be converted to lactam **9H$_2$** in two steps, while this can be dehydrated/halogenated to the chloro-imidazoloporphyrin **10H$_2$**.[35] Oxidation of diol **3Ni** with $Pb(OAc)_4$ leads to the formation of an intermediate secochlorin bisaldehyde that may undergo, under strongly basic conditions, an intramolecular Cannizarro reaction,[36] followed by loss of CO_2 and oxidative ring closure, forming an oxazolochlorin hemiacetal.[37] This can be readily converted to the oxazolochlorin acetal **11Ni**.[32] The same framework structure, as its free base **11H$_2$**, can be generated from the free base lactone **8Zn**, by reduction, metal removal, and acetalization with MeOH.[32] Porpholactone **8Zn** is also susceptible to alkylation reactions using Grignard reagents.[38] Bisalkylation leads to, for example, the formation of oxazolochlorin **12H$_2$** carrying a b-*gem*-dialkyl group

known to stabilize a chlorin against oxidations. Alkyl addition to the lactone **8Zn**, followed by acetalization, generates an intermediate that can be, like regular chlorins, regiospecifically dihydroxylated at the pyrrole opposite the pyrroline (or, here, the oxazole).[39] This diol can then be oxidized using MnO_4^-, generating pyrrole-modified porphyrin $\mathbf{13H_2}$ in which two pyrroles were replaced by oxazole/oxazolone moieties.[39]

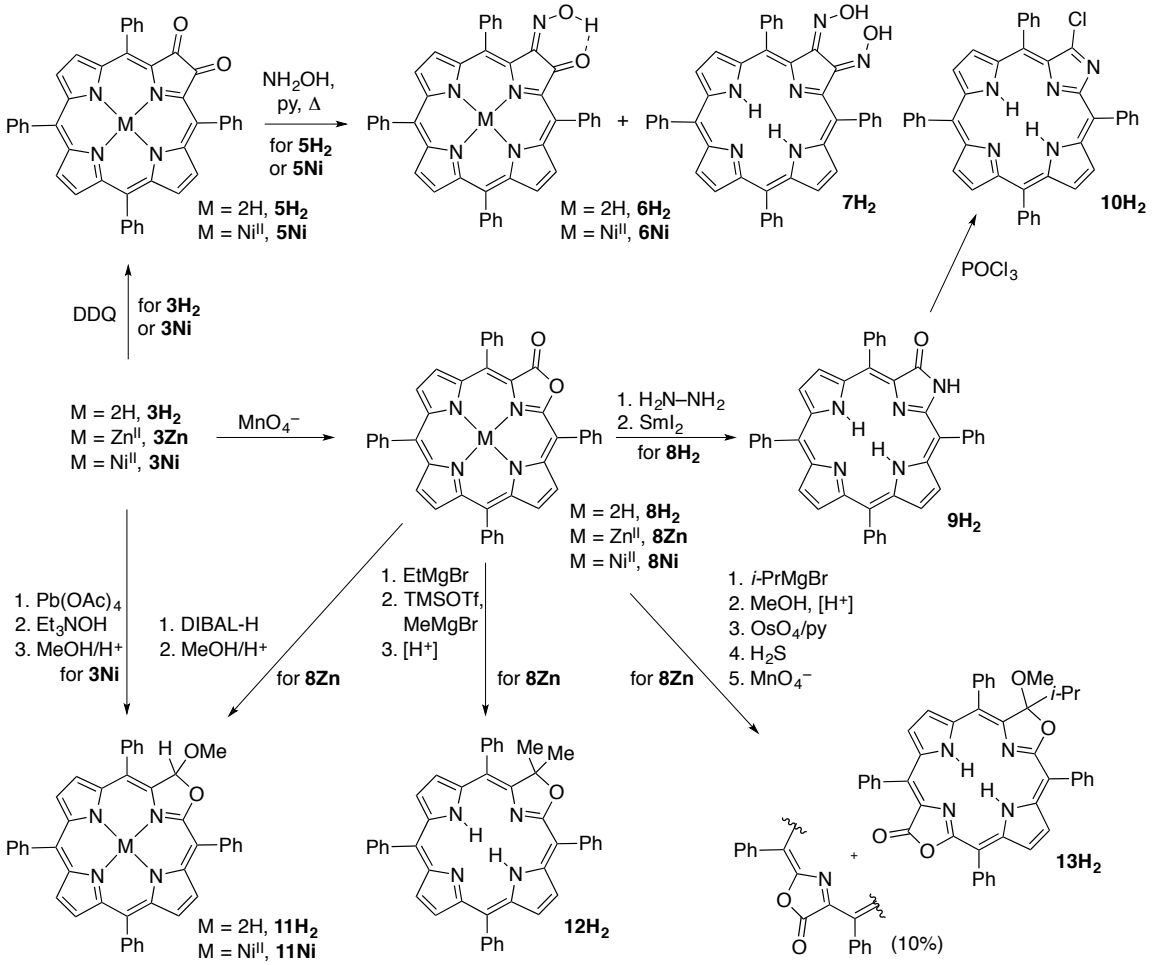

Scheme 2. Synthesis of the porphyrin and chlorin analogues used in this study by transformation of chlorin diol **3**H

Traditionally, in cases where all b-carbons are sp^2-hybridized, the compound is classified as a porphyrin; if an sp^3-carbon is present, a chlorin is formed (Figure 1). However, as will be detailed below, this simple metric often succeeds in predicting their optical properties but also fails frequently. In general, little is known about the electronic properties of pyrrole-modified porphyrins.[32,40,41] The ability to stepwise modulate their chromophores makes them ideal objects for systematic investigations on the role of the b,b'-functionalities on the electronic structure of porphyrinoids.

Quite often, the UV-vis spectra of reduced porphyrins looks very similar to the corresponding porphyrin systems. This makes it extremely difficult to evaluate the differences in their electronic structures. The MCD spectroscopy, on the other hand, is very sensitive to the perturbation of the macrocyclic π-system and thus can be used for investigation of the differences in electronic structures between reduced porphyrins and corresponding porphyrins.[42] Curiously, despite the large progress of the research on the reduced porphyrins and their analogues, the number of reports on the MCD spectroscopy and the electronic structure of these systems is very limited.[43] Following the perimeter model, in application to the reduced porphyrins, one might expect that the MCD spectra would produce a negative signal for the MCD Faraday B-term for the lowest energy transition if the Δ HOMO is larger than Δ LUMO (Δ HOMO is the energy between the two highest energy occupied porphyrin-centered orbitals and Δ LUMO is the energy difference between the two lowest unoccupied porphyrin-centered orbitals).[44]

We present in this contribution a systematic study on the electronic structures of a series of chlorins and porphyrin- and chlorin-like porphyrinoids in reference to the parent

porphyrin **1H$_2$** using MCD spectroscopy and time-dependent DFT (TDDFT) calculations. The choice of chromophores investigated was to cover a swath of structural variety among porphyrinoids containing four five-membered moieties in a porphyrin-like arrangement that are either known or strongly suspected to be essentially planar. Porphyrinoids **5H$_2$**, **6H$_2$**, **7H$_2$**, **8M**, **9H$_2$**, **10H$_2$** possess all sp^2-hybridized b-carbons, that would put them into porphyrin categories. However, dione **5H$_2$** or particularly its oximes **6H$_2$** and **7H$_2$** containing sp^2-hybridized b-carbons are more chlorin-like.[31] Also, the spectra classification of some classes may change with metallation, as is for the case of the porpholactones **5M**; the free base is porphyrin-like while the metal complexes are metallochlorin-like.[32] Other porphyrinoids, such as **11M**, **12H$_2$** are UV-vis spectroscopically and by architecture clearly chlorin-like. Likewise, compound **4Zn** is an unambiguous metalloisobacteriochlorin.[25] Bis-modified chromophore **13H$_2$** was classified as a chlorin, with the oxazole moiety mimicking a pyrroline and the oxazolone moiety mimicking a pyrrole moiety.[39] Again, we were interested in better understanding the electronic structures of these chromophores and hypothesized that MCD spectroscopy would provide a deeper insight into the classifications of these chromophores. As we will show below, this proved to be indeed the case.

Results and Discussion

UV-vis and MCD spectra

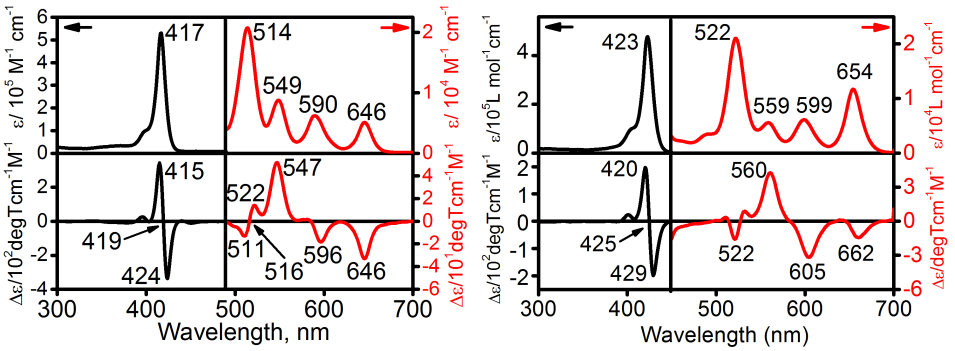

Figure 2: UV-visible and MCD spectra of compounds **1H$_2$** (left) and **10H$_2$** (right)

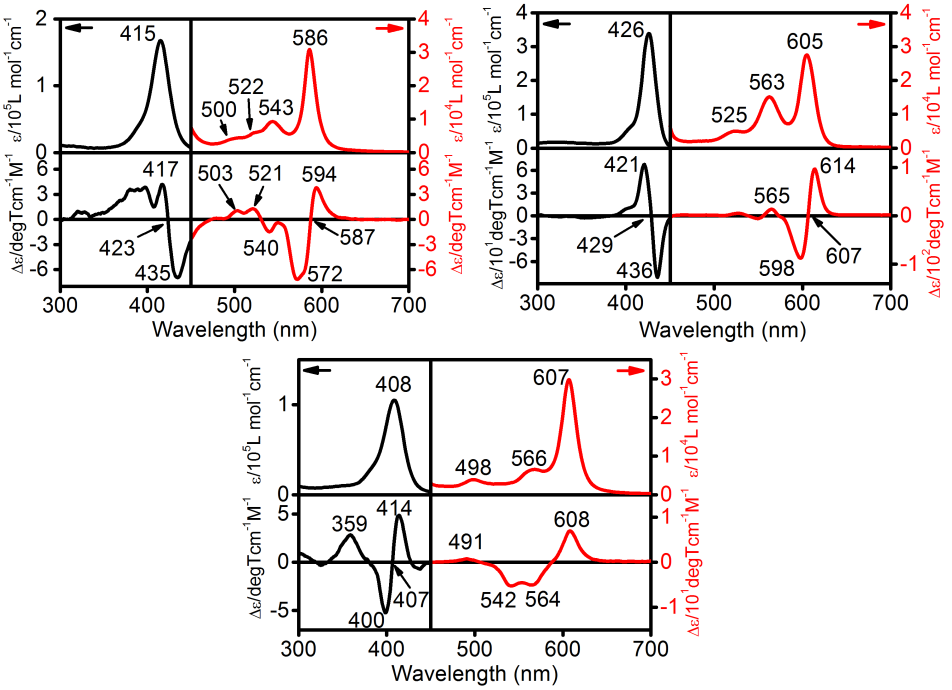

Figure 3: UV-visible and MCD spectra of compounds **8Ni** (top left), **8Zn** (top right), and **11Ni** (bottom).

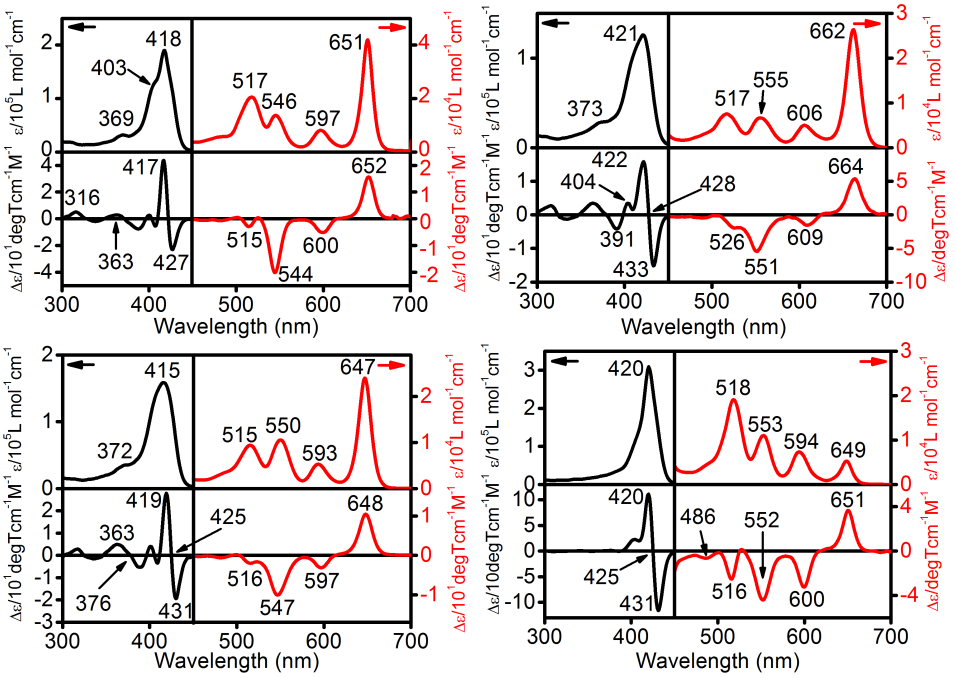

Figure 4: UV-visible and MCD spectra of compounds **$2H_2$** (top left), **$12H_2$** (top right), **$11H_2$** (bottom left), and **$9H_2$** (bottom right).

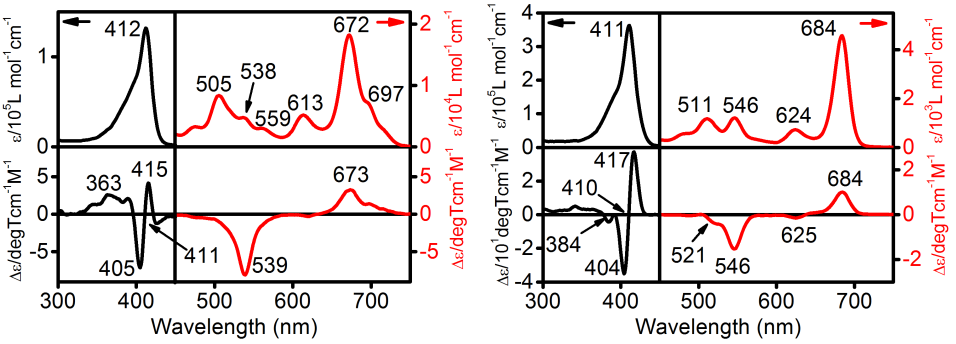

Figure 5: UV-visible and MCD spectra of compounds **$13H_2$** (left) and **$8H_2$** (right).

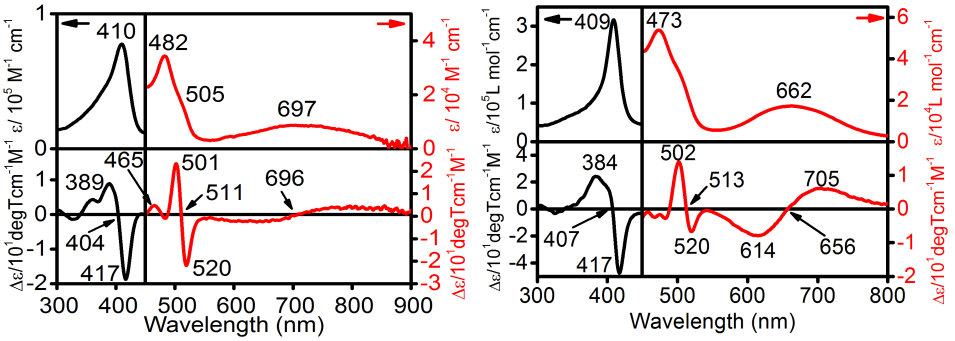

Figure 6: UV-visible and MCD spectra of compounds **5Ni** (left) and **6Ni** (right).

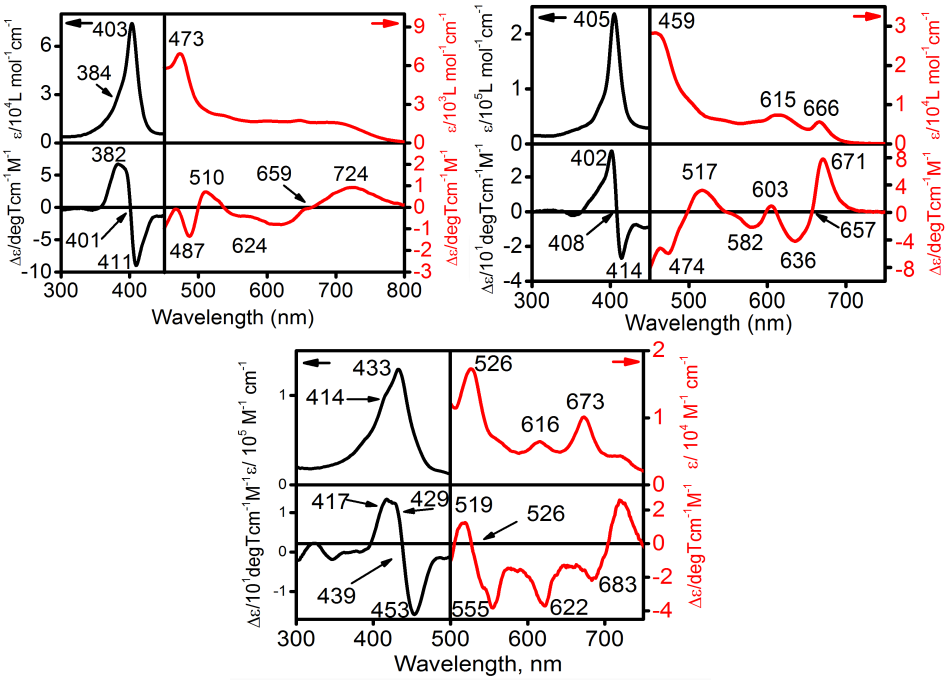

Figure 7: UV-visible and MCD spectra of compounds **5H$_2$** (top left), **6H$_2$** (top right), and **7H$_2$** (bottom).

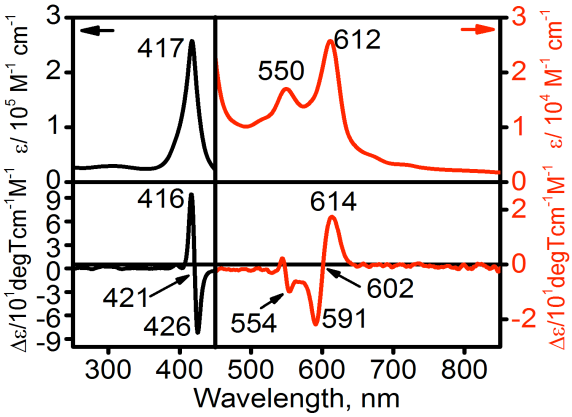

Figure 8: UV-visible and MCD spectroscopy of compound **4Zn**.

The UV-vis and MCD spectra of all compounds are shown in Figures 2 - 8. The well-known UV-vis spectrum of the reference **1H$_2$** is dominated by an intense Soret band at 417 nm, which is associated with a very strong MCD pseudo A-term centered at 419 nm. In addition, there are four bands observed at the Q-band region of this compound, which

are associated with two negative and two positive MCD B-bands in ascending energy. This type of MCD spectra is very characteristic for the free base tetraarylporphyrins.[45] Substitution of one b-carbon atom to the more electronegative nitrogen and addition of an electron withdrawing chlorine atom at the neighboring position results in an increase in the intensity of the $Q_{00}(x)$ band observed at 654 nm in porphyrin **$10H_2$**. The sequence of the MCD signals in the fully conjugated porphyrin however does not change, as four bands in the Q-band region are associated with two negative and two positive signals in **$10H_2$** in ascending energy. The Soret band in **$10H_2$** also resembles that of parent porphyrin **$1H_2$** with respect to its position and the associated strong MCD pseudo A-term centered at 425 nm (Figure 2).

The effect of the reduction of a single pyrrole ring in the free base chlorins is illustrated by chlorins **$2H_2$**, **$12H_2$**, **$11H_2$** and **$9H_2$**. The introduction of the lactone functional group in chlorin **$9H_2$**, at first glance, does not affect its electronic structure because its UV-vis spectrum still resembles that of reference porphyrin **$1H_2$**, including a Soret band at 420 nm. Its MCD spectrum of chlorin **$9H_2$**, however, suggests that there are dramatic changes in its electronic structure compared to the reference porphyrin **$1H_2$**. In particular, the $Q_{00}(x)$ band is associated with a positive MCD signal observed at 651 nm which is followed by three negative MCD signals at 600, 552, and 516 nm. Qualitatively, chlorins **$2H_2$**, **$12H_2$**, and **$11H_2$** all possess similar UV-vis and MCD spectra. In particular, all three of these chlorins have a broader Soret bands compared to the reference **$1H_2$** spectrum. This can be rationalized by the non-degenerate transitions giving rise to the Soret band and the generally increased conformational flexibility of the hydroporphyrins. All three

of these compounds also exhibit the chlorin-typical most intense $Q_{00}(x)$ band at the longest wavelength of absorption. In chlorins **$2H_2$**, **$12H_2$**, **$11H_2$**, and **$9H_2$**, four clear transitions can be identified in the Q-band region and the energies of the lowest energy transition do not vary much (ranging from 649 to 662 nm), irrespective of the presence of different heterocycles in these chlorin models. The low energy Q-band is associated with a positive MCD signal, followed by a set of three negative MCD signals in ascending energy.

The situation changes dramatically, however, when it comes to chlorins **$5H_2$**, **$6H_2$**, and **$7H_2$**, which are all derived from free base porphyrin b-diketone **$5H_2$**.[31] The Q-band region in all of these compounds are represented by closely spaced transitions, resulting in the broadening of the Q-bands. Despite of the broadening, however, the MCD spectroscopy reveals a very clear positive signal associated with the lowest energy transition in these compounds, followed by a set of negative MCD B terms in ascending energy.

Finally, free base bacteriochlorins **$13H_2$** and **$8H_2$** possess similar UV-vis spectra that are close to those of chlorins **$2H_2$**, **$12H_2$**, and **$11H_2$**, with the most intense Q-band at the longest wavelength of absorption (at 672 nm for **$13H_2$** and 684 nm for **$8H_2$**). Both of these transitions are associated with a positive MCD signal close to their corresponding energies, which are followed, by a negative MCD signal at higher energy. Unlike all other chlorins and porphyrins discussed above, however, the Soret bands in chlorins **$9H_2$** and **$13H_2$** are represented by the MCD pseudo A-terms with a positive to negative signal sequence in the Soret band region in ascending energy. Similar behavior for the both the Soret and Q-band region, having the positive to negative sequences in ascending

energies, has already been documented for tetraphenylbacteriochlorins published by Djerassi and coworkers in 1982,[43a,b] but a different behavior was observed for the free base bislactone bacteriochlorins discussed by Zhang and coworkers possessing all sp^2-hybridized b-carbons in the ring.[43c]

The MCD spectra of zinc chlorin **8Zn** and its nickel analogue **8Ni** are quite similar. In particular, the Q-band region in both compounds is dominated by two bands with the lowest energy band being the most intense in this region. The lowest energy band in both compounds is associated with a MCD pseudo A-term, centered at the corresponding band of their UV-vis spectra. The MCD pseudo A-term is almost symmetrical in compound **8Zn** but shows an asymmetrical nature in nickel complex **8Ni**, with a positive to negative amplitude in ascending energy. The situation is quite different in the case of nickel complex **11Ni**. Although the UV-vis Q-band region resembles that of complex **8Ni**, its MCD spectrum is quite different as the energy of the $Q_{00}(x)$ band at 607 nm correlates well with the MCD B-term observed at 608 nm and no MCD pseudo A-terms were observed in the Q-band region.

The UV-vis and MCD spectra of nickel complexes **5Ni** and **6Ni** reveal two unusual features. First, the Q-band regions in these compounds are represented by a very broad absorption, which is also associated with a very broad MCD pseudo A-term with positive to negative sequences in ascending energy. The second unusual feature in the UV-vis and MCD spectra of **5Ni** and **6Ni** is the relatively intense absorption asymmetric band at 482 nm for **Ni** and 473 nm for **Ni**. This unusual band is associated with a quite strong MCD pseudo A-term with negative to positive sequence in ascending energy.

Finally, in the case of the zinc isobacteriochlorin **4Zn**, the UV-vis and MCD spectra are close to the spectra observed for chlorin **TPPZn**, except the sequence of the MCD B-terms are reversed. This behavior is similar to the previously discussed zinc isobacteriochlorin.[43a,b]

Overall, in the set of hydroporphyrins and pyrrole-modified porphyrins and chlorins studied in this work, only the reference porphyrin **$1H_2$** and imidazoloporphyrin **$10H_2$** show standard porphyrin MCD spectra in the Q-band region: Two negative signals followed by two positive signals in ascending energy. All hydroporphyrins and hydroporphyrin analogues studied here possess a reversed MCD sequence in which the lowest energy transition in the UV-vis spectrum is associated with a positive signal in the MCD spectrum.

Electronic Structure:

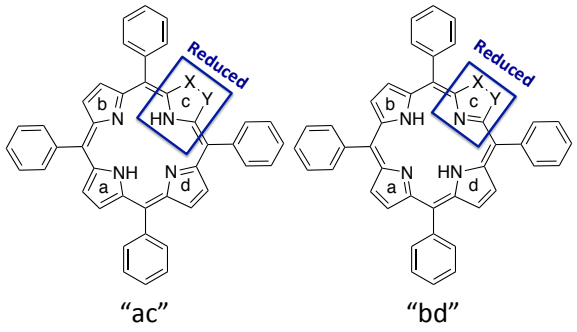

Figure 9: Two possible NH tautomers for the general chlorin structure

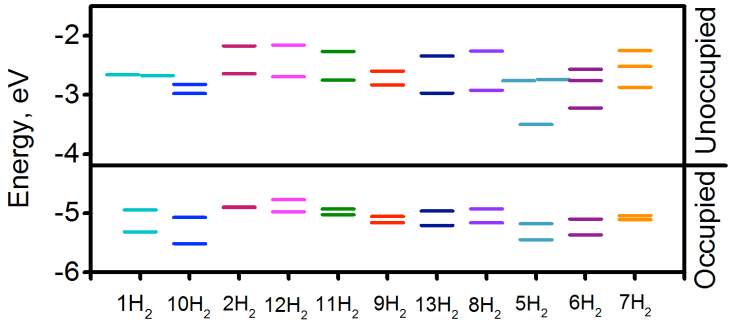

Figure 10: Frontier orbitals energy diagram for the nonmetal complexes

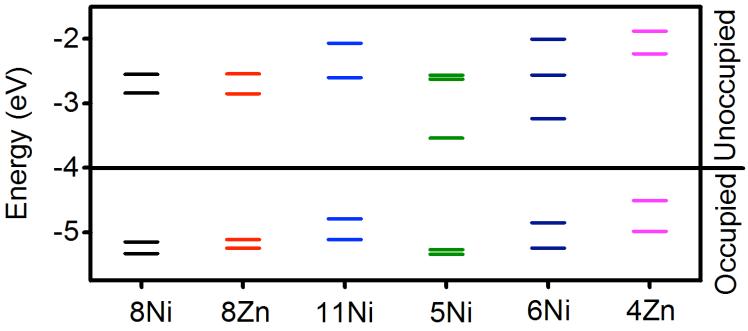

Figure 11: Frontier orbital energy diagram for the metal complexes

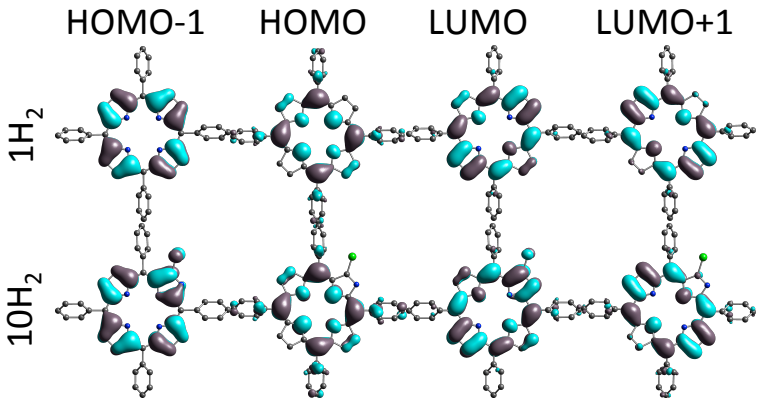

Figure 12: Frontier orbitals for compounds **$1H_2$** and **$10H_2$**

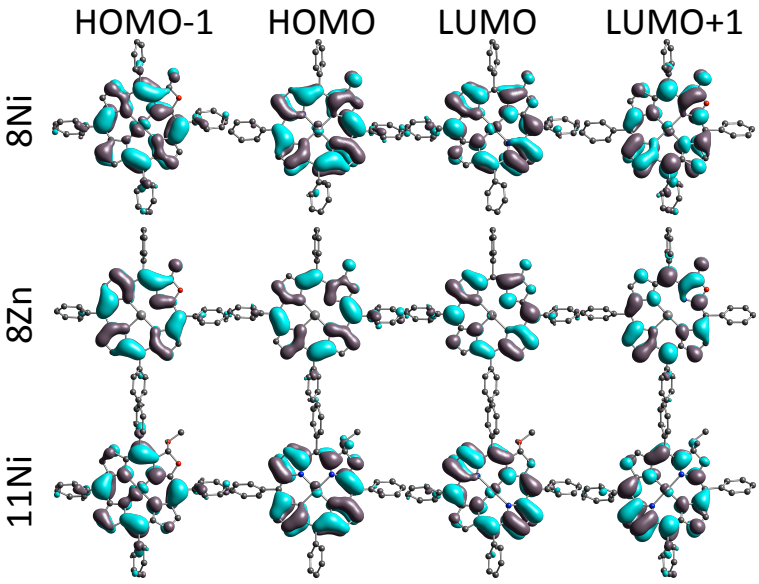

Figure 13: Frontier orbitals for **8Ni**, **8Zn**, **11Ni**

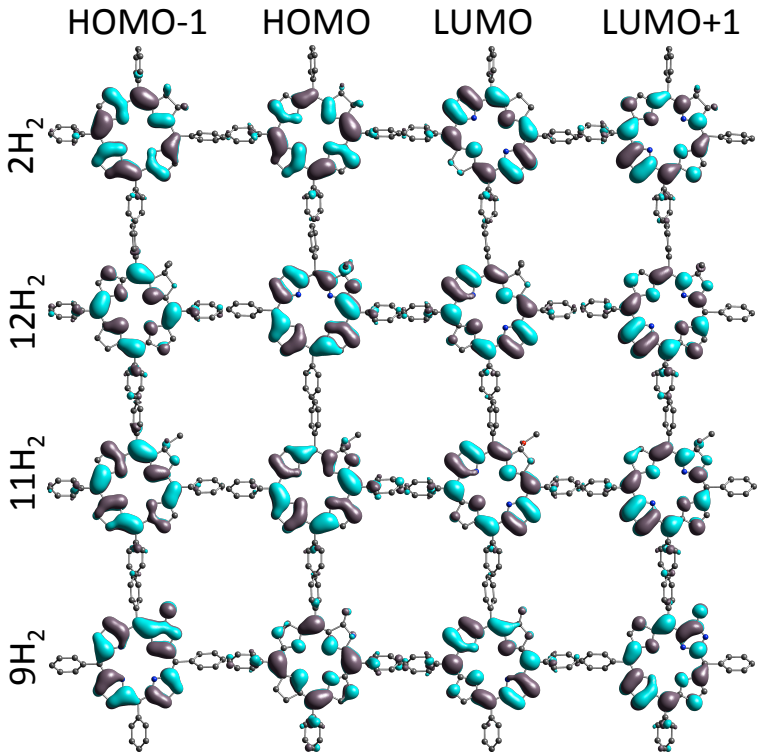

Figure 14: Frontier orbitals for compounds **$2H_2$**, **$12H_2$**, **$11H_2$**, and **$9H_2$**

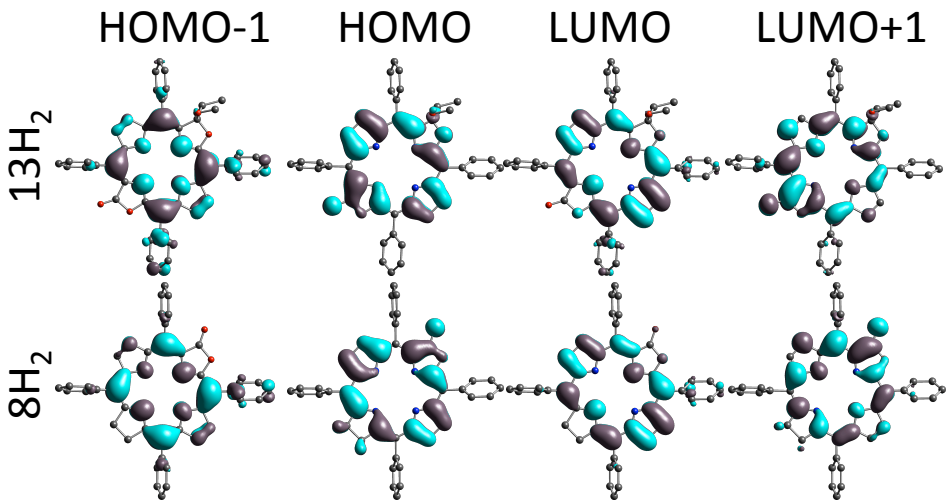

Figure 15: Frontier orbitals for compounds **$13H_2$** and **$8H_2$**

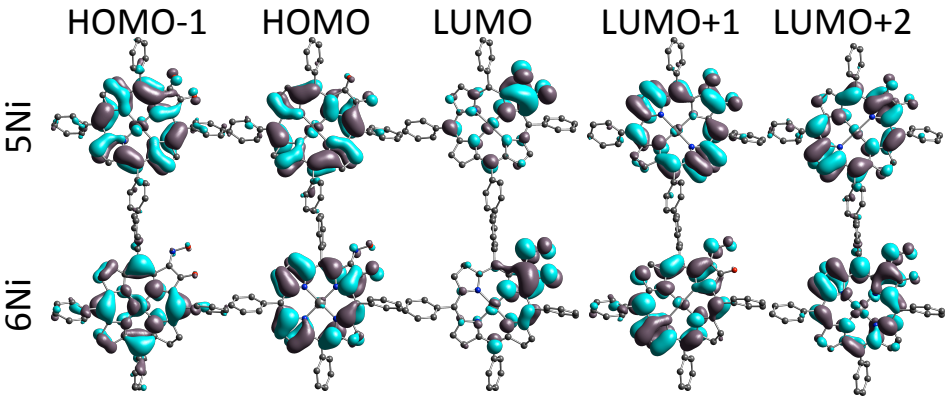

Figure 16: Frontier orbitals for compounds **5Ni** and **6Ni**

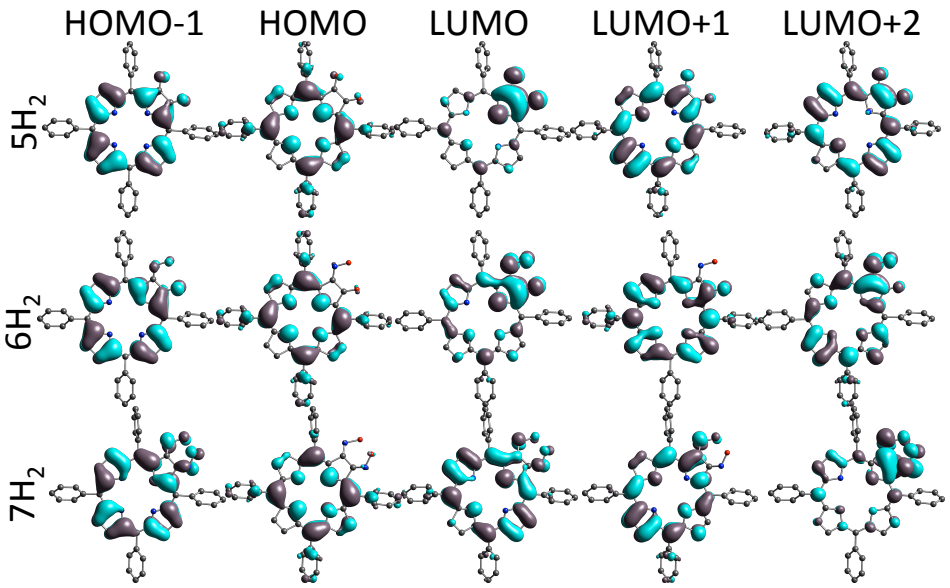

Figure 17: Frontier orbitals for compounds **5H$_2$**, **6H$_2$**, and **7H$_2$**

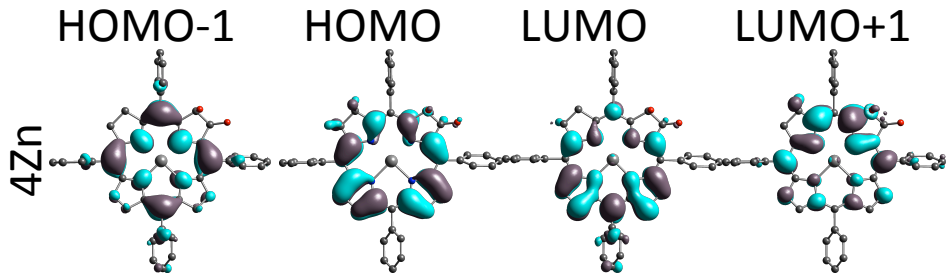

Figure 18: Frontier orbital for compound **4Zn**

To reveal the differences and similarities in the electronic spectra of the chromophores discussed, we conducted DFT and TDDFT calculations on these systems. In case of the metal derivatives, the geometry optimization is fairly straightforward. However, in the case of the hydroporphyrin free base compounds, the possibilities of different tautomers exists,[46-48] and needed to be addressed (Figure 9).[49] In all the calculations, we found that

the "ac" NH tautomers are at least ~28 kcal/mol less stable compared to the corresponding NH tautomers. Thus only the "bd" tautomers were considered.

The electronic structure of reference **1H$_2$** and core-modified porphyrin **10H$_2$** are quite close to each other and their frontier orbitals fit well within Gouterman's four-orbital model.[10] For instance, the HOMO-1 and HOMO frontier orbitals in these compounds resemble the Gouterman's a_{1u} and a_{2u} type orbitals, while the closely spaced LUMO and LUMO+1 orbitals resemble e_g set of the orbitals (in a D_{4h} space group notation). It is interesting to note that all of the metal-containing chlorin and isobacteriochlorin derivatives studied in this paper have the same orbital order for the HOMO and HOMO-1 orbitals in which the a_{1u} type orbital will always be the HOMO and the HOMO-1 will always be a_{2u} type. This sequence correlates really well with the electron withdrawing effect on the central metal in any given macrocycle, which stabilizes the a_{2u} type orbitals because of the high electron density at the inner nitrogen atoms, with the degree of stabilization of the a_{2u} orbital depending on the electronegativity of the metal cations. Accordingly, DFT predicts that the a_{2u} type orbital in zinc chlorin **8Zn** will be of lower energy than the corresponding orbital in nickel chlorin **8Ni**.

The HOMO and HOMO-1 orbital sequence in the free base chlorins and isobacteriochlorins, in general, follow the general electron withdrawing strength of the substituents at the modified pyrrole ring(s). Due to the large electron density at the inner b-pyrrolic carbon atoms and the outer substituents in a_{1u} type orbitals, electron-withdrawing groups would stabilize its energy compared to the a_{2u} type orbitals. Inversely, electron donor groups destabilize it.[10] For instance, in the case of the free base

chlorins **9H$_2$**, **5H$_2$**, **6H$_2$**, and **7H$_2$**, the HOMO orbital was found to be a_{2u} and the HOMO-1 was identified as a_{1u}. While in the case of the chlorins **12H$_2$** and **11H$_2$**, in which electron-donating groups are attached to the b-pyrrolic carbons, the HOMO orbital was found to possess a_{1u} symmetry and the HOMO-1 orbital was found to be of a_{2u} symmetry. In case of the simple metal free chlorin **2H$_2$**, the a_{2u} and a_{1u} HOMO and HOMO-1 orbitals are almost degenerate. In the case of the free base and metalated derivatives with the same chlorin macrocycles (**5H$_2$**/**5Ni** and **6H$_2$**/**6Ni**) the presence of the transition metal stabilizes the orbital of the a_{2u} type symmetry and thus reverses the nature of the HOMO and HOMO-1 orbitals.

The energies of the HOMO and HOMO-1 orbitals in all free base chlorin derivatives follow the electron-donating or electron-withdrawing strengths of the peripheral substituents. For instance, stepwise substitution of the keto groups in chlorin **5H$_2$** by the less electron withdrawing oxime fragments in **6H$_2$** and **7H$_2$** results in an incremental destabilization of the a_{2u} type orbital by ~0.2 eV and a_{1u} type HOMO-1 orbital (which is more sensitive to the substituents effect) by about ~0.4 eV. It is interesting to note that the energy difference of a_{1u} and a_{2u} types of orbitals in chlorins **5H$_2$**, **6H$_2$**, and **7H$_2$** reduces from 0.27 eV to 0.02 eV upon stepwise substitution of the carbonyl groups by oximes. The DFT-predicted structures of chlorins **11H$_2$** and **12H$_2$** allow us to conclude that the substituents in chlorin **12H$_2$** have stronger electron-donating properties than in chlorin **11H$_2$**. In the case of the free base bacteriochlorins **13H$_2$** and **8H$_2$**, DFT predicted the a_{1u} type orbitals to be the HOMO orbital and the a_{2u} orbitals to correspond to HOMO-1.

The LUMO and LUMO+1 orbitals for the majority of compounds studied in this paper resemble a pair of Gouterman's e_g orbitals oriented along two opposite pyrrolic fragments ("ac" and "bd").[10] In the case of the core-modified porphyrin **10H$_2$**, the lower energy LUMO is oriented along the modified pyrrolic ring. On the contrary, in case of the hydroporphyrins, the lower energy orbital from Gouterman's e_g set is oriented along the unsubstituted pyrrolic fragments, which includes the inner N-H bonds. In the case of the derivatives of porphyrin diketones **5Ni**, **6Ni**, **5H$_2$**, **6H$_2$**, and **7H$_2$**, the LUMO region includes a localized or hybrid orbital which is dominated by contribution from the modified pyrrolic fragment. For instance, the LUMO in chlorins **5Ni** and **5H$_2$** are predominantly located at the modified pyrrole fragment, while in the case of chlorins **6Ni** and **6H$_2$**, the largest contribution of LUMO still comes from the pyrrole rings. In the case of nickel complexes **8Ni**, **5Ni**, and **6Ni**, the MO with significant contribution of the nickel $d_{x^2-y^2}$ orbital was also observed in the LUMO energy envelope. According to the Michl perimeter model, in application to porphyrins and their analogues[44], The difference in energy between two occupied Gouterman's type a_{1u} and a_{2u} orbitals and the difference in energy between the Gouterman's e_g orbitals will dictate the sign of the lowest energy MCD signal. In the case where Δ HOMO is larger than Δ LUMO, the negative MCD signal is expected. While in the case when Δ HOMO is smaller than Δ LUMO, the positive signal of the reduced porphyrinoid will be expected. The calculated Δ HOMO and Δ LUMO values are located in Table 1. In agreement with DFT predictions, pyrrole-modified porphyrin **10H$_2$** and reference porphyrin **1H$_2$** should have a negative lowest-energy signal on the MCD spectrum, while the modified chlorin models should have the

opposite (positive) signal on the lowest-energy MCD band. This prediction correlates well with our experimental data. The only exceptions from these predictions are reduced porphyrins **5H$_2$** and **6H$_2$** in which DFT predicted that Δ LUMO is smaller than Δ HOMO. In these systems, however, the Δ LUMO is calculated as the energy difference between LUMO+1 and LUMO+2 as the LUMO in both of these compounds is predominately centered at the modified pyrrole fragment. The presence of such LUMO, however, makes Δ LUMO calculations less predictable in the assignment of the MCD signal sequence. In the case of isobacteriochlorin **4Zn** the DFT calculations fail to model the correct sign of the lowest-energy MCD signal. But as was discussed earlier by Djerrasu,[43a,b] prediction of isobacteriochlorin MCD signals are challenging.

TDDFT calculations

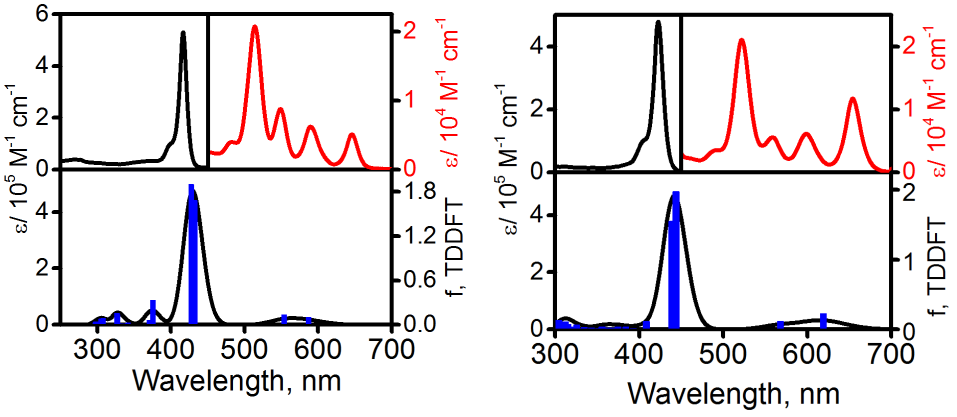

Figure 19: Experimental (top) and TDDFT predicted UV-vis spectra for compounds **1H$_2$** (left) and **10H$_2$** (right)

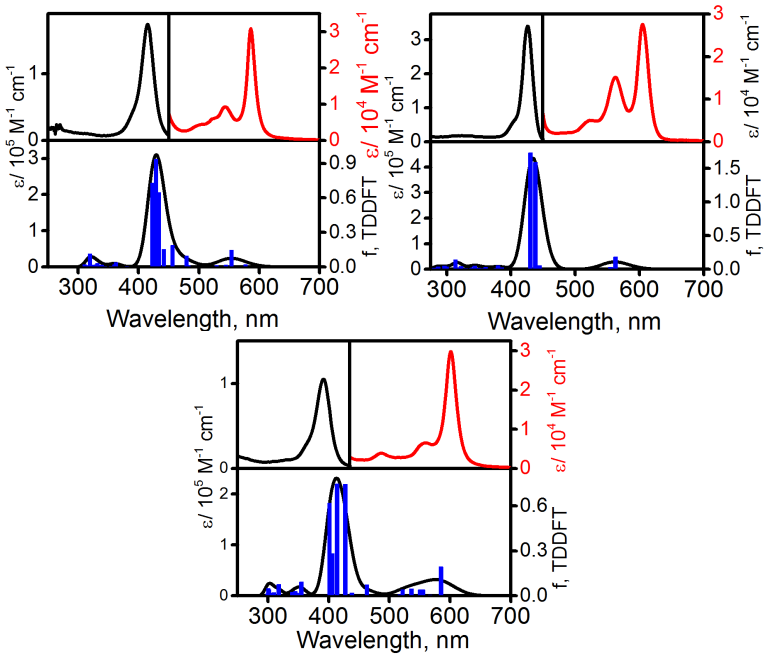

Figure 20: Experimental (top) and TDDFT predicted UV-vis spectra for compounds **8Ni** (top left) , **8Zn** (top right), **11Ni** (bottom)

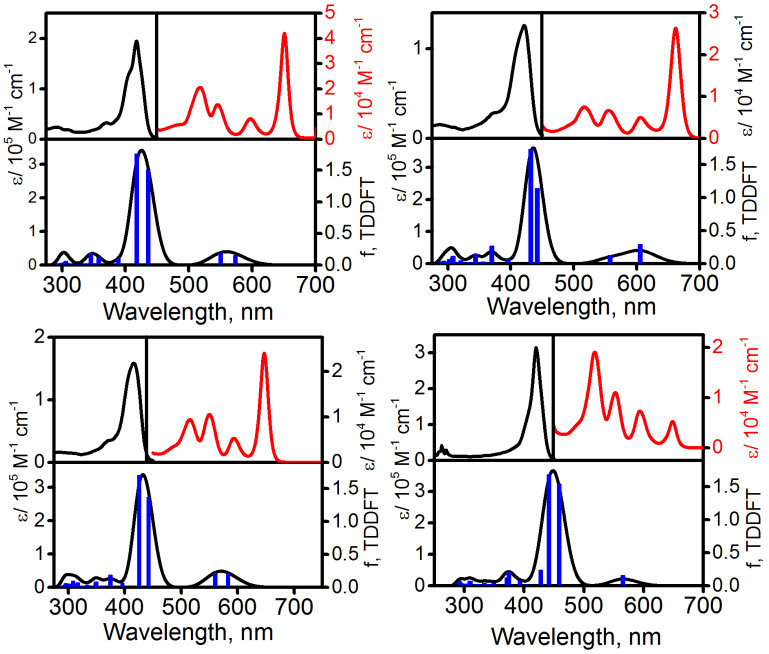

Figure 21: Experimental (top) and TDDFT (bottom) predicted UV-vis spectra for compounds **2H$_2$** (top left), **12H$_2$** (top right), **11H$_2$** (bottom left), and **9H$_2$** (bottom right)

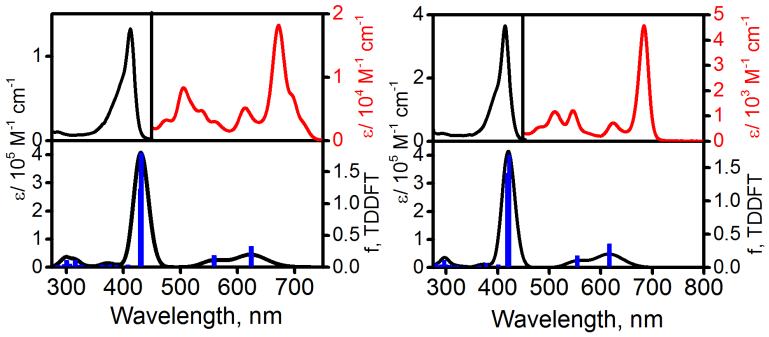

Figure 22: Experimental (top) and TDDFT (bottom) predicted UV-vis spectra for compounds **13H$_2$** (left), and **8H$_2$** (right)

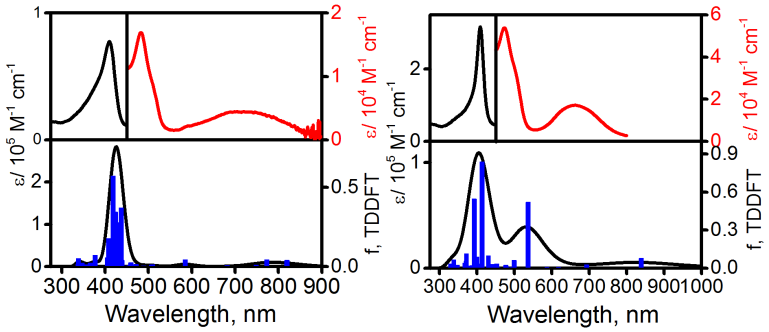

Figure 23: Experimental (top) and TDDFT (bottom) predicted UV-vis spectra for compounds **5Ni** (left) and **6Ni** (right)

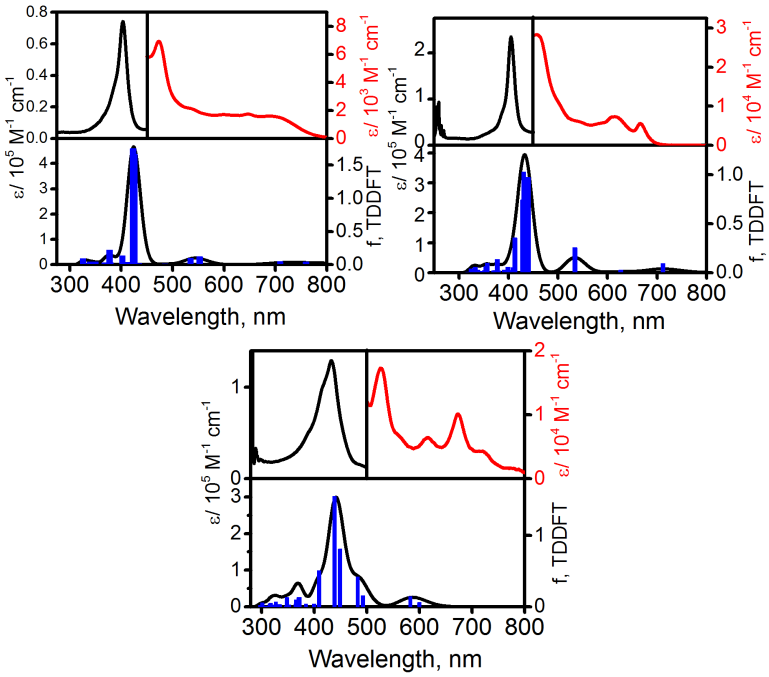

Figure 24: Experimental (top) and TDDFT (bottom) predicted UV-vis spectra for compounds **5H$_2$** (top left), **6H$_2$** (top right), and **7H$_2$** (bottom)

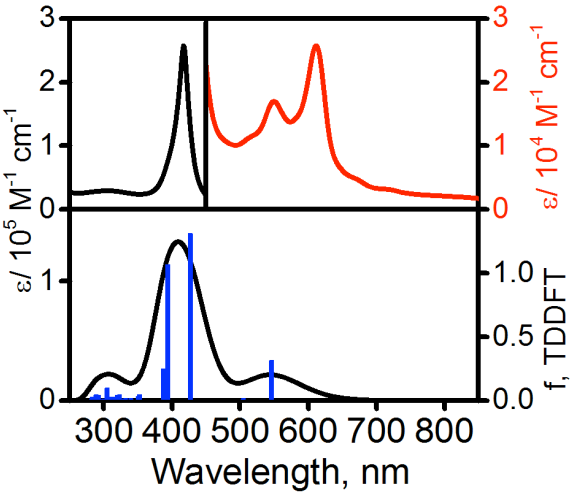

Figure 25: Experimental (top) and TDDFT (bottom) predicted UV-vis spectra for compound **4Zn**

TDDFT was used to compute the UV-vis spectra of the porphyrinoids investigated (Figures 19-25). As expected, in reference porphyrin **$1H_2$** and pyrrole-modified porphyrin **$10H_2$** the most intense transitions originate from the classic Gouterman's π-π single electron excitations and their Q-band region from HOMO → LUMO and HOMO → LUMO+1 single-electron transitions, complemented by HOMO-1 → LUMO and HOMO-1 → LUMO+1 excitations. The Soret band region is dominated by two very strong excited states, which predominately originate from HOMO-1 → LUMO and HOMO-1 → LUMO+1 single-electron transitions complemented by the HOMO → LUMO and HOMO → LUMO+1 transitions.

In case of chlorins **$2H_2$**, **$12H_2$**, and **$11H_2$**, and **$9H_2$**, the basic Gouterman's model[10] is still valid as the TDDFT transitions in the Q-band region have lower intensity than the Soret band excited states and all transitions are found to be dominated by the HOMO/HOMO-1 → LUMO/LUMO+1 single-electron excitations. As discussed above, the LUMO in the carbonyl-containing chlorin systems **$5H_2$** and **$6H_2$** is predominately centered at the modified pyrrole ring. As a consequence of this localization, one might expect that the lowest energy HOMO → LUMO transitions would not be related to the Gouterman model. Indeed, TDDFT predicts that the first three excited states in chlorin **$5H_2$** will predominately originate from the HOMO/HOMO-1/HOMO-2 → LUMO single-electron excitations. These intramolecular charge transfer transitions were predicted to have low intensities and be located within the 840 – 710 nm envelope. There are thus likely responsible for the significantly broad and diffuse nature of the UV-vis and MCD

spectra in the Q-band region for these compounds. In addition to these intramolecular charge transfer (CT) transitions, TDDFT predicts two classical Gouterman excited states in the Q-band region originating from the HOMO/HOMO-1 → LUMO+1/LUMO+2 single-electron transitions (at 553 and 535 nm). TDDFT further predicts we have two low-energy excited states (7 and 8) in the 485 nm region which correspond to the weak band at 473 nm of the UV-vis spectrum of **5H$_2$**, and that is associated with a relatively strong MCD signal. The nature of these transitions is rather unique. They are a combination of the intramolecular CT transitions originating from the localized a-diketone fragment (HOMO-2) to the LUMO+1 and LUMO+2 porphyrin centered orbitals, complemented by the HOMO-4 porphyrin π orbital to the LUMO (localized at modified pyrrole fragment), as well as classic Gouterman's HOMO-1 to LUMO+1 and LUMO+2 π-π* transitions. In both of these excited states, the largest contribution to the intensity originates from the Gouterman's π-π* single electron excitations, which agrees well with the presence of two MCD B-terms observed between 480 – 520 nm. Finally, the Soret band region in the UV-vis spectrum of **5H$_2$** is dominated by the excited states 14 and 15 which represent the classic Gouterman's π-π* transitions originating from the HOMO-1/HOMO → LUMO+1/LUMO+2 single-electron excitations. Similar to compound **5H$_2$**, the broadening in the Q-band region in compounds **6H$_2$** and **7H$_2$** can be explained by the presence of additional intramolecular transitions which involve a localized, at the modified pyrrole ring, low-energy molecular orbital.

In the case of bacteriochlorins **8H$_2$** and **13H$_2$**, TDDFT predicts that the most intense bands in the visible region will originate from the classic Gouterman's HOMO-1/HOMO

→ LUMO/LUMO+1 single-electron transitions. The large energy gap between the LUMO and LUMO+1 orbitals in these systems, however, results in a striking difference for the predicted nature of the transitions found in the Soret and Q-band regions. Indeed, in the case of the reference porphyrin **1H$_2$**, as well as systems **10H$_2$**, **2H$_2$**, **12H$_2$**, **11H$_2$**, and **9H$_2$**, the Q-band region is dominated by the single-electron excitations from the HOMO orbital to the LUMO and LUMO+1, and the single-electron excitations in the Soret band region are dominated by transitions from the HOMO-1 → LUMO / LUMO+1 molecular orbitals. On the contrary, the Q-band region in the bacteriochlorins **8H$_2$** and **13H$_2$** can be described by the excited states 1 and 2 which are dominated by the HOMO→LUMO transitions (excited state 1) but the HOMO-1→LUMO single-electron transitions (excited state 2). Similarly, the Soret band in bacteriochlorins **8H$_2$** and **13H$_2$** is dominated by excited states 3 and 4, which mainly originate from the HOMO → LUMO+1 (excited state 3) and the HOMO-1 → LUMO+1 (excited state 4) single-electron excitations. The unusual nature of these excited states explains the large energy difference between the Q(x) and Q(y) band in the UV-vis and MCD spectra in compounds **8H$_2$** and **13H$_2$**, as well as the presence of the reverse MCD pseudo A-term in the Soret band region. This reverse MCD pseudo A-term sequence was only observed for free base bacteriochlorins **8H$_2$** and **13H$_2$**.

The UV-vis spectrum of zinc chlorin **8Zn** can also be described within the parameters of Gouterman's four-orbital model.[10] Indeed, the two largest intensity transitions in the Q-band region are excited states 1 and 2 which originate from HOMO/HOMO-1 → LUMO/LUMO+1 single-electron excitations. Similarly, the Soret band in zinc chlorin

8Zn is dominated by two excited states (4 and 5), which originate from the same single-electron transitions as the Q-band region. The presence of nickel in chlorin system **8Ni** allows for low-energy CT transitions from nickel-centered orbitals (HOMO-2 - HOMO-4) to the chlorin-centered LUMO and LUMO+1 molecular orbitals. Indeed, TDDFT predicts that the first two excited states in chlorin **8Ni** will be dominated by the nickel to chlorin metal to ligand charge transfer transitions, although their intensities are relatively small. The Q-band region in chlorin **8Zn** is dominated by excited state 3, which has the major contribution from HOMO → LUMO. The Soret band region in nickel complex **$9H_2$** is dominated by the three excited states 13-15, fit well the Gouterman's model,[10] with contributions from the HOMO/HOMO-1 → LUMO/LUMO+1 single-electron transitions. In general, for nickel chlorin **11Ni** excited states were predicted that are similar to those of chlorin **8Ni,** except that the lowest energy excited state 1 is a Gouterman type π-π transition, followed closely by MLCT transitions in the Q-band region.

In the case of nickel complexes **5Ni** and **6Ni**, the occupied MO localized on the dione fragment is the HOMO-5 orbital, while the unoccupied orbital localized on the dione fragment is the LUMO orbital. Thus, in addition to the Gouterman's predicted π-π* transitions in the Q-band region (excited states 7 and 8), the presence of low-energy excited states dominated by HOMO → LUMO and HOMO → LUMO+1 transitions are expected. These transitions have π-π* character and can be described as intramolecular CT in nature. Indeed, TDDFT predicts that the first two excited states will have predominant HOMO→LUMO and HOMO-1→LUMO character. In addition, the MLCT

bands originating from the single-electron excitations from the HOMO-2 - HOMO-4 →LUMO were also predicted by TDDFT calculations in the low energy region (excited states 3, 4, and 5). It is therefore not surprising that the Q-band region in **5Ni** and **6Ni** are much broadened. Interestingly, the classic Gouterman's π-π* transitions in nickel complexes **5Ni** and **6Ni** originating from the HOMO/HOMO-1 → LUMO+1/LUMO+2[10] were predicted to lie in the 500 - 510 nm range. This correlates well with the corresponding MCD pseudo A-terms centered at 511 and 513 nm, respectively. Finally, TDDFT predicts at least nine intense excited states at the Q-band region, which have complex contributions from the π-π and MLCT single-electron excitations.

Although the LUMO and LUMO+1 orbitals in zinc isobacteriachlorin **4Zn** are located at adjacent pyrrolic rings, they are still π* orbitals. Thus, it is not surprising that the first two excited states belong to the classic Gouterman's HOMO-1/HOMO → LUMO/LUMO+1 single-electron excitations. Since only these two transitions are present in the Q-band region, it is not surprising that the corresponding MCD and UV-vis spectral signals are narrow. Similarly, the excited states 3 and 4 originate from the Gouterman's π-π* transitions and resemble Soret band intensities in normal porphyrins.

Conclusion

A set of free-base and transition metal 5,10,15,20-tetraphenyl substituted chlorins, bacteriochlorins, isobacteriochlorins, and their pyrrole-modified analogues were investigated by a combination of UV-vis and MCD spectroscopy and DFT and TDDFT computations. It was found that the nature of the substituents at the β-pyrrolic positions

of the chlorin macrocycle dictates the intensities of the low-energy bands in the Q-band region. In the case of the chlorin derivatives that originate from the b-diketone chlorins, it was found that the Q-band region is dominated by very broad absorption features, determined to result from a superposition of π-π* and MLCT single-electron transitions. The bacteriochlorins have both positive to negative sequences in ascending energy in both the Q-and Soret-band regions, while the zinc isobacteriochlorin **4Zn** has a MLCT sequence similar to the chlorin derivatives. In all cases, the MCD spectroscopy is suggestive of the Δ HOMO being smaller than Δ LUMO relationship for the frontier macrocycle-centered molecular orbitals.

This investigation helped to shed light on the elctronic features of pyrrole-modified porphyrins, particularly with repect to their classification as chlorin- or porphyrin-type chromophores. The results therefor help in guiding the rational depvelopment of chromophores with electronic properties that are customized to their applications.

Experimental Section

Materials

All chromophores described were synthesized from **1H$_2$**[50] as described in the literature, and referenced in the text.

Computational studies

All computations were performed using the *Gaussian 09* software package running under Windows or UNIX OS.[51] Molecular orbital contributions were compiled from

single point calculations using the QMForge program.[52] In all single-point calculations, the TPSSh exchange-correlation functional[53] was used. The 6-31G(d) basis set[54] was used for all atoms in all calculations. Frequencies were calculated for all optimized geometries in order to ensure that final geometries represent minima on the potential energy surface. TDDFT calculations were conducted for the first 50 excited states in order to ensure that all π-π^* transitions of interest were accounted for. Solvent effects were modeled using PCM approach using DCM as a solvent.[55]

Spectroscopy

All UV-Vis data were obtained on a JASCO-720 spectrophotometer at room temperature. An OLIS DCM 17 CD spectropolarimeter with a 1.4 T DeSa magnet was used to obtain all Magnetic Circular Dichroism (MCD) data.

Chapter Three: Tuning up an electronic structure of the subphthalocyanine derivatives toward electron-transfer process in non-

covalent complexes with C_{60} and C_{70} fullerenes: experimental and theoretical studies

SUMMARY:

Non-covalent p-p interactions between chloroboron subphthalocyanine (**1**), 2,3-subnaphthalocyanine (**3**), 1,4,8,11,15,18-(hexathiophenyl)subphthalocyanine (**4**), or 4-*tert*-butylphenoxyboron subphthalocyanine (**2**) with C_{60} and C_{70} fullerenes were studied by UV-vis and steady-state fluorescence spectroscopy, as well as, mass (APCI, ESI, and CSI) spectrometry. Mass spectrometry experiments were suggestive of relatively weak interaction energies between compounds **1** - **4** and fullerenes. The formation of a new weak charge-transfer band in the NIR region was observed in solution only for subphthalocyanine **4** when titrated with C_{60} and C_{70} fullerenes. Molecular structures of the subphthalocyanines **2** and **4** as well as co-crystallite of **4** with C_{60} fullerene (**4@C_{60}**) were studied using X-ray crystallography. One of the C_{60} fullerenes in the crystal structure of **4@C_{60}** was found in the concave region between two subphthalocyanine cores, while the other three fullerenes are aligned above individual isoindole fragmets of the aromatic subphthalocyanine. The excited state dynamics in non-covalent assemblies were studied by transient absorption spectroscopy. The time-resolved photophysics data suggest that only electron-rich subphthalocyanine **4** can facilitate an electron-transfer to C_{60} or C_{70} fullerenes, while no electron-transfer from the photoexcited receptors **1** - **3** to fullerenes was observed in UV-vis and transient spectroscopy experiments. DFT calculations using the CAM-B3LYP exchange-correlation functional and the 6-31+G(d)

basis set allowed an estimation of interaction energies for the non-covalent 1:1 and 1 : 2 (fullerene : subphthalocyanine) complexes. Theoretical data suggest that the weak (~3.5 - 10.5 kcal/mol) van der Waals-type interaction energies tend to increase with an increase of the electron density at the subphthalocyanine core with compound **4** being the best platform for non-covalent interactions with fullerenes. DFT calculations are also indicate that 1 : 2 (fullerene : subphthalocyanine) non-covalent complexes are more stable than corresponding 1 : 1 assemblies.

INTRODUCTION:

Covalent and non-covalent donor-acceptor (D-A) assemblies were intensively studied during the last several decades due to their potential use in solar energy to electricity conversion.[1-5] The electronic structure, type of the linking group (if any), and geometric orientation of the light-harvesting donor and electron acceptor are the key for formation and stability of the long-living charge-separation (CS) state, which is required for efficient in solar energy to electricity conversion.[2] In the case of the D-A assemblies with covalent bonds coupling a donor and an acceptor fragments, a D-A distance and degree of the electronic coupling between them can be controlled by the nature of the linking group.[5-8] Preparation of covalently linked D-A assemblies, however, often requires several additional synthetic steps, which make such structures less attractive for industrial applications. An alternative approach is formation of well-organized non-covalent assemblies, which can be controlled by, for instance, specific dispersion p-p interactions. Because of their specific photophysical properties useful for light harvesting, aromatic macrocycles, such as porphyrins and their analogues were extensively studied as

electron donors in D-A structures, while fullerenes and carbon nanotubes were proposed as electron acceptors in non-covalently linked assemblies.[9-11] For non-covalent D-A assemblies, which are based on dispersion p-p interactions, both topology and electron density of the p-systems of the donor and acceptor plays an important role. For instance, electron-rich and planar b-octaalkylporphyins can easily form non-covalent assemblies with fullerenes, while planar but less electron-rich neutral unsubstituted or alkyl-substituted phthalocyanines or tetraazaporphyrins do not form such supramolecular systems.[7] The addition of eight electron-donating substituents to the planar tetraazaporhyrin core, however, can increase the p-electron density at the tetraazaporphyrin core and enhance non-covalent p-p coordination with fullerenes.[12]

The bowl-shaped geometry of subphthalocyanine, probably, provides the best topology for non-covalent p- p complex formation with the curved surfaces of C_{60} and C_{70} fullerenes.[9,13] Not surprisingly, subphthalocyanine-fullerene heterolayers, along with subphthalocyanine-subphthalocyanine and subphthalocyanine-subnaphthalocyanine systems, have been proposed as prospective non-covalent donor-acceptor components for organic heterojunction photovoltaic platforms.[14] The energetics and spectroscopy of such non-covalent p-p interaction between subphthalocyanine derivatives and fullerenes remains, however, largely unexplored. Covalently linked subphthalocyanine-fullerene assemblies, on the other hand, were explored in great detail by Torres and co-workers, who clearly demonstrated the importance of the subphthalocyanine-to-fullerene distance for effective electron-transfer or energy-transfer processes.[5b] In addition, Torres and co-workers studied non-covalent interactions between fullerenes and pre-formed

bis(subphthalocyanine)-containing spherical cages, which was proven to accommodate a single fullerene molecule.[5h,i] Ziessel and co-workers briefly discussed non-covalent coordination between C_{60} fullerene and unsubstituted subphthalocyanine with an axial ethynylphenyl group and found 1:1 complex formation with a binding constant of 3,975 M^{-1}.[15] Although no data were provided to support such a claim, the authors observed subphthalocyanine fluorescence quenching in toluene, which they assigned to the electron transfer from subphthalocyanine to fullerene. In 2011, Kobayashi and co-workers published an impressive X-ray crystal structure of fullerene : pyrene-fused subphthalocyanine assembly, which exploited high affinity of the pyrene fragment to form a 1:2 (fullerene : subphthalocyanine) complex with fullerene in the solid state, although these authors did not see any significant interaction between two components in solution.[9c] In 2013, Torres and co-workers observed non-covalent p-p interactions between unsubstituted and b,b'-hexaalkylsulfonyl substituted subphthalocyanines and concluded that both 1:1 and 1:2 (fullerene : subphthalocyanine) complexes can be formed in solution. Energy transfer, rather than electron-transfer was assigned as the major deactivation pathway upon photoexcitation of the subphthalocyanine core.[16] However, unlike in their previous work on subphthalocyanine cages,[5h,i] the authors did not present ESI MS or UV-vis titration data, and their analysis shown in the supporting information is inconclusive. Very recently, on the basis of DFT calculations, Denis predicted the 19.9 - 33.8 kcal/mol and the 38.8 - 68.5 kcal/mol interaction energies for 1:1 and 1:2 (fullerene : subphthalocyanine) non-covalent complexes.[17] These calculations, however, raise the question why, despite such a strong interaction energies and fairly negative Gibbs

energies predicted by DFT for non-covalent complex formation between fullerenes and subphthalocyanines, their spectroscopic signatures in solution remain unobserved. Indeed, Torres and co-workers in 2014[18] and Konarev and co-workers in 2015[19] presented solid state X-ray crystal structures of non-covalent bis(subphthalocyanine) : C_{60} and axially linked bis(subphthalocyanine) : C_{60} complexes, respectively. In addition, Konarev and co-workers observed a new low intensity broad band between 650 and 750 nm in UV-vis spectrum of their system in the solid state.[19] Nevertheless, interactions between subphthalocyanine receptors and C_{60} fullerene in solution remains unexplored to a large extent.

In this paper, we explore the tunability of the subphthalocyanine core toward finding a stronger binding fullerene receptor both in a solid state and in a solution, which could potentially improve photovoltaic characteristics of subphthalocyanine : fullerene heterojunctions by facilitating the electron-transfer from subphthalocyanine to fullerene. In order to do so, we compared four basic aromatic platforms (Figure 1): (i) chloroboron subphthalocyanine as a reference compound; (ii) chloroboron 2,3-subnaphthalocyanine as a system with an expanded aromatic p-system; (iii) chloroboron 1,4,8,11,15,18-(hexathiophenyl)substituted subphthalocyanine as a system with an increased electron density because similar to phthalocyanine analogues,[20] the electronic structure of subphthalocyanine[21] indicates that substitution at the a,a'-positions of the subphthalocyanine core with electron-donating groups should increase cores' electron density to a higher extent compared to the b,b'-substitution pattern used by Torres and co-workers; (iv) 4-*tert*-butylphenoxyboron subphthalocyanine in order to investigate if axial,

electron-rich, phenoxy substituent would facilitate interaction with fullerenes. We used both C_{60} and C_{70} fullerenes due to their slightly different topology of their p-system and thus potentially different energies of interactions with subphthalocyanine analogues.

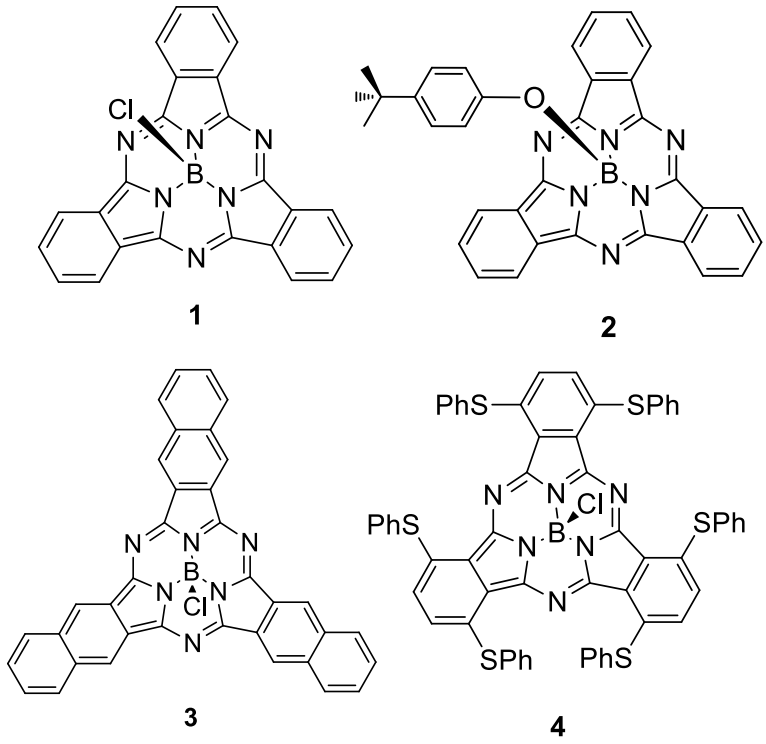

Figure 1. Structure of subphthalocyanine and its derivatives used in this paper.

EXPERIMENTAL SECTION:

Reagents and materials: When necessary, reactions were performed under an argon atmosphere using standard Schlenk techniques. Solvents were purified using standard approaches: toluene was dried over sodium metal, THF was dried over sodium-potassium alloy, hexane and DCM were dried over calcium hydride. Chloroboron subphthalocyanine, SubPcBCl (**1**), 4-*tert*-butylphenol, thiophenol, 2,3-dicyano-1,4-

dihydroxybenzene, 2,3-dicyanonaphthalene, C_{60}, and C_{70} were purchased from Aldrich and used without further purification. SubPcB(OC_6H_4-*tert*-Bu) (**2**),[22] 2,3-SubNcBCl (**3**),[23] $SubPc^{(SPh)6}BCl$ (**4**),[24] and 3,6-diphenylthio-2,3-dicyanobenzene[24] were prepared as described earlier and have similar to the reported UV-vis, ^1H NMR, and ESI or APCI mass spectra.

***DFT and TDDFT Calculations*:** All DFT calculations were conducted using the Gaussian 09 software.[25] The complexes were optimized in a gas phase at the DFT level using the CAM-B3LYP exchange-correlation functional.[26] In a separate set of test calculations on the smallest **1** : C_{60} system, wB97XD,[27] TPSSh,[28] M06,[29] M06L,[30] and CAM-B3LYP[26] exchange-correlation functionals were used to investigate exchange-correlation functional dependence on the calculated interaction energies for non-covalent complexes of interest. The 6-31+G(d) basis set[31] was used for all atoms in these calculations. The 6-31+G(d) basis set was found to be a good compromise for a quality (double-zeta level) and has both polarization and diffuse functions, which are critical for accurate description of the weak,long distance, non-covalent interactions in donor-acceptor assemblies. The integral value was set to "ultrafine" and the "acc2e=12" command was used in these calculations to set the 2-electron integral accuracy parameters to 10^{-12}. Equilibrium geometries were confirmed by frequency calculations and specifically by the absence of imaginary frequencies. QMForge program was used for molecular orbital analysis.[32]

***X-ray crystallography*:** Single crystals of **4** and **4@C_{60}** useful for the X-ray crystallographic experiments were prepared by the slow evaporation of saturated DCM/hexane (**4**) or toluene/hexane (**4@C_{60}**) solutions. The X-ray quality crystals of subphthalocyanine **2** were obtained by slow evaporation of its toluene solution. Single crystals of **C_{60}@*o*-DCB** were grown from the mixture of subphthalocyanine **1** and C_{60} in *o*-DCB during our attempt to crystallize **1@C_{60}** assembly. A Rigaku RAPID-II diffractometer with a graphite monochromator and Mo Ka (λ=0.71073 Å) or Cu Ka (λ= 1.54178 Å) radiation. All experiments were conducted at -150 ^{o}C temperature. Multi-scan absorption correction[33] was applied to the data in all cases. The crystal structures were solved by the direct method (*SIR-92*)[34] or *Superflip* approach[35] and refined by a full-matrix least-squares method based on F^2 using the *Crystals for Windows*,[36] *SHELXL-2013*, and *SHELXLE* programs.[37] In the case of the X-ray structure of **4**, a disordered solvent molecule was observed on the Fourier density map, which was eliminated using standard SQUEEZE protocol implemented into *PLATON* software.[38] All non-hydrogen atoms were refined anisotropicaly, while hydrogen atoms were refined using "riding mode" with displacement parameters bonded to a parent atom: $U_{iso}(H) = 1.2U_{eq}(C)$ (U_{eq} = $1/3(U_{11}+U_{22}+U_{33})$).

A crystal structure of the non-covalent **4@C_{60}** was successfully solved using *SHELXT*: the solution showed a subphthalocyanine molecule **4** and one of C_{60} fullerene units. Another C_{60} was located on a mirror plane. It was possible to refine these three moieties in isotropic approximation. Still, around half of the space remained unoccupied, including a cavity between two subphthalocyanine units. Several areas with high electron

density were visible; however, obvious disorder prevented us from locating atoms of C_{60}. Fullerene fragments were placed in three areas located at three-fold rotational axes intersecting the mirror plane using FRAG command in *SHELXL-2013*. Occupancies of each of them were multiplied by 1/6. Attempts to refine occupancies confirmed that the model with one C_{60} entity in each position is the best fit to the experimental data. Poor resolution prevented us from attempting to resolve disorder after fitting the fullerene group. In addition, a phenyl ring of solvent toluene molecule was visible on residual Fourier density map. Crystal data for systems **2**, **4**, and **4@C$_{60}$** are summarized in Table 1, while selected bond distances and angles are presented in Table 2. CCDC 1411398, 1411397, 1411396, and 1411407 contain the supplementary crystallographic data for **2**, **4**, **4@C$_{60}$**, and **C$_{60}$@*o*-DCB**, respectively. These data can be obtained free of charge via www.ccdc.cam.ac.uk/conts/retrieving.html (or from Cambridge Crystallographic Data Centre, 12 Union Road, Cambridge CB2 1EZ, UK; fax: (+44) 1223-336-033 or deposit@ccdc.cam.ac.uk).

Table 1. Summary of crystallographic data for compounds **2** , **4**, and **4@C$_{60}$**.

	2	**4**	**4@C$_{60}$**
Empirical formula	$C_{34}H_{25}B_1N_6O_1$	$C_{60}H_{36}B_1Cl_1N_6S_6$	$C_{120}H_{12}B_1Cl_1N_6S_6$
Formula weight	544.42	1079.65	1775.98
Crystal system	Triclinic	Trigonal	Hexagonal
Space group, Z	P-1, 2	R-3, 6	P 63/m, 12

a (Å)	8.5172(9)	21.6424(7)	25.560(7)
b (Å)	12.7393(14)	21.6424(7)	25.560(7)
c (Å)	13.2237(15)	19.4859(13)	39.513(5)
α (°)	79.896(6)	90	90
β (°)	78.303(6)	90	90
γ (°)	70.711(5)	120	120
Volume ($Å^3$)	1317.0(3)	7904.3(6)	22357(12)
$\rho_{calc}(g/cm^3)$	1.373	1.361	1.583
$\mu(K_\alpha)(mm^{-1})$	0.086	3.230	0.289
$\theta_{max}(°)$	23.247	68.127	18.923
GoF(F^2)	1.0084	0.9016	2.132
R_1 ($F^2>2\sigma(F^2)$)	0.0881	0.0695	0.2001
wR_2[b] (all data)	0.2405	0.1690	0.2655

***Spectroscopy Measurements*:** A Jasco-720 spectrophotometer was used to collect UV-vis data. An OLIS DCM 17 CD spectropolarimeter with a 1.4 T DeSa magnet was used to collect all MCD data. Complete spectra were recorded at room temperature in parallel and anti-parallel directions with respect to the magnetic field. Steady-state fluorescence data were collected using a Cary Eclipse fluorimeter at room temperature. Bruker micrOTOF II and micrOTOF III systems were used in atmospheric pressure chemical ionization (APCI), electro-spray ionization (ESI), and cryo-spray ionization (CSI) experiments. Bruker Daltonics facility in Yokohama, Japan, equipped with a Bruker micrOTOF II CryoSpray Ion Source was used to collect all CSI and some ESI

data. Samples were studied in THF or toluene solutions and washed with a continuous flow of THF or *i*-PrOH during experiment.

Fluorescence lifetimes were measured using time correlated single photon counting. Samples in a 1 cm quartz cuvette were excited with a 472 nm, 40 MHz diode laser (Driver: Picoquant PDL 800-B; Head: Picoquant LDH-P-470). Emission was directed through a double monochromator (Jobin-Yvon DH-10) and detected using an avalanche photodiode (Picoquant MPD PDM). The instrument response of the system is approximately 500 ps FWHM.

Pump-probe spectroscopy allowed for the time resolved measurement of non-emissive samples. A home-built laser system consisting of a Ti:sapphire oscillator (powered by a Spectra Physics Millenia Pro) and regenerative amplifier (powered by a Spectra Physics Empower 15) generated ~60 fs (FWHM), 0.8 mJ, 805 nm pulses at a repetition rate of 1 kHz. A portion of this light was directed into a home-built noncollinear optical parametric amplifier (NOPA) to create excitation pulses at 560 nm. Continuum probe pulses (420-750 nm) were created by focusing a small fraction of the 805 nm light (~20 mW) into a 2 mm sapphire window. The excitation light was polarized at 54.7 degrees relative to the probe polarization (the magic angle) to isolate the isotropic dynamics of the excited state. Time delay between the excitation and probe pulses was controlled by a mechanical delay stage (Newport UTM150PP.1). After the pulses were focused in the sample, the probe beam was collimated, directed through a monochromator (Princeton Instruments SP2150i, gratings were 150 lines/mm and were blazed at 500 nm for the visible probe experiments and 1.2 μm for the near-IR probe

experiments). The dispersed signals were detected using either a 256 pixel silicon diode array for the visible portion of the spectrum (Hamamatsu S3902-256Q) or a 256 linear pixel InGaAs diode array for the near-IR portion of the spectrum (Hamamatsu G9213-256S). The pump beam was modulated at half the laser repetition rate while the probe beam was measured for every laser pulse allowing for the change in optical density, ΔOD, induced by the pump to be calculated for each pulse pair. The dependence of the ΔOD signal for pulse energies between 10-40 nJ was found to be linear. Data shown was collected with pulse energies of 25-35 nJ. Samples had an optical density of 0.25 at the excitation wavelength and were continuously pumped through a 1 mm flow cell during data collection to ensure a fresh sample for each laser pulse.[39] Absorption spectra taken before and after the pump probe experiments were indistinguishable, indicating no evidence of sample degradation.

RESULTS AND DISCUSSION

X-Ray Crystal Structures. Two key structures of the subphthalocyanine receptors **2** and **4** were confirmed by X-ray crystallography in addition to the earlier reported structure of subphthalocyanine **1**. Experimental refinement data for subphthalocyanines **2** and **4** are listed in Table 1. In addition, key bonds lengths and bond angles are reported in Table 2. CAMERON plots of receptors **2** and **4** are shown in Figure 2. As the other known subphthalocyanines, subphthalocyanine macrocycle in **2** and **4** has a non-planar bowl-shaped conformation with the boron atom located above the 3N plane formed by the nitrogen atoms in isoindole fragments.[9,40] Trigonal pyramidal

(3N+X) coordination in both compounds **2** and **4** is complimented by the axial oxygen (**2**) or chlorine (**4**) atom. Lengths of the axial B-O and B-Cl bonds in **2** and **4**, respectively, agree well with previously reported subphthalocyanines.[9,40] Equatorial B-N bond distances are also in the normal range for this type of compounds.[9,15,18,40] The axial substituted phenol ligand in subphthalocyanine **2** is significantly tilted from the axial plane toward the subphthalocyanine p-system. The equatorial thiophenol fragments in subphthalocyanine **4** are closer to the perpendicular arrangement from the isoindole plane. The packing diagram for subphthalocyanines **2** and **4** is shown in Supporting Information Figure S1. In the case of compound **2**, there are several close (3.35 - 3.39 Å) p-p interactions observed between neighboring subphthalocyanine molecules. In the case of the thiophenol system **4**, a zigzag motif formed by the close C---H contacts is dominated in the packing diagram.

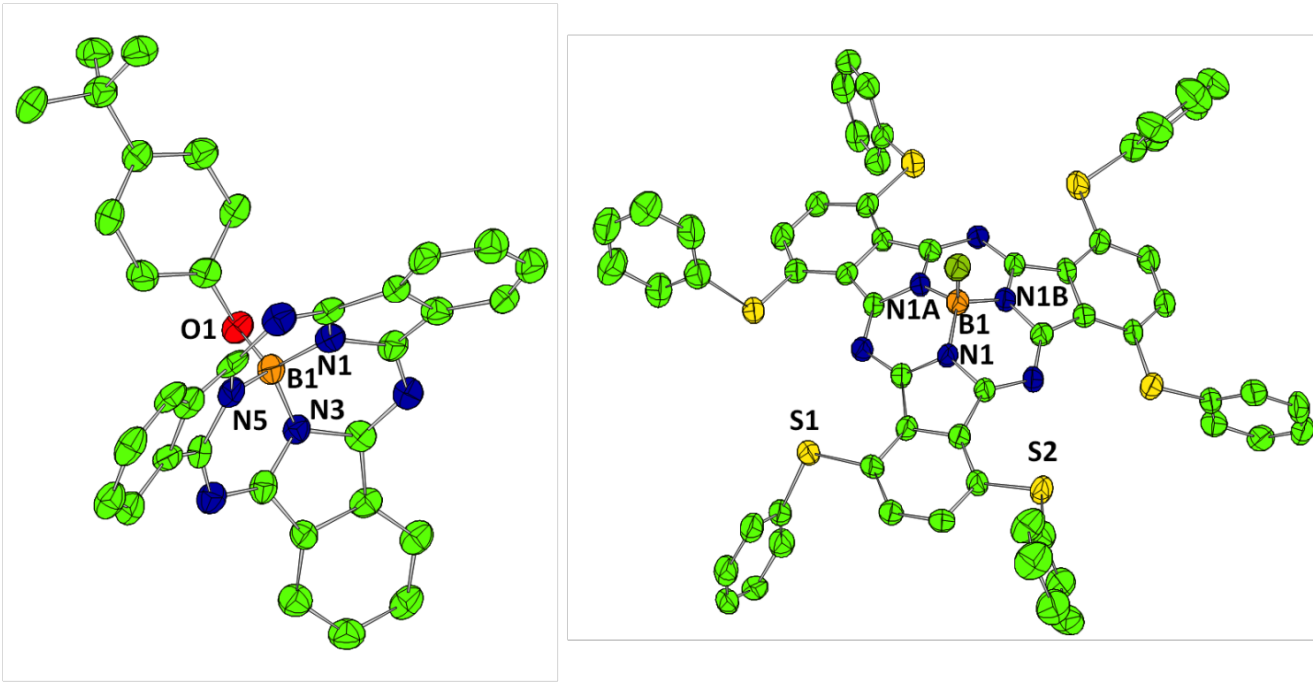

Figure 2. Labeled CAMERON diagrams for X-ray structures of **2** (left) and **4** (right).

Hydrogen atoms are omitted for clarity. The thermal ellipsoid probability level is 50%.

Table 2. Selected bond lengths (Å) and angles (°) for compounds **2** and **4.**

Compound **2**			
N(1)-B(1)	1.494(13)	N(5)-B(1)-O(1)	117.3(8)
N(3)-B(1)	1.468(12)	N(1)-B(1)-O(1)	114.2(8)
N(5)-B(1)	1.485(12)	N(3)-B(1)-O(1)	110.3(8)
O(1)-B(1)	1.474(12)	N(3)-B(1)-N(5)	105.5(7)
O(1)-C(25)	1.348(10)	N(1)-B(1)-N(3)	104.5(7)
		N(1)-B(1)-N(5)	103.9(8)
Compound **4**			
N(1)-B(1)	1.468(6)	N(1)-B(1)-Cl(1)	113.6(5)
Cl(1)-B(1)	1.834(12)	N(1)-B(1)-N(1A)	105.0(5)
S(1)-C(9)	1.779(6)	S(1)-C(3)-C(4)	124.8(4)
C(3)-S(1)	1.766(5)	S(1)-C(9)-C(10)	121.5(4)
S(2)-C(15)	1.791(7)	C(5)-C(6)-S(2)	124.5(4)
C(6)-S(2)	1.758(5)	S(2)-C(15)-C(20)	123.5(6)

As the main goal of this report was to obtain a reasonable proof of subphthalocyanine-to-fullerene interaction, we tried to crystallize such non-covalent complexes using subphthalocyanines **1** - **4** and fullerenes C_{60} and C_{70}. In all cases, toluene, *o*-dichlorobenzene (*o*-DCB), and their mixtures with hexanes, CH_2Cl_2, or chloroform were explored for crystallization, while subphthalocyanine : fullerene ratio was varied between 1 : 1 up to 1 : 10. In case of the parent subphthalocyanine **1**, the only X-ray quality crystals we obtained were well ordered **C_{60}@*o*-DCB** non-covalent

assemblies (Supporting Information Figures S2 and S3). Similarly, all our attempts to obtain suitable for X-ray analysis crystals of receptors **2** and **3** with fullerenes C_{60} and C_{70} resulted is fullerene single crystals formation. These results are in agreement with the current state of the literature as there was no X-ray structure of a "standard" monomeric subphthalocyanine or naphthalocyanine to fullerene non-covalent complexes were reported despite of a large interest for such systems. In the case of electron-rich thiophenol-containing subphthalocyanine **4**, we were able to crystallize its non-covalent complex with C_{60} fullerene (Figure 3). We are aware of only three similar systems reported in the literature. The first structure was published by Kobayashi and co-workers for pyrene-containing subphthalocyanine system in which pyrene fragment facilitates p-p interaction between subphthalocyanine macrocycle and C_{60} fullerene in a solid state.[9c] In the second reported structure, Torres and co-workers were able to crystallize a fully conjugated *anti*-bis(subphthalocyanine) with C_{60} fullerene.[18] In this case, the authors exploited the expanded bis(subphthalocyanine) p-system to promote non-covalent interactions with C_{60} fullerene. In the third case, Konarev and co-workers used axially linked conformationally rigid bis(subphthalocyanine) receptors to form a non-covalent complex with C_{60} fullerene.[19] The **4@C$_{60}$** complex reported here, to the best of our knowledge, is the first example of a monomeric subphthalocyanine, that was able to co-crystallize non-covalently with C_{60} fullerene. Moreover, this is the only reported system in which three clear subphthalocyanine : fullerene interaction motifs are simultaneously present in the solid state (Figure 3). The first structural motif represents a 2 : 1 (**4** : C_{60}) non-covalent complex formation in which a single fullerene molecule is located between

two concave surfaces of the electron-rich p-system of **4** (Figure 3B). The observed concave-to-fullerene coordination motif is similar to that observed by Kobayashi and co-workers, Torres and co-workers,[18] as well as Konarev and co-workers.[19] The close fullerene - subphthalocyanine contacts are ranging between 3.1 - 3.4 Å, while the distances between the boron atom in **4** and C_{60} were found around 3.7-3.8 Å. The fullerene : subphthalocyanine contacts in **4@C$_{60}$** assembly are slightly shorter compared to the similar distances reported by Konarev and co-workers in their subphthalocyanine : fullerene assembly (3.3 - 3.8 Å).[19] It also correlates well with our DFT calculations, which suggest closer receptor : fullerene distances for the more electron-rich subphthalocyanine **4**. In addition, the X-ray structure of **4@C$_{60}$** reveals three C_{60} molecules aligned above each of the individual isoindole fragments of subphthalocyanine **4** (Figure 3C). According to the earlier reported[41] and our DFT calculations, such "sitting atop" interaction should be less energetically favorable compared to the "concave" type of non-covalent interaction. Not surprisingly, close contacts between these "sitting atop" fullerenes and subphthalocyanine **4** (3.3 - 3.6 Å) are slightly longer compared to those observed in subphthalocyanine concave : fullerene motif. Finally, two thiophenol substituents on the same isoindole fragment can also form close contacts (3.3 - 3.7 Å) with the C_{60} fullerene (Figure 3D). Overall, out of three areas with close contacts between compound **4** and the fullerene, two were found to involve the subphthalocyanine core and one involves electron-rich thiophenyl substituents. All three fullerenes that interact with subphthalocyanine **4** can be clearly seen on the experimental electron density map at 0.83 e/Å^3 level (Supporting Information Figure S4).

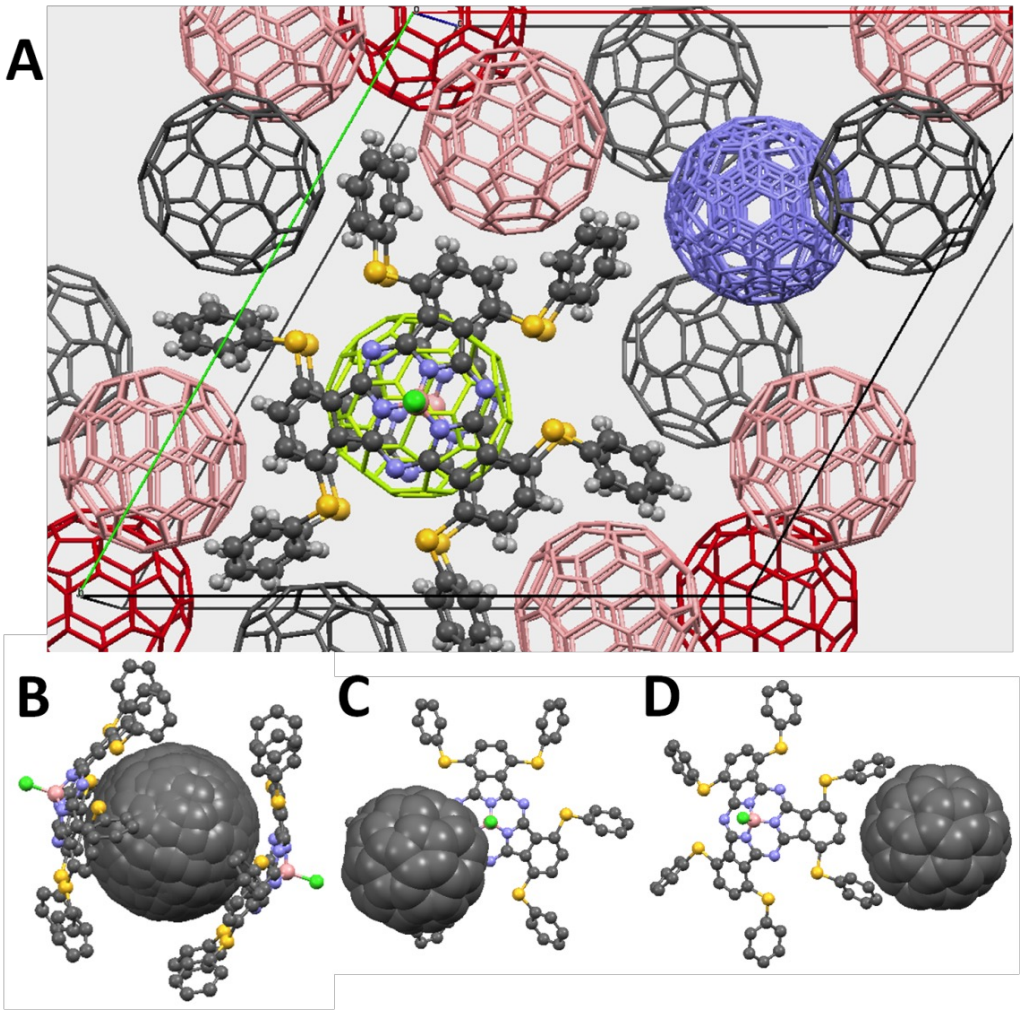

Figure 3. ORTEP and MERCURY diagrams for X-ray structure of **4@C_{60}**. Hydrogen atoms are omitted for clarity. (**A**) prospective view of the unit cell; (**B**) "concave" 1 : 2 motif; (**C**) one out of three "sitting atop" motifs; (**D**) one out of three fullerene : 2 thiophenol non-covalent interactions motif.

Spectroscopy. Although X-ray crystallography is clearly suggestive of the possible non-covalent interactions between prepared by Kobayashi's,[9c] Torres's,[18] Konarev's,[19] and our group's subphthalocyanines and C_{60} fullerenes in a solid state, it is unclear if such

interactions remain strong enough in solution to affect spectroscopic properties of the targeted non-covalent donor-acceptor assemblies. Indeed, Kobayashi and co-workers mentioned that they were not able to recognize any specific spectroscopic signatures for pyrene-containing subphthalocyanine : fullerene assemblies in solution.[9c] In addition, Torres and co-workers stated that at the first glance no evidence for similar interaction between octaalkylthio-substituted subphthalocyanines and fullerenes were observed in solution and careful analysis was needed to recognize such spectroscopic signatures.[16]

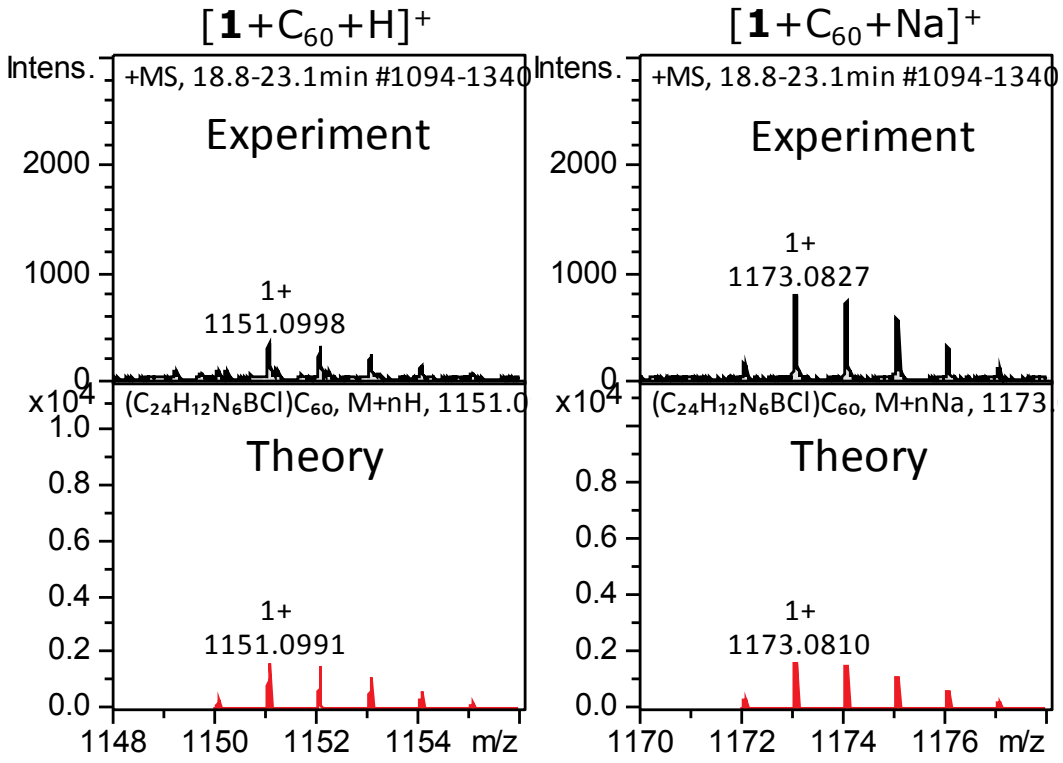

Figure 4. Partial ESI (positive mode) spectra of subphthalocyanine **1** in the presence of C_{60} fullerene.

In order to fully characterize spectroscopic signatures for non-covalent complex

formation between subphthalocyanines **1** - **4** and C_{60} and C_{70} fullerenes in solution, we conducted an extensive set of mass spectrometry, UV-vis and steady-state fluorescence spectroscopy, as well as, transient absorption spectroscopy experiments. First, we collected APCI, ESI, and CSI mass spectrometry data on subphthalocyanine-based receptors **1**, **3**, and **4**. The choice of these three mass spectroscopy methods was dictated by two key assumptions. First, all three methods are known for gentle ionization of weakly interacting non-covalent assemblies[42] with two of them (ESI and CSI) using the close electrospray approach and the remaining one (APCI) using similar ionization technique. The second assumption was that the typical temperature range used in these three methods (450^{o}C for APCI, 200^{o}C for ESI, and -40^{o}C for CSI) would provide a crude estimation of the subphthalocyanine : fullerene complex stability. In the case of positive or negative polarity APCI experiments, the only peaks observed in the mass spectra corresponded to the compounds **1**, **3**, and **4** and C_{60} or C_{70} fullerenes. Lowering electrospray capillary temperature to 250^{o}C (regular temperature for ESI experiments) allows us to detect low intensity peaks for 1 : 1 complex formation between subphthalocyanine-type receptors **1**, **3**, and **4** and C_{60} fullerenes with individual subphthalocyanine and fullerene peaks dominating mass spectra (Figure 4 and Supporting Information Figure S5). Finally, low temperature CSI experiments reveal the presence of both 1 : 1 and 2 : 1 (macrocyclic receptor : fullerene) non-covalent complexes (Figure 5 and Supporting Information Figures S6 - S8). Due to the differences in ionization cross-section between **1**, **3**, and **4**, one cannot easily draw quantitative conclusions about the effectiveness or the energetics of non-covalent complex formation between

subphthalocyanines **1**, **3**, and **4** and C_{60} and C_{70} fullerenes. ESI and CSI experiments, however, clearly show that non-covalent complexes exist in solution. Observation of such assemblies under ESI, but not APCI conditions can allow crude estimation of non-covalent complex stabilities in terms of thermal energy.[42] It is clear that the APCI probe is too hot for non-covalent complexes to survive. The observation of 2 : 1 complexes in CSI experiments but not in ESI experiments suggest that the ESI probe is too hot for 2 : 1 complexes to survive. Of course, in order to quantify the subphthalocyanine : fullerene complexes dissociation energy, one would need to conduct a set of calibrated collision-induced dissociation experiments, which would require a special mass spectrometry setup. It was estimated, however, that in order to observe signals of non-covalent complexes in ESI experiments the stability of these systems should be at least 12 - 14 kcal/mol at 250^{o}C.[42] In agreement with this assumption, a 17 - 18 kcal/mol dissociation energy for the non-covalent metal-free tetraphenylporphyrin : C_{60} complex was suggested on the basis of ESI experiments.[43] In this case, only a very weak molecular ion signal was observed in ESI experiments. Stronger ESI signal for protonated porphyrin : C_{60} complexes was observed in ESI experiments by the same authors that calculated 28 - 34 kcal/mol binding energies for these systems.[44]

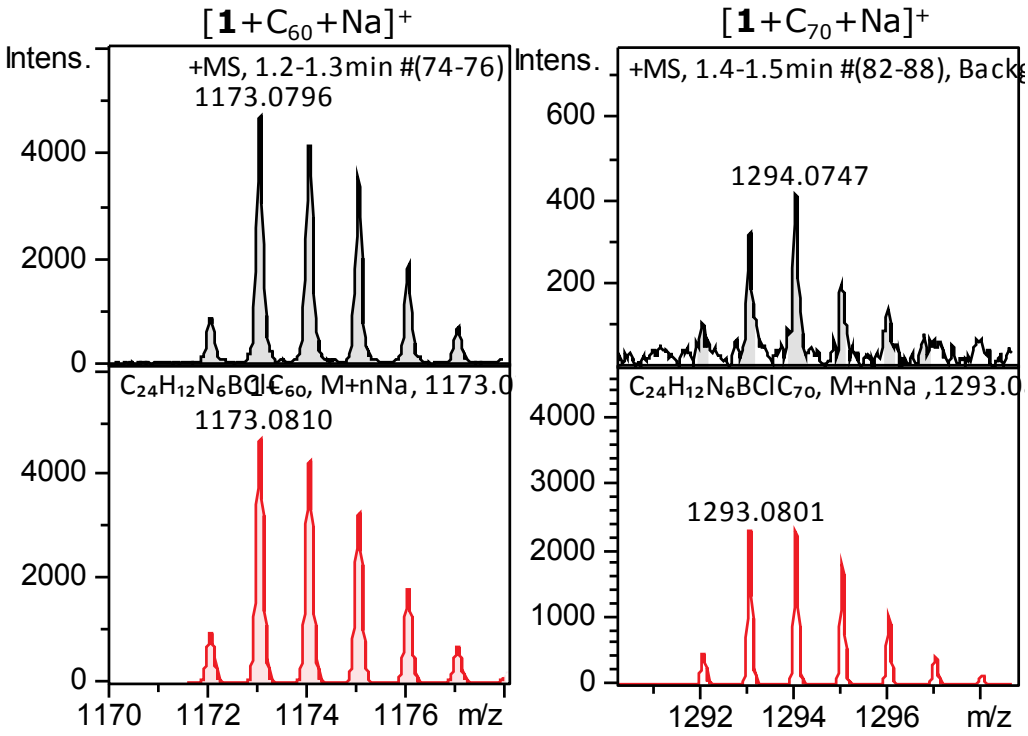

Figure 5. Partial CSI (positive mode) spectra of subphthalocyanine **1** in the presence of C_{60} and C_{70} fullerenes.

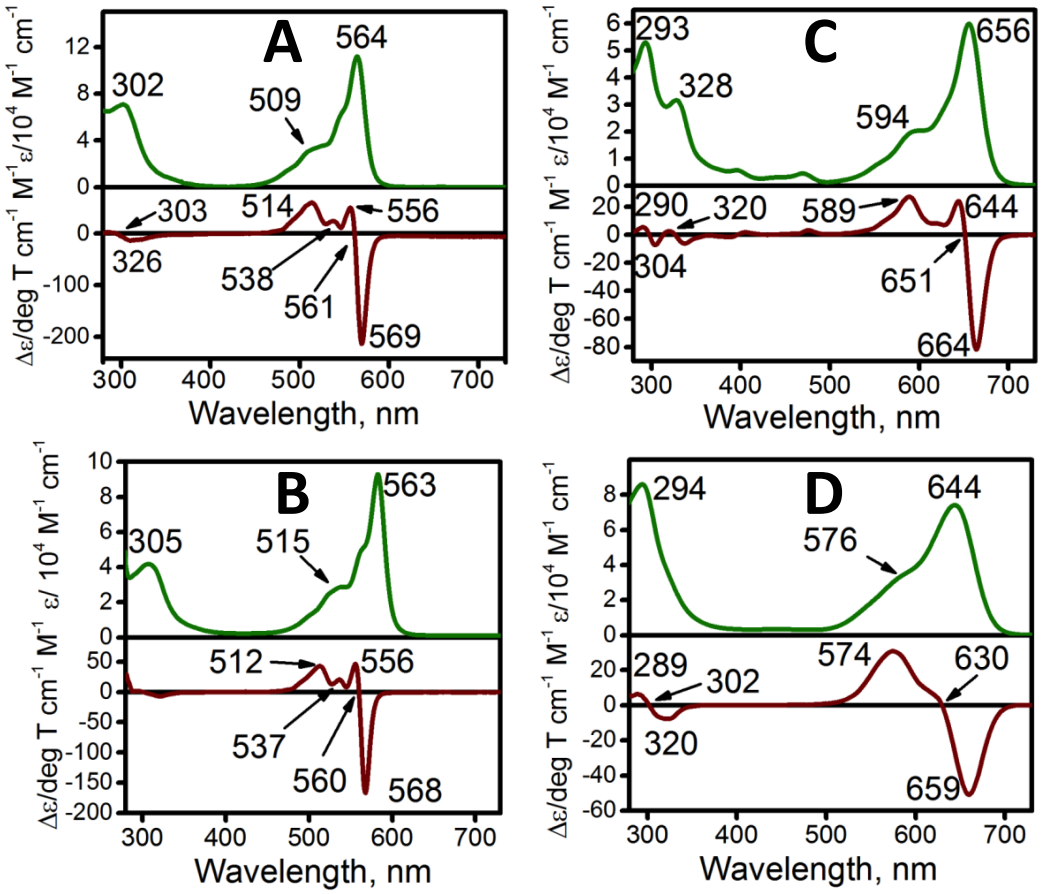

Figure 6. UV-vis (green, top) and MCD (brown, bottom) spectra of compounds **1** (**A**), **2** (**B**), **3** (**C**), and **4** (**D**).

Table 3. UV-vis spectra and time constants data for compounds **1** - **4**.

Compound	UV-vis λ, nm ($\varepsilon/10^4$)
1	564 (7.01), 546sh, 510sh, 303 (3.83)
2	563(4.97), 546sh, 515sh, 305(4.62)
3	656(4.47), 594sh,328(4.5), 293(4.72)
4	644(4.87), 576sh, 294(4.72)

UV-vis and MCD spectra of macrocycles **1** – **4** are shown in Figure 6 and their quanitative properties are presented in Table 3. In agreement with the previous reports on subphthalocyanines,[9,13,40,45] substitution of the axial chlorine atom by a *p-tert*Bu-C_6H_4-O group in **2** has a negligible effect on their UV-vis and MCD spectra because they are dominated by the intense SubPc centered $\pi\rightarrow\pi^*$ transitions. Benzoannulation of the p-system of the subphthalocyanine core results in a large shift to lower energy of the *Q*-band indicative of reduction of the HOMO-LUMO energy gap in **3** compared to parent macrocycles **1** and **2**. A similar effect is well-known for benzannulated phthalocyanine derivatives.[46] Introduction of six electron-donating thiophenol groups at a-positions of the subphthalocyanine core results in an expected,[20,21] large, low-energy shift of the *Q*-band in the UV-vis spectrum of **4** compared to the parent systems **1** and **2**. MCD spectra of receptors **1** - **4** are clearly suggestive of the degeneracy of their first excited state as indicated by the presence of a strong MCD Faraday *A*-term in the *Q*-band region. Since TDDFT calculations on subphthalocyanines clearly indicate that the *Q*-band is dominated

by the HOMO → LUMO, LUMO+1 single electron excitations, the low-energy shift in subphthalocyanine **4** reflects significant reduction in the HOMO - LUMO energy gap in this compound compared to subphthalocyanines **1** and **2**.

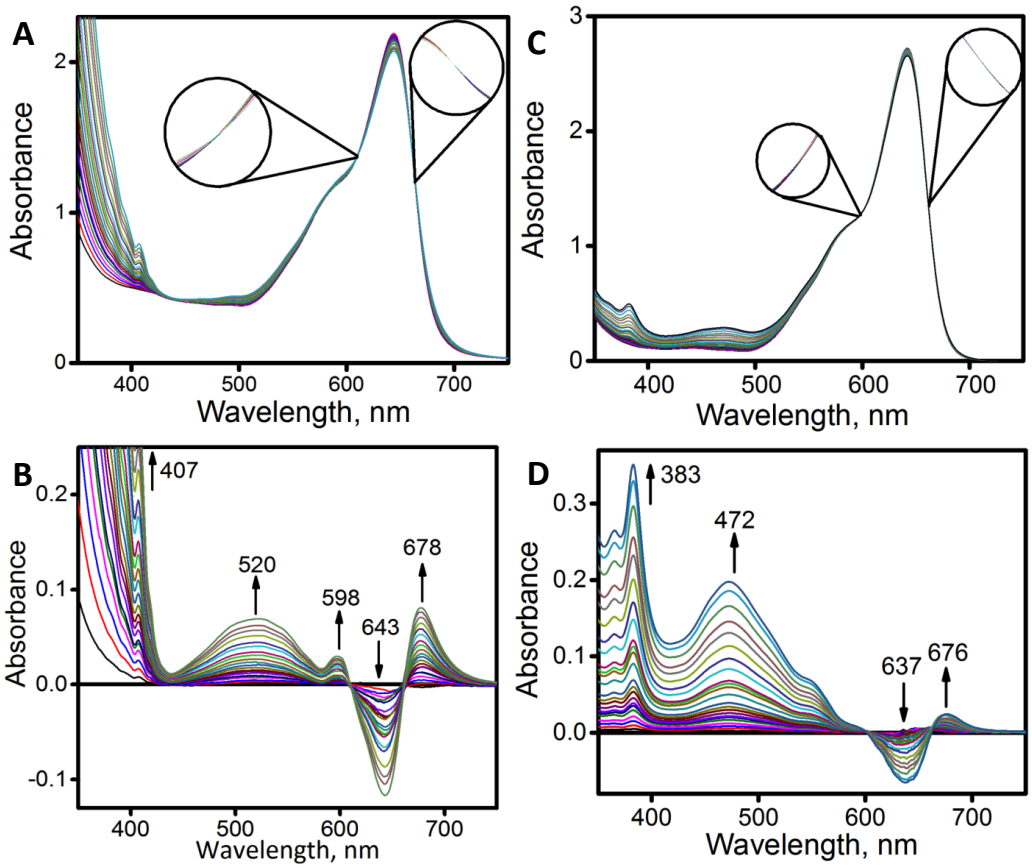

Figure 7. UV-vis (**A**, **C**) and difference (**B**, **D**) spectra of titration of subphthalocyanine **4** with C_{60} (**A**, **B**) and C_{70} (**C**, **D**) fullerenes.

Data on UV-vis titrations of the receptors **1** - **4** with C_{60} and C_{70} fullerenes in toluene are presented in Figure 7 and Supporting Information Figure S9 - S11. Each of these titrations was repeated several times for different concentrations of receptors **1** - **4** in order to assure the reproducibility of the experiments. The difference UV-vis spectra of

subphthalocyanine receptors **1** and **2** with C_{60} and C_{70} fullerenes are very similar to each other and are indicative of a growth of the corresponding fullerene spectra and very minor decrease in *Q*-band intensity (Supporting Information Figures S9 and S10). Similarly, difference UV-vis spectra of subnaphthalocyanine **3** with C_{60} and C_{70} fullerenes indicative of the growth of corresponding fullerene spectra and minor decrease of the *Q*-band intensity of a receptor (Supporting Information Figure S11). The difference UV-vis spectra of hexathiophenol-containing receptor **4** with C_{60} and C_{70} fullerenes, however, are quite different (Figure 7). In addition to the expected growth of the UV-vis spectra of C_{60} and C_{70} fullerenes, the intensity of the *Q*-band in receptor **4** significantly decreases, while a new band at 678 (C_{60} titrations) or 676 (C_{70} titrations) nm appears in the UV-vis spectra (Figure 7). Clear isosbestic points at 660 and 603 nm (C_{60} titrations) or 664 and 599 nm (C_{70} titrations) were observed for these transformations and UV-vis data are reproducible for several concentrations and different samples of the subphthalocyanine **4**. Formation of the new low-energy band between 676 and 678 nm was not observed for the compounds **1** - **3** and thus one might speculate that electron-rich subphthalocyanine **4** has the largest interaction energy with C_{60} and C_{70} fullerenes. Moreover, the position of this band (which can be tentatively assigned to a charge-transfer transition from receptor **4** to the C_{60} or C_{70} fullerene) is close to the broad band observed by Konarev and co-workers between 650 and 750 nm in a solid state UV-vis spectrum of their axially linked bis(subphthalocyanine) : C_{60} non-covalent adduct.[19]

Support for this hypothesis came from the steady-state fluorescence quenching and transient absorption spectroscopy experiments. In the case of steady-state

fluorescence spectroscopy experiments (Figure 8), titration of the electron-rich subphthalocyanine **4** with with C_{60} and C_{70} fullerenes leads to clear fluorescence quenching. Although quenching is incomplete even at large excess of fullerenes, partial fluorescence quenching is indicative of an energy or electron-transfer process in non-covalent subphthalocyanine **4** : fullerene assemblies.

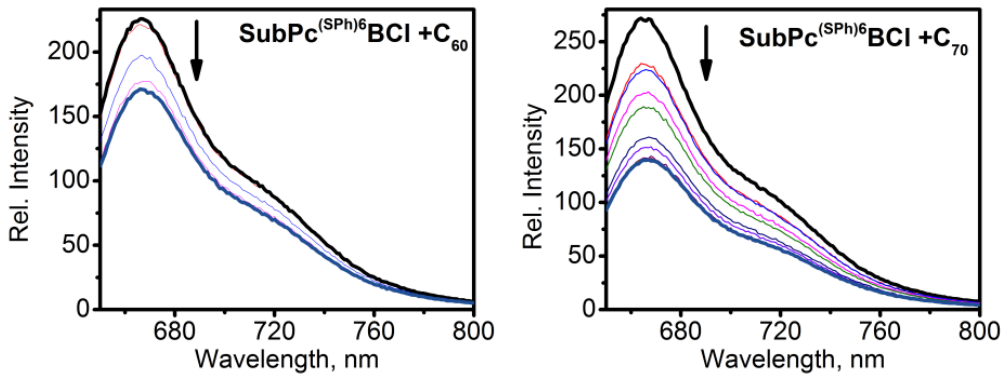

Figure 8. Steady-state fluorescence titration of subphthalocynaine **4** with C_{60} and C_{70} fullerenes.

Pump-probe spectroscopy in the visible and near-IR regions of the spectrum following excitation at the Q-band wavelength (560 nm for **1** - **2** and 622 nm for **3** - **4**) was performed on compounds **1** - **4** in toluene at concentrations of ~2 x 10^{-5} M. In the visible, the difference spectra for all compounds were the combination of a ground state bleach of the Q-band (negative DOD) and a broad excited state absorption across the visible leading to positive DOD changes on both sides of the bleach. Compounds **1** - **3** demonstrated very little change in the transient spectra as a function of probe delay on the time scale accessible to the experiments, < 1 ns, and only compound **3** had measureable

transient absorption in the near-IR that was weak, broad and featureless (see Supporting Information). There was no discernable difference in the transient spectra of compounds **1 - 3** with the addition of C_{60} or C_{70} up to a ratio of 1:10. Compound **4** showed small, but measureable changes in the visible portion of the spectrum, Figure 9(a), with decreases in the signal amplitude at all wavelengths with delay time.

The transient absorption of compound **4** in the near-IR portion of the spectrum was different than **1 - 3**. There was an isosbestic point at 1050 nm and a new broad absorption grows in centered around 1150 nm, Figure 9(b). The time dependence of the new absorption at 1150 nm is shown in Figure 10. Although the time scale was comparable to the maximum delay accessible in the experiments, we were able to fit the rise to a single exponential with a time constant of 1.4+/-0.8 ns. We assigned this new feature to the excited triplet state of **4**. Enhancement of the intersystem crossing rate relative to **1 - 3** was consistent with the expected influence of the heavier sulfur atoms. When the solution of **4** is titrated with C_{60}, a subtle, but discernable difference in the shape of the near-IR transient absorption appeared, Figure 9(c) and Supporting Information. In the presence of C_{60}, there was a consistent enhancement in the transient absorption in the region 1020 - 1120 nm relative to shorter wavelengths. This spectral region is consistent with the region previously assigned to absorption of the C_{60} anion,[47] providing additional support for the presence of **4@C$_{60}$** complexes in solution. There were no measureable pump-probe signals when C_{60} or C_{70} was examined in the absence of compounds **1 - 4**.

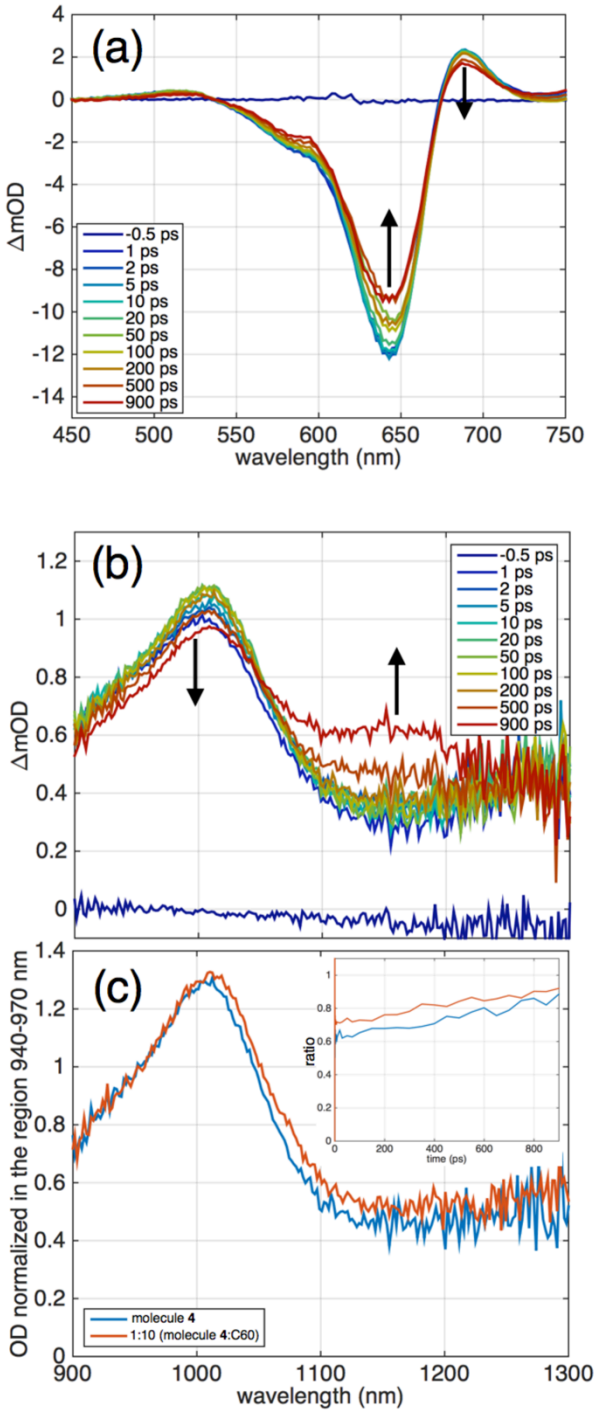

Figure 9. Transient absorption spectra of subphthalocyanine **4** in toluene. (a) The visible potion of the spectrum. (b) The near-IR portion of the spectrum. (c) A comparison of **4**

with the addition of C_{60} at a ratio of 1:10 demonstrating enhancement of the transient absorption around 1060 nm. The pump-probe delay is 200 ps. The inset shows the ratio of integrated difference signal in the regions 1060-1100 nm to 920-980 nm as a function of pump-probe delay.

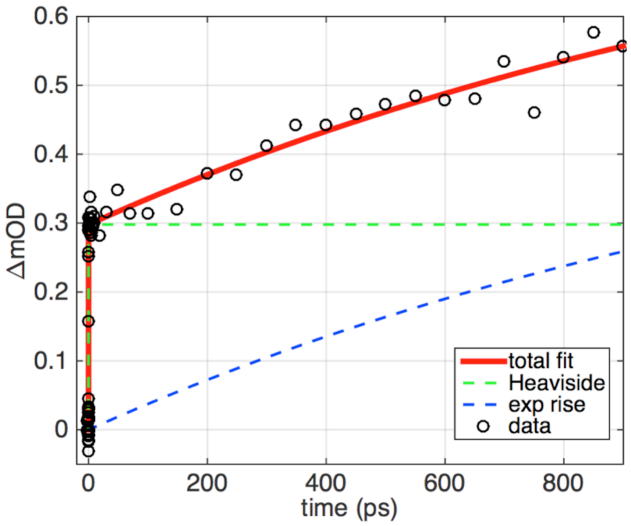

Figure 10. Transient absorption of **4** probed at 1160 nm. The fit consists of the sum of a Heaviside function and an exponential rise with a time constant of 1.4 +/- 0.8 ns (confidence interval reported at 68.2%).

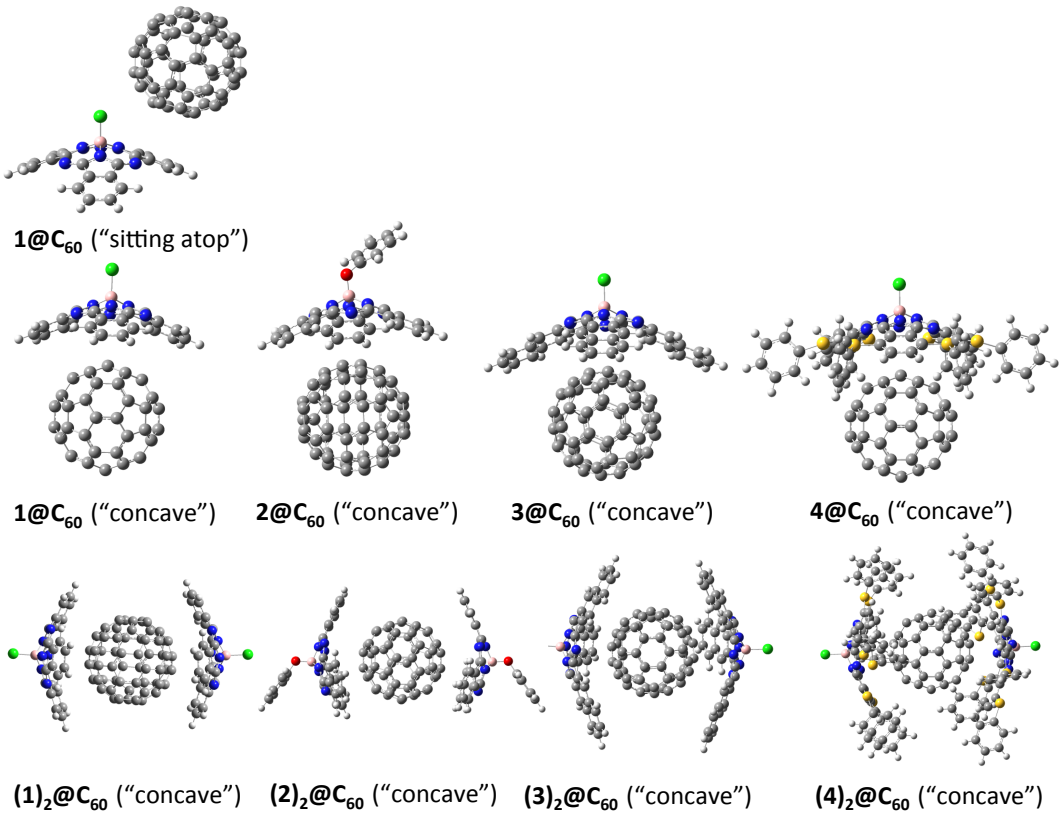

Figure 11. DFT-predicted geometries for compounds **1** - **4** and their adducts with C_{60} fullerene.

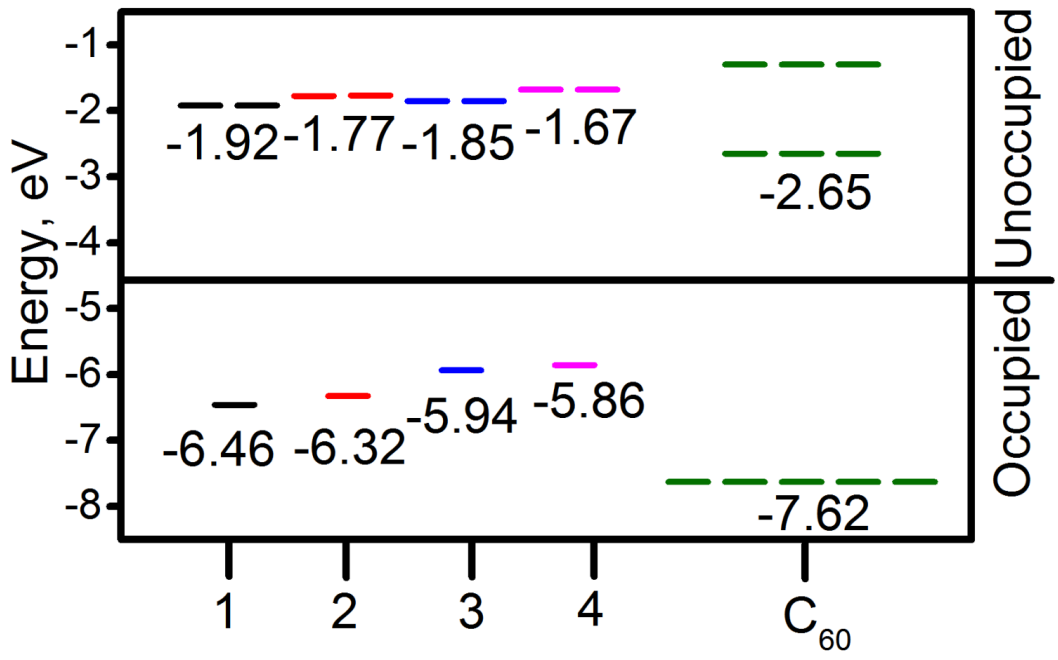

Figure 12. DFT-predicted energy diagram for individual compounds **1** - **4** and C_{60} fullerene.

DFT calculations. Further insights into the interaction energies of receptors **1** - **4** and C_{60} and C_{70} fullerenes were gained on a basis of the DFT calculations. First, we conducted several test calculations on the smallest size **1** : C_{60} system using several exchange-correlation functionals and suitable for the long-range weak interactions 6-31+(G) basis set (Supporting Information Table 1). From our test data, it is clear that the choice of exchange-correlation functional for interaction energy calculations is critical since calculated interaction energies varying between 1.54 and 28.49 kcal/mol. Although earlier,[17] based on the DFT calculations using M06-2X, Denis suggested ~20 and ~40 kcal/mol interaction energy for **2** : C_{60} and $(\mathbf{2})_2$: C_{60} complexes, our experimental data suggest weaker interaction energies for these non-covalent complexes. Based on

comparison with experimental data, only the TPSSh and CAM-B3LYP exchange-correlation functionals provide interaction energies that are physically consistent out of all tested exchange-correlation functionals. Good performance of CAM-B3LYP exchange-correlation functional is not surprising as it was specifically developed for accurate description of long-range weakly interacting systems. Using CAM-B3LYP as the functional of choice, we also tested the interaction energies of "sitting atop" and standard "concave" geometries for **1** : C_{60} non-covalent complex (Figure 11). In agreement with very recent DFT calculations on similar system,[41] the interaction energy for the "sitting atop" geometry is smaller than that for the "concave" geometry (Table 4). Next, we calculated the electronic structures of individual compounds **1** - **4** and C_{60} fullerene. DFT energy diagrams for all macrocyclic receptors and individual C_{60} fullerene are shown in Figure 12. DFT results clearly indicate that: (i) the HOMO - LUMO energy gap decreases as **1** ~ **2** > **4** > **3**; (ii) the energy of the donor HOMO increases as **1** < **2** < **3** < **4** and reflects electron-donating properties of subphthalocyanine **4**; (iii) energy of the HOMO and the LUMO in receptors **1** - **4** is always higher than the HOMO and LUMO energies in C_{60} fullerene.

Having a good choice of exchange-correlation functional and preferred "concave" geometry, we also optimized geometries for all 1 : 1 and 1 : 2 (fullerene : subphthalocyanine) non-covalent complexes between receptors **1** - **4** and C_{60} fullerene (Table 4, Figures 11 and 13). Since C_{70} fullerene is a non-spherical, larger system, and both "tip" and "flat" p-sufaces of this fullerene should be used for geometry optimization (which requires much longer computational times), additional results on interactions

between receptors **1** - **4** and C_{70} fullerene will be reported elsewhere. In the case of $(\mathbf{1})_2@\mathbf{C_{60}}$, $(\mathbf{2})_2@\mathbf{C_{60}}$, and $(\mathbf{4})_2@\mathbf{C_{60}}$ complexes, DFT predicted distances for close non-covalent contacts between subphthalocyanine macrocycle and C_{60} are in a reasonable agreement between theory and experiment. The calculated interaction energies for non-covalent 1 : 1 and 1: 2 complexes are listed in Table 4 and follow the general trend of **1** : fullerene < **2** : fullerene < **3** : fullerene < **4** : fullerene, which agrees very well with experimental observations. Indeed, according to DFT calculations, the most electron-rich receptor **4** has the highest interaction energy. DFT predicted interaction energies for compounds **1** - **3** that are within the values typical for van der Waals type interactions. The DFT-predicted interaction energies in the non-covalent 1 : 1 and 2 : 1 complexes suggest that: (i) replacing an axial chlorine ligand with a more electron-donating phenoxy group results in only minor stabilization of the receptor : C_{60} interactions; (ii) receptor **3** with an extended p-system slightly (~0.5 - 1 kcal/mol) improves the interaction energy with C_{60} fullerene; (iii) increase of the electron density on the subphthalocyanine core of **4** is the best way to improve subphthalocyanine : fullerene interactions; (iv) interaction energies in the 2 : 1 complexes are almost additive when compared to the interaction energies in 1 : 1 complexes. Overall, the DFT-predicted interaction energies for 1 : 1 and 2 : 1 complex formations between receptors **1** - **4** and C_{60} fullerenes range between ~3.5 and ~10.5 kcal/mol (Table 4). These values are slightly lower than the generally accepted threshold of ~12 - 14 kcal/mol for ESI mass spectrometry of non-covalent complexes.[42] Similar underestimation of interaction energies was observed in the case of non-covalent porphyrin : fullerene complexes, where the experimentally determined range of

interaction energies is between 17 and 34 kcal/mol.[43,44]

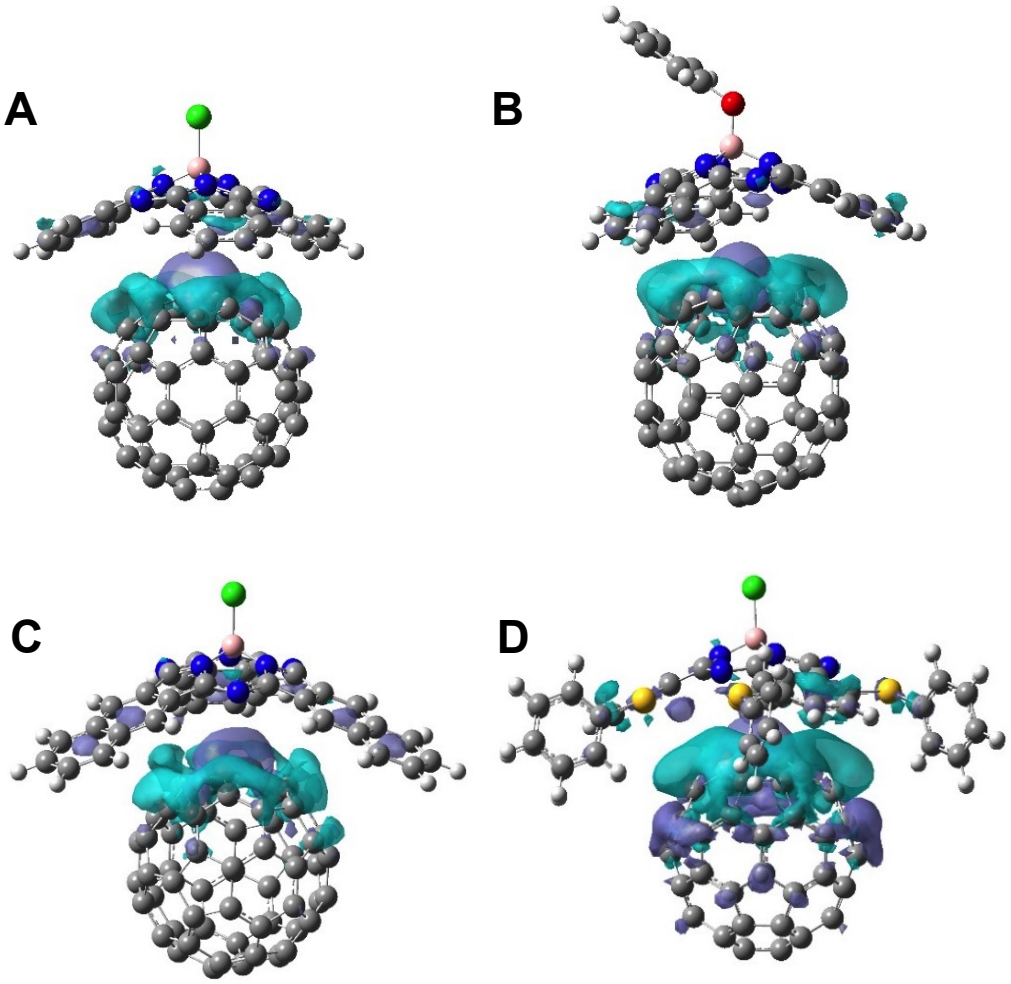

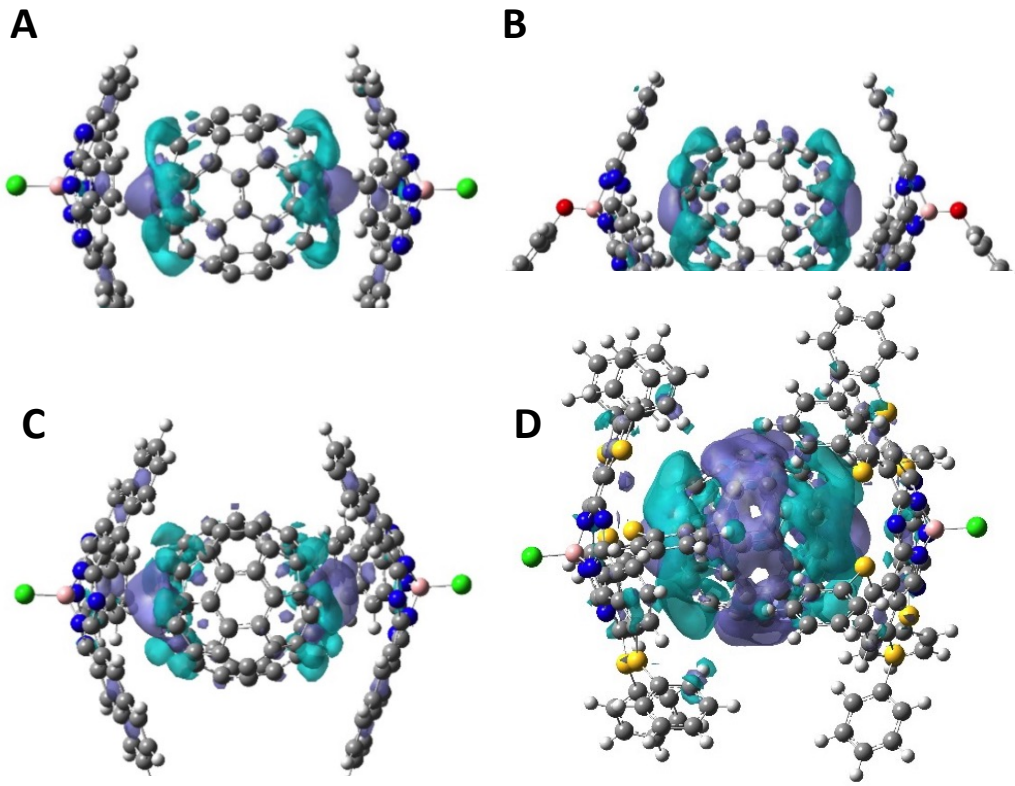

Figure 13. DFT-calculated charge density isosurfaces for 1 : 1 (top) and 2 : 1 non-covalent complexes between **1** (**A**), **2** (**B**), **3** (**C**), and **4** (**D**) and C_{60} fullerene.

The interaction between the subphtalocyanine molecules and C_{60} can be demonstrated by a charge density isosurface. The difference in charge density (excess and depletion electrons) has been estimated by:[48]

$$\Delta\rho = \rho(C_{60}{+}subphtal) - (\rho(C_{60}) + \sum_{k=1}^{2} \rho_k(subphtal)), \qquad (1)$$

where $\rho(C_{60}{+}subphtal)$ is a total electron density of complex, $\rho(C_{60})$ and $\rho_k(subphtal)$ are the total electron densities of fullerene and subphtalocyanine molecule, respectively, and k is number subphtalocyanine molecules in the complex. The results for the non-covalent

1 : 1 complexes are shown in Figure 13. In all cases, the charge density isosurface shows only charge redistribution in individual subphtalocyanine and C_{60} molecules, indicating only van der Waals type interaction between them. The main motif of the van der Waals complex formation between receptors **1** - **4** and C_{60} fullerene is the redistribution of electron density at the C_{60} fullerene from its periphery to the center point and accumulation of the electron density at the center of benzene rings in receptors **1** - **4**. Since three additional benzene fragments are present in subnaphthalocyanine **3**, it is not surprising that all of them contribute to van der Waals interactions between this receptor and C_{60} thus increasing the total interaction energy by ~1 kcal/mol compared to the **1** : C_{60} complex. In the case of subphthalocyanine **4**, additional van der Waals interactions come from the thiophenol fragments (depletion of electron density) and periphery of the C_{60} fullerene (increase of electron density). Such type of electron density redistribution is not present in any other tested systems and is, most likely, responsible for the highest interaction energy predicted for **4** : C_{60} system. The excess of electron density is accumulated on the part of the molecules located closest to subphptalocyanine. Overall, charge density isosurface plots indicate that the van der Waals interaction between receptors **1** - **4** and C_{60} fullerene should follow **1** < **2** < **3** < **4** trend, which is in a good agreement with the interaction energy DFT calculations and experimental data.

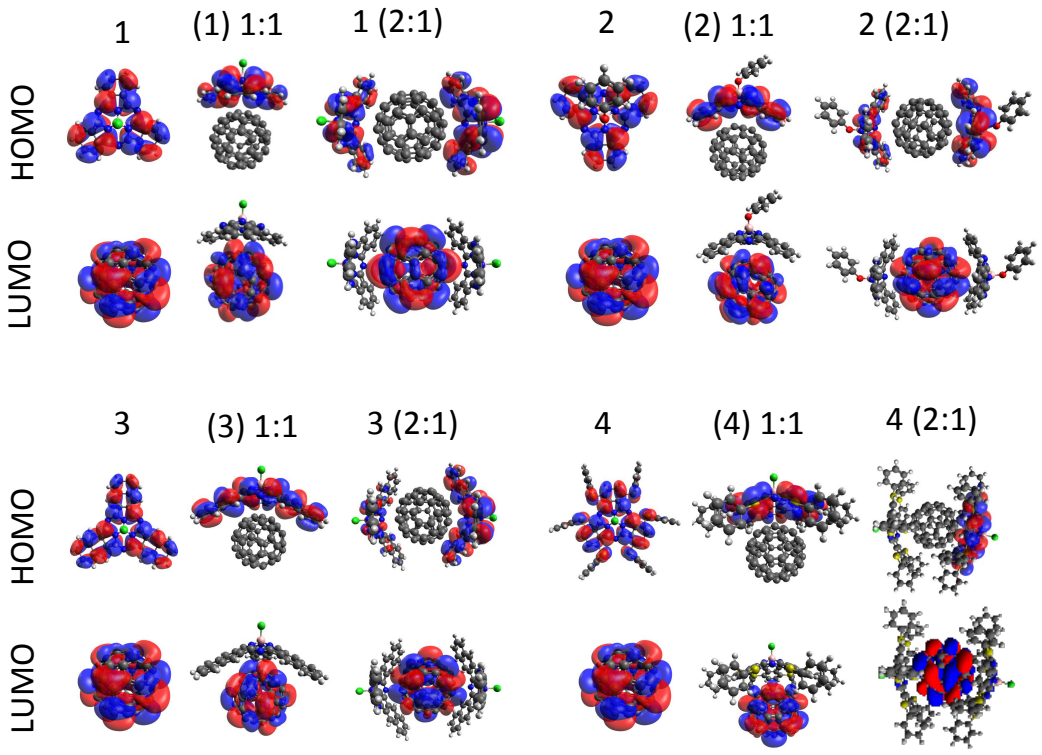

Figure 14. DFT-predicted frontier orbitals of compounds **1** - **4**, C_{60} fullerene and their non-covalent complexes.

Table 4. DFT-predicted interaction energies (kcal/mol) for non-covalent 1 : 1 and 1 : 2 complexes with and without ZPE correction.

Complex	Energy without ZPE	Energy with ZPE
1@C$_{60}$ [a]	-2.42	-3.51
2@C$_{60}$	-2.80	-3.64
3@C$_{60}$	-3.25	-4.12
4@C$_{60}$	-4.92	-5.71

(1)$_2$@C$_{60}$	-5.11	-5.71
(2)$_2$@C$_{60}$	-5.35	-5.93
(3)$_2$@C$_{60}$	-6.26	-6.88
(4)$_2$@C$_{60}$	-9.68	-10.09
1@C$_{60}$ [b]	-1.71	-2.56

[a] "concave" geometry; [b] "sitting atop" geometry.

Analysis of the HOMO and LUMO in all non-covalent assemblies is provided in Figures 14 and 15. In all cases, the HOMO is localized at the macrocyclic receptor, while the LUMO localized on the C_{60} fullerene. In general, the energies of the frontier MOs in all non-covalent assemblies are close to those in the individual components with the largest deviation (~0.2 eV) observed for **4@C$_{60}$** and **(4)$_2$@C$_{60}$** non-covalent assemblies. Such small deviations are in better agreement with a van der Waals description of the interaction rather than any strong charge-transfer character. The energies of the macrocycle-centered receptor's HOMO in non-covalent assemblies increase in the order of **1** < **2** < **3** < **4**, which is also consistent with their affinity toward fullerenes (Figure 14). DFT calculations of the non-covalent assemblies also suggest that the energy of subphthalocyanine-to-fullerene charge-transfer band should be lower than the energy of *Q*-band of corresponding compounds **1** - **4**, which agrees well with the experimentally observed low-energy band between 650 and 750 nm.[19]

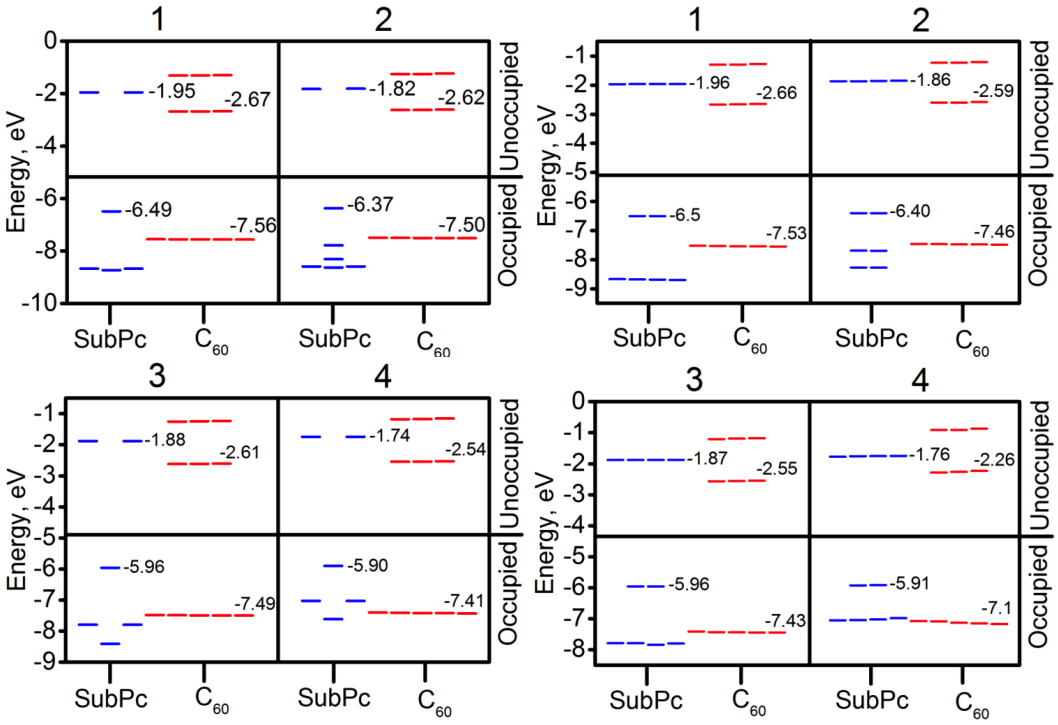

Figure 15. DFT-predicted energy diagram for non-covalent 1 : 1 (left) and 1 : 2 (right) complexes.

CONCLUSIONS:

Four subphthalocyanine-based compounds **1** - **4** were tested as potential receptors for C_{60} and C_{70} fullerenes in a solid state and solution. X-ray crystal structures of the electron-rich hexathiophenol subphthalocyanine **4** and its **4@C$_{60}$** fullerene adduct were discussed. The **4@C$_{60}$** fullerene adduct structure reveals two major types of non-covalent interactions: (i) "concave" accommodation of a single fullerene molecule between two subphthalocyanine molecules and (ii) weak interaction between isoindole fragments of subphthalocyanine and "sitting atop" fullerene molecules. Solution non-covalent interactions between receptors **1** - **4** and C_{60} or C_{70} fullerenes were probed by UV-vis,

APCI, ESI and CSI spectroscopy and their photophysical properties were investigated using steady-state fluorescence and transient absorption spectroscopy. ESI and CSI experiments suggest the presence of 1 : 1 (ESI and CSI) and 1 : 2 (CSI, fullerene : receptor) non-covalent complexes between fullerenes and receptors. UV-vis and steady-state fluorescence experiments indicate that the electron-rich receptor **4** has the highest interaction energy with C_{60} and C_{70} fullerenes. Transient absorption spectra reveal partial formation of the charge-separated state between the electron-rich receptor **4** and C_{60} and C_{70} fullerenes. DFT calculations using the CAM-B3LYP exchange-correlation functional and the 6-31+d(G) basis set are in agreement with experimental data and indicate the following trend in interaction energies between receptor and fullerene: **1** < **2** < **3** < **4**. DFT calculations are suggestive of weak (~3.5 - 10.5 kcal/mol) van der Waals interactions between subphthalocyanine and fullerene. Based on experimental and theoretical data in this report one can propose a rational design of a subphthalocyanine-based receptor for fullerene.

Bibliography:

Chapter One References:

(1) (a) Johnson, A.W.; Kay, I. T. *Proc. Chem. Soc. London* **1964,** *89,* 211-214. (b) Johnson, A. W.; Kay, I. T. *J. Chem. Soc.* **1965**, 1620-1629. (c) A. W. Johnson, I. T. Kay, *Proc. R. Soc. London, Ser. A: Math. Phys. Sci.* **1965,** *288,* 334-341.

(2) (a) Gross, Z.; Galili, N.; Saltsman, I. *Angew. Chem., Int. Ed.* **1999,** *38*, 1427-1429. (b) Gross,Z.; Galili, N.; Simkhovich, L.; Saltsman, I.; Botoshsnsky, M.; Blaser, D,; Boese, R.; Goldberg, I. *Org. Lett.* **1999,** *1,* 599-602. (c) Paolesse, R.; Jaquinod, L.; Nurco, D. J.; Mini, S.; Sagone, F.; Boschi, T.; Smith, K. M. *Chem. Commun.* ***1999,*** 1307-1308. (a) Geier, G.R III; Chick, J.F. B.; Callinan, J.B.; Reid, C.G.; Auguscinski, W.P. *J. Org. Chem.* **2004,** ***69****,* 4159-4169. (b) Braaten, K.C.; Gordon, D.G.; Aphibal, M.M.; Geier, G.R. III. *Tetrahedron* **2008,** *64,* 9828-9836. (c) Koszarna, B.; Gryko, D. T. *J. Org. Chem.* **2006,** *71,* 3707-3717. (d) Gryko, D.T. *J. Porphyrins Phthalocyanines* **2008,** *12,* 906-917.

(3) (a) Ngo, T. H.; Puntoriero, F.; Nastasi, F.; Robeyns, K.; Van Meervelt, L.; Campagna, S.; Dehaen, W.; Maes, W. *Chem. Eur. J.* **2010,** *16,* 5691-5705.(b) Tasior, M.; Gryko, D. T.; Pielacinska, D.; Zanelli, A.; Flamigni, L. *Chem. Asian J.* **2010,** *5,* 130-140. (c) Tasior, M.; Gryko, D. T.; Cembor, M; Jaworski, J. S.; Ventura, B.; Flamigni, L. *New J. Chem.* **2007,** *31,* 247-259. (d) Flamigni, L.; Ventura, B.; Tasior, M.; Gryko, D. T. *Inorg. Chim. Acta*. **2007,** *360,* 803-813. (e) Ventura, B.; Esposti, A.D.; Koszarna, B.; Gryko, D.T.; Flamigni, L. *New J. Chem.* 2005, **29**, 1559-1566. (f) Ding, T.; Aleman, E. A.; Modarelli, D. A.; Ziegler, C. J.; *J. Phys. Chem. A.* **2005**, *109,* 7411-7414. (g) Pomarico, G.; Vecchi, A.; Mandoj, F.; Bortolini, O.; Cicero, D. O.; Galloni, P.; Paolesse, R. *Chem. Commun.* **2014**, *50*, 4076-4078. (h) Vestfrid, J.; Goldberg, I.; Gross, Z. *Inorg. Chem.* **2014**, *53*, 10536-10542. (i) Santos, C. I. M.; Oliveira, E.; Barata, J. F. B.; Faustino, M. A. F.; Cavaleiro, J. A. S.; Neves, M. G. P. M. S.; Lodeiro, C. *Inorg. Chim. Acta.* **2014**, *417*, 148-154.

(4) (a) Gouterman, M. *J. Mol. Spectrosc*. **1961,** *6,* 138-163. (b) Gouterman, M.; Wagnière, G.H.; Snyder, L.C. *J. Mol. Spectrosc.* **1963,** *11,* 108-127.

(5) Ding, T.; Harvey, J.D.; Ziegler, C.J. *J. Porphyrins Phthalocyanines* **2005**, *9*, 22-27.

(6) (a) Gross, Z.; Simkhovichm, L.; Galili, N. *Chem. Commun.* **1999**, 599-600. (b) Ramdhanie, B.; Telser, J.; Caneschi, A.; Zakharov, L N.; Rheingold, A. L.; Goldberg, D. P. *J. Am. Chem. Soc.* **2004,** *126,* 2515-2525. (c) Collman, J.P.; Kaplum, M.; Decréau, R.A. *Dalton Trans*. 2006, 554-559. (d) Aviv, I.; Gross, Z. *Synlett*. **2006,** *6,* 951-953. (e) Simkhovich,L.; Gross, Z. *Tetrahedron Lett.* **2001,** *42,* 8089-8092. (f) Ou, Z.; Lu, A.; Meng, D.; Huang, S.; Fang, Y.; Lu, G.; Kadish, K. M. *Inorg. Chem.* **2012**, *51*, 8890-8896. (g) Chattopadhyay, P.; Matsuo, T.; Tsuji, T.; Ohbayashi, J.; Hayashi, T. *Organometallics* **2011**, *30*, 1869-1873. (h) Dogutan, D. K.; Stoian, S. A.; McGuire, R.; Schwalbe, M.; Teets, T. S.; Nocera, D. G. *J. Am. Chem. Soc.* **2011**, *133*, 131-140.

(7) (a) Mahammed, A.; Weaver, J. J.; Gray, H. B.; Abdelas, M.; Gross, Z. *Tetrahedron Lett.* **2003,** *44,* 2077-2079. (b) Li, C-Y.; Zhang, X-B.; Han, Z-X.; Akermark,

B.; Sun, L.; Shen, G-L.; Yu, R-Q. *Analyst*, **2006**, *133*, 388-393. (c) Zhang, X-B.; Han, Z-X.; Fang, Z-H.; Shen, G-L.; Yu, R-Q. *Anal. Chim. Acta*. **2006**, *562*, 210-215. (d) Radecki, J.; Dehaen, W. *Comb. Chem. High Throughput Screening* **2006,** *9,* 399-406. (e) J. Radecki, I. Stenka, E. Dolusic, W. Dehaen, *Electrochim. Acta,* 2006, **51**, 2282; (f) Yang, S.; Wo, Y.; Meyerhoff, M. E. *Analyt. Chim. Acta* **2014**, *843*, 89-96.

(8) (a) Gross, Z. *J. Biol. Inorg. Chem.* **2001,** *6,* 733-738. (b) Goldberg, D.P. *Acc. Chem. Res.* **2007,** *40,* 626-634.

(9) Ziegler, C.J.; Sabin, J.R.; Geier, G.R. III; Nemykin, V.N. *Chem. Commun.* **2012**, *48*, 4743-4745.

(10) Liang, X.; Mack, J.; Zheng, L-M.; Shen, Z.; Kobayashi, N.; *Inorg. Chem.* **2014**, *53*, 2797–2802.

(11) (a) Wasbotten, I. H.; Wondimagegn, T.; Ghosh, A. *J. Am. Chem. Soc.* **2002**, *124*, 8104-8116. (b) Gryko, D. T.; Koszarna, B. *Org. Biomol. Chem.* **2003**, *1*, 350-357.

(12) (a) Sripothongnak, S.; Ziegler, C. J.; Dahlby, M. R.; Nemykin, V. N. *Inorg. Chem.* **2011**, *50*, 6902-6909. (b) Muranaka, A.; Homma, S.; Maeda, H.; Furuta, H.; Kobayashi, N. *Chem. Phys. Lett.* **2008**, *460*, 495-498.

(13) (a) Waluk, J.; Michl, J. *J. Org. Chem.* **1991,** *56,* 2729-2735. (b) Michl, J. *J. Am. Chem. Soc.* **1978,** *100,* 6801-6811. (f) Michl, J. *J. Am. Chem. Soc.* **1978,** *100,* 6812-6818.

(14) (a) Simkhovich, L.; Galili, N.; Saltsman, I.; Goldberg, I.; Gross, Z. *Inorg. Chem*. **2000,** *39,* 2704-2705. (b) Simkhovich, L.; Mahammed, A.; Goldberg, I.; Gross, Z. *Chem. Eur. J.* **2001,** *7,* 1041-1055. (c)Bendix, J.; Dmochowski, I.J.; Gray, H.B.; Mahammed, A.; Simkhovich, L.; Gross, Z. *Angew. Chem. Int. Ed.* **2000,** *39,* 4048-4051.

(15) (a) Kobayashi, N.; Muranaka, A.; Mack, J. *Circular Dichroism and Magnetic Circular Dichroism Spectroscopy for Organic Chemists*, RSC London, UK, **2012**, 216. (b) Mason, W. R. *A Practical Guide to Magnetic Circular Dichroism Spectroscopy*, John Wiley & Sons, Inc., Hoboken, N. J.; **2007**, 223.

(16) Frisch, M. J.; Trucks, G. W.; Schlegel, H. B.; Scuseria, G. E.; Robb, M. A.; Cheeseman, J. R.; Scalmani, G.; Barone, V.; Mennucci, B.; Petersson, G. A.; Nakatsuji, H.; Caricato, M.; Li, X.; Hratchian, H. P.; Izmaylov, A. F.; Bloino, J.; Zheng, G.; Sonnenberg, J. L.; Hada, M.; Ehara, M.; Toyota, K.; Fukuda, R.; Hasegawa, J.; Ishida, M.; Nakajima, T.; Honda, Y.; Kitao, O.; Nakai, H.; Vreven, T.; Montgomery, J. A., Jr.; Peralta, J. E.; Ogliaro, F.; Bearpark, M.; Heyd, J. J.; Brothers, E.; Kudin, K. N.; Staroverov, V. N.; Kobayashi, R.; Normand, J.; Raghavachari, K.; Rendell, A.; Burant, J. C.; Iyengar, S. S.; Tomasi, J.; Cossi, M.; Rega, N.; Millam, N. J.; Klene, M.; Knox, J. E.; Cross, J. B.; Bakken, V.; Adamo, C.; Jaramillo, J.; Gomperts, R.; Stratmann, R. E.; Yazyev, O.; Austin, A. J.; Cammi, R.; Pomelli, C.; Ochterski, J. W.; Martin, R. L.; Morokuma, K.; Zakrzewski, V. G.; Voth, G. A.; Salvador, P.; Dannenberg, J. J.; Dapprich, S.; Daniels, A. D.; Farkas, Ö.; Foresman, J. B.; Ortiz, J. V.; Cioslowski, J.; Fox, D. J. Gaussian 09, revision D.01; Gaussian, Inc.: Wallingford, CT, **2009**.

(17) Tao, J.; Perdew, J. P.; Staroverov, V. N.; Scuseria, G. E. *Phys. Rev. Lett*. **2003**, *91*,146401-146405.

(18) Wachters, A. J. H. *J. Chem. Phys*. **1970**, *52*, 1033−1036.

(19) McLean, A. D.; Chandler, G. S. *J. Chem. Phys*. **1980**, *72*, 5639− 5648.

(20) Tomasi, J.; Mennucci, B.; Cammi, R. *Chem. Rev.* **2005**, *105*, 2999-3093.

(21) Tenderholt, A. L. QMForge, version 2.1; Stanford University: Stanford, CA, **2011**.

(22) (a) Mack, J.; Asano, Y.; Kobayashi, N.; Stillman, M. J. *J. Am. Chem. Soc.* **2005**, *127*, 17697-17711. (b) Mack, J.; Bunya, M.; Shimizu, Y.; Uoyama, H.; Komobuchi, N.; Okujima, T.; Uno, H.; Ito, S.; Stillman, M. J.; Ono, N.; Kobayashi, N. *Chem. Eur. J.* **2008**, *14*, 5001-5020.

(23) (a) Wang, J.-J.; Liu, C.; Wu, J.; Liu, R.-R.; Zhang, P. *J. Heterocyclic Chem.* **2014**, *51*, 392-397. (b) Ogikubo, J.; Meehan, E.; Engle, J. T.; Ziegler, C. J.; Bruckner, C. *J. Org. Chem.* **2013**, *78*, 2840-2852. (c) Ryppa, C.; Niedzwiedzki, D.; Morozowich, N. L.; Srikanth, R.; Zeller, M.; Frank, H. A.; Bruckner, C. *Chem. Eur. J.* **2009**, *15*, 5749-5762.

(24) Ziegler, C. J.; Erickson, N. R.; Dahlby, M. R.; Nemykin, V. N. *J. Phys. Chem. A* **2013**, *117*, 11499-11508.

(25) (a) DiPasquale, A. G.; Mayer, J. M. *J. Am. Chem. Soc.* **2008**, *130*, 1812-1813. (b) Coutsolelos, A.; Guilard, R.; Bayeul, D.; Lecomte, C. *Polyhedron* **1986**, *5,* 1157-164.

(26) Mahammed A.; Giladi, I.; Goldberg, I.; Gross, Z. *Chem. Eur. J.* **2001**, *7*, 4259-4265.

(27) Murakami, Y.; Yamada, S.; Matsuda, Y.; Sakata, K. *Bull. Chem. Soc. Japan* **1978**, *51*, 123-129.

(28) Nyokong, T.; Isago, H. *J. Porphyrins Phthalocyanines* **2004,** *8,* 1083-1090.

(29) Taube, H. *Chem. Rev.* **1952,** *50,* 69–126.

(30) Thomson, A.J.; Gadsby, P.M.A. *Dalton Trans.* **1990,** 1921-1928; (b) Yamamoto, T.; Nozawa, T.; Kobayashi, N.; Hatano, M. *Bull. Chem. Soc. Jpn.* **1982**, *55*, 3059-3063; (c) Kobayashi, N.; Nozawa, T.; Hatano, M. *Bull. Chem. Soc. Jpn.* **1981**, *54*, 919 – 924.

(31) (a) Lei, H.; Han, A.; Li, F.; Zhang, M.; Han, Y.; Du, P.; Lai, W.; Cao, R. *Phys. Chem. Chem. Phys.* **2014**, *16*, 1883-1893; (b) Nardis, S.; Cicero, D. O.; Licoccia, S.; Pomarico, G.; Berionni Berna, B.; Sette, M.; Ricciardi, G.; Rosa, A.; Fronczek, F. R.; Smith, K. M.; Paolesse, R. *Inorg. Chem.* **2014**, *53*, 4215-4227. (c) Conradie, J.; Ghosh, A. *Inorg. Chem.* **2011**, *50*, 4223-4225.

(32) (a) Ghosh, A.; Wondimagegn, T.; Parusel, A. B. J. *J. Am. Chem. Soc.* **2000**, *122*, 5100-5104. (b) Bendix, J.; Dmochowski, I. J.; Gray, H. B.; Mahammed, A.; Simkhovich, L.; Gross, Z. *Angew. Chem., Int. Ed.* **2000**, *39*, 4048-4051.

(33) (a) Rovira, C.; Kunc, K.; Hutter, J.; Parrinello, M. *Inorg. Chem.* **2001**, *40*, 11-17.

(34) (a) Hocking, R. K.; DeBeer George, S.; Gross, Z.; Walker, F. A.; Hodgson, K. O.; Hedman, B.; Solomon, E. I. *Inorg. Chem.* **2009**, *48*, 1678-1688. (b) Ye, S.; Tuttle, T.; Bill, E.; Simkhovich, L.; Gross, Z.; Thiel, W.; Neese, F. *Chem. Eur. J.* **2008**, *14*, 10839-10851.

(35) (a) Vale, L.S.H.P.; Barata, J.F.B.; Santos, C.I.M.; Neves, M.G.P.M.S.; Faustino, M.A.F.; Tomé, A.C.; Silva, A.M.S.; Paz, F.A.A.; Cavaleiro, J.A.S. *J. Porphyrins Phthalocyanines* **2009**, *13*, 358-368. (b) Simkhovich, L.; Goldberg, I.; Gross, Z. *Inorg. Chem.*, **2002**, *41*, 5433-5439.

Chapter Two References:

(1) Battersby, A. R. Tetrapyrroles: the pigments of life. *Nat. Prod. Rep.* **2000**, *17*, 507-526.

(2) Murphy, M. J.; Siegel, L. M.; Tove, S. R.; Kamin, H. Siroheme: A New Prosthetic Group Participating in Six-Electron Reduction Reactions Catalyzed by Both Sulfite and Nitrite Reductases. *Proc. Natl. Acad. Sci. U.S.A.* **1974**, *71*, 612-616.

(3) Scott, A. I.; Irwin, A. J.; Siegel, L. M.; Shoolery, J. N. Sirohydrochlorin. Prosthetic Group of Sulfite and Nitrite Reductases and its Role in the Biosynthesis of Vitamin B_{12}. *J. Am. Chem. Soc.* **1978**, *100*, 7987-7994.

(4) *Chlorophylls*; Scheer, H., Ed.; CRC Press: Boca Raton, 1991.

(5) Scheer, H.: An Overview of Chlorophylls and Bacteriochlorophylls: Biochemistry, Biophysics, Functions, and Applications. In *Chlorophylls and Bacteriochlorophylls*; Grimm, B., Porra, R. J., Rüdiger, W., Scheer, H., Eds.; Advances in Photosynthesis and Respiration 25; Springer: Dordrecht, NL, 2006; pp 1-26.

(6) Agius, L.; Ballantine, J. A.; Ferrito, V.; Jaccarani, V.; Murray-Rust, P.; Pelter, A.; Psaila, A. F.; Schembri, P. J. The Structure and Physiological Activity of Bonellin - A Unice Chlorin Derived from *Bonellia viridis*. *Pure Appl. Chem.* **1979**, *51*, 1847-1864.

(7) (a)Bible, K. C.; Buytendorp, M.; Zierath, P. D.; Rinehart, K. L. Tunichlorin: a nickel chlorin isolated from the Caribbean tunicate Trididemnum solidum. *Proc. Natl. Acad. Sci. U.S.A.* **1988**, *85*, 4582-4586. (b) Sings, H. L.; Bible, K. C.; Rinehart, K. L. Acyl tunichlorins: a new class of nickel chlorins isolated from the Caribbean tunicate Trididemnum solidum. *Proc. Natl. Acad. Sci. U.S.A.* **1996**, *93*, 10560-10565.

(8) Prinsep, M. R.; Caplan, F. R.; Moore, R. E.; Patterson, G. M. L.; Smith, C. D. 'Tolyporphin, a Novel Multidrug Resistance Reversing Agent from the Blue-Green Alga Tolypothrix nodosa' J. Am. Chem. Soc. 1992, 114, 385.

(9) Brückner, C.; Samankumara, L.; Ogikubo, J.: Syntheses of Bacteriochlorins and Isobacteriochlorins. In *Handbook of Porphyrin Science*; Kadish, K. M., Smith, K. M., Guilard, R., Eds.; World Scientific: River Edge, NY, 2012; Vol. 17 (Synthetic Developments, Part II; Chapter 76); pp 1–112.

(10) (a) Gouterman, M. J. In: *The Porphyrins*; Dolphin, D., Ed.; Academic Press: New York, **1978**; Vol. III, pp 1-165. (b) Seybold, P. G.; Gouterman, M. *J. Mol. Spectrosc.* **1969**, *31*, 1–13. (c) Gouterman, M. *J. Mol. Spectrosc.* **1961**, *6*, 138–163.

(11) Chorghade, M. S.; Hill, D. R.; Lee, E. C.; Pariza, R. J.; Dolphin, D. H.; Hino, F.; Zhang, L.-Y. Metalloporphyrins as chemical mimics of cytochrome P-450 systems. *Pure Appl. Chem.* **1996**, *68*, 753-756.

(12) Barona-Castano, J. C.; Carmona-Vargas, C. C.; Brocksom, T. J.; de Oliveira, K. T. Porphyrins as Catalysts in Scalable Organic Reactions. *Molecules* **2016**, *21*.

(13) Urbani, M.; Grätzel, M.; Nazeeruddin, M. K.; Torres, T. Meso-Substituted Porphyrins for Dye-Sensitized Solar Cells. *Chem. Rev.* **2014**, *114*, 12330-12396.

(14) Donnelly, R. F.; McCarron, P. A.; Tunney, M. M. Antifungal photodynamic therapy. *Microbiol. Res.* **2008**, *163*, 1-12.

(15) O'Connor, A. E.; Gallagher, W. M.; Byrne, A. T. Porphyrin and Nonporphyrin Photosensitizers in Oncology: Preclinical and Clinical Advances in Photodynamic Therapy. *Photochem. Photobiol.* **2009**, *85*, 1053–1074.

(16) Sessler, J. L.; Hemmi, G.; Mody, T. D.; Murai, T.; Burrell, A.; Young, S. W. Texaphyrins: Synthesis and Applications. *Acc. Chem. Res.* **1994**, *27*, 43-50.

(17) Lindsey, J. S.; Bocian, D. F. Molecules for Charge-Based Information Storage. *Acc. Chem. Res.* **2011**, *44*, 638–650.

(18) Huang, H.; Song, W.; Rieffel, J.; Lovell, J. F. Emerging applications of porphyrins in photomedicine. *Frontiers Phys.* **2015**, *3*.

(19) Oliveira, K. T. d.; Momo, P. B.; Assis, F. F. d.; Ferreira, M. A. B.; Brocksom, T. J. Chlorins: Natural Sources, Synthetic Developments and Main Applications. *Curr. Org. Synth.* **2014**, *11*, 42–58.

(20) Galezowski, M.; Gryko, D. T. Recent advances in the synthesis of hydroporphyrins. *Curr. Org. Chem.* **2007**, *11*, 1310-1338.

(21) Lindsey, J. S. De novo synthesis of gem-dialkyl chlorophyll analogues for probing and emulating our green world. *Chem Rev* **2015**, *115*, 6534-6620.

(22) Whitlock Jr., H. W.; Hanauer, R.; Oester, M. Y.; Bower, B. K. Diimide reduction of porphyrins. *J. Am. Chem. Soc.* **1969**, *91*, 7485-7489.

(23) Pereira, M. M.; Abreu, A. R.; Goncalves, N. P. F.; Calvete, M. J. F.; Simões, A. V. C.; Monteiro, C. J. P.; Arnaut, L. G.; Eusébio, M. E.; Canotilho, J. An insight into solvent-free diimide porphyrin reduction: a versatile approach for meso-aryl hydroporphyrin synthesis. *Green Chem.* **2012**, *14*, 1666–1672.

(24) Brückner, C.; Rettig, S. J.; Dolphin, D. Formation of a meso-Tetraphenylsecochlorin and a Homoporphyrin with a Twist. *J. Org. Chem.* **1998**, *63*, 2094-2098.

(25) Brückner, C.; Dolphin, D. ß,ß'-Dihydroxylation of meso-tetraphenylchlorins and metallochlorins. *Tetrahedron Lett.* **1995**, *36*, 9425-9428.

(26) Bruhn, T.; Brückner, C. Origin of the Regioselective Reduction of Chlorins. *J. Org. Chem.* **2015**, *80*, 4861-4868.

(27) Warren, M. J.; Smith, A. G., Tetrapyrroles: Birth, Life and Death. Springer: New York, 2009.

(28) Brückner, C.; Akhigbe, J.; Samankumara, L.: Syntheses and Structures of Porphyrin Analogues Containing Non-pyrrolic Heterocycles. In *Handbook of Porphyrin Science*; Kadish, K. M., Smith, K. M., Guilard, R., Eds.; World Scientific: River Edge, NY, 2014; Vol. 31; pp 1–276.

(29) Brückner, C. The Breaking and Mending of meso-Tetraarylporphyrins: Transmuting the Pyrrolic Building Blocks. *Acc. Chem. Res.* **2016**, accepted for publication (DOI: 10.1021/ar-2016-00043q).

(30) Daniell, H. W.; Williams, S. C.; Jenkins, H. A.; Brückner, C. Oxidation of meso-tetraphenyl-2,3-dihydroxychlorin: simplified synthesis of ß,ß'-dioxochlorins. *Tetrahedron Lett.* **2003**, *44*, 4045-4049.

(31) Akhigbe, J.; Luciano, M.; Zeller, M.; Brückner, C. Mono- and Bisquinoline-Annulated Porphyrins from Porphyrin β,β'-Dione Oximes. *J. Org. Chem.* **2015**, *80*, 499-511.

(32) Brückner, C.; Ogikubo, J.; McCarthy, J. R.; Akhigbe, J.; Hyland, M. A.; Daddario, P.; Worlinsky, J. L.; Zeller, M.; Engle, J. T.; Ziegler, C. J.; Ranaghan, M. J.; Sandberg, M. N.; Birge, R. R. Oxazolochlorins. 6. meso-Arylporpholactones and their Reduction Products. *J. Org. Chem.* **2012**, *77*, 6480–6494.

(33) Gouterman, M.; Hall, R. J.; Khalil, G. E.; Martin, P. C.; Shankland, E. G.; Cerny, R. L. Tetrakis(pentafluorophenyl)porpholactone. *J. Am. Chem. Soc.* **1989**, *111*, 3702-3707.

(34) Yu, Y.; Lv, H.; Ke, X.; Yang, B.; Zhang, J.-L. Ruthenium-Catalyzed Oxidation of the Porphyrin ß-ß'-Pyrrolic Ring: A General and Efficient Approach to Porpholactones. *Adv. Synth. Catal.* **2012**, *354*, 3509–3516.

(35) Akhigbe, J.; Haskoor, J. P.; Krause, J. A.; Zeller, M.; Brückner, C. Oxazolochlorins. 10. Formation, Structure and Reactivity of meso-Tetraaryl-chlorolactones, -porpholactames, and chlorolactames, Porphyrin and Chlorin Analogues Incorporating Oxazolone or Imidazolone Moieties. *Org. Biomol. Chem.* **2013**, *11*, 3616–3628.

(36) Akhigbe, J.; Ryppa, C.; Zeller, M.; Brückner, C. Oxazolochlorins. 2. Intramolecular Cannizzaro Reaction of meso-Tetraphenylsecochlorin Bisaldehyde. *J. Org. Chem.* **2009**, *74*, 4927-4933.

(37) Ogikubo, J.; Worlinsky, J. L.; Fu, Y.-J.; Brückner, C. Oxazolochlorins. 8. A Two-step, One-pot Route to Swap the Pyrroline Moiety in meso-Tetraaryldihydroxychlorins with an O /N-Substituted Oxazoline. *Tetrahedron Lett.* **2013**, *54*, 1707–1710.

(38) Ogikubo, J.; Meehan, E.; Engle, J. T.; Ziegler, C.; Brückner, C. Oxazolochlorins. 7. meso-Aryl-3-alkyl-2-oxachlorins. *J. Org. Chem.* **2012**, *77*, 6199–6207.

(39) Ogikubo, J.; Meehan, E.; Engle, J. T.; Ziegler, C. J.; Brückner, C. Oxazolochlorins. 9. meso-Tetraphenyl-2-oxabacteriochlorins and meso-Tetraphenyl-2,12/13-dioxabacteriochlorins. *J. Org. Chem.* **2013**, *78*, 2840–2852.

(40) Brückner, C.; McCarthy, J. R.; Daniell, H. W.; Pendon, Z. D.; Ilagan, R. P.; Francis, T. M.; Ren, L.; Birge, R. R.; Frank, H. A. A spectroscopic and computational study of the singlet and triplet excited states of synthetic ß-functionalized chlorins. *Chem. Phys.* **2003**, *294*, 285-303.

(41) Greco, J. A.; Shima, S.; Wagner, N. L.; McCarthy, J. R.; Atticks, K.; Brückner, C.; Birge, R. R. Two-Photon Spectroscopy of the Q-Bands of meso-Tetraphenyl-Porphyrin and -Chlorin Framework Derivatives. *J. Phys. Chem. C* **2015**, *119*, 3711-3724.

(42) (a) Mack, J.; Stillman, M. J.; Kobayashi, N. *Coord. Chem. Rev.* 2007, **251**, 429. (b) Kobayashi, N.; Nakai, K. Applications of magnetic circular dichroism spectroscopy to porphyrins and phthalocyanines *Chem. Commun.* **2007**, 4077-4092. (c) Stillman, M.; Mack, J.; Kobayashi, N. Theoretical aspects of the spectroscopy of porphyrins and phthalocyanines *J. Porphyrins Phthalocyanines* **2002**, *6*, 296-300.

(43) (a) Keegan, J. D.; Stolzenberg, A. M.; Lu, Y.-C.; Linder, R. E.; Barth, G.; Moscowitz, A.; Bunnenberg, E. Djerassi, C. Magnetic circular dichroism studies. 60. Substituent-induced sign variation in the magnetic circular dichroism spectra of reduced porphyrins. 1. Spectra and band assignments. *J. Am. Chem. Soc.* **1982**, *104*, 4305-4317. (b) Keegan, J. D.; Stolzenberg, A. M.; Lu, Y.-C.; Linder, R. E.; Barth, G.; Moscowitz, A.; Bunnenberg, E. Djerassi, C. Magnetic circular dichroism studies. 61. Substituent-induced sign variation in the magnetic circular dichroism spectra of reduced porphyrins. 2. Perturbed molecular orbital analysis. *J. Am. Chem. Soc.* **1982**, *104*, 4317-4329. (c) Ke, X.-S.; Chang, Y.; Chen, J.-Z.; Tian, J.; Mack, J.; Cheng, X.; Shen, Z.; Zhang, J.-L. Porphodilactones as synthetic chlorophylls: relative orientation of b-substituents on a pyrrolic ing tunes NIR absorption *J. Am. Chem. Soc.* **2014**, *136*, 9598-9607.

(44) (a) Waluk, J. and Michl, J. Perimeter model and magnetic circular dichroism of porphyrin analogues. *J. Org. Chem.* **1991**, *56*, 2729-2735; (b) Gorski, A.; Vogel, E.; Sessler, J. L.; and Waluk, J. Magnetic Circular Dichroism of Octaethylcorrphycene and its Doubly Protonated and Unprotonated Forms. *J. Phys. Chem. A* **2002**, *106*, 8139-8145.

(45) (a) Kitagawa, Y.; Miyatake, T.; Ishii, K. Magneto-chiral dichroism of artificial light-harvesting antenna *Chem. Commun.* **2012**, *48*, 5091-5093. (b) Sripothongnak, S.; Ziegler, C. J.; Dahlby, M. R.; Nemykin, V. N. Controllable and Reversible Inversion of the Electronic Structure in Nickel N-Confused Porphyrin: A Case When MCD Matters *Inorg. Chem.*, **2011**, *50*, 6902-6909. (c) Vecchi, A.; Erickson, N. R.; Sabin, J. R.; Floris, B.; Conte, V.; Venanzi, M.; Galloni, P.; Nemykin, V. N. Electronic properties of mono-substituted tetraferrocenyl porphyrins in solution and on gold surface: assessment of the influencing factors for photoelectrochemical applications *Chem. Eur. J.* **2015**, *21*, 269-279. (d) Rhoda, H. M.; Crandall, L. A.; Geier III, G. R.; Ziegler, C. J.; Nemykin, V. N. Combined MCD/DFT/TDDFT Study of the Electronic Structure of Axially Pyridine Coordinated Metallocorroles *Inorg. Chem.* **2015**, *54*, 4652-4662. (e)

Kon-no, M.; Mack, J.; Kobayashi, N.; Suenaga, M.; Yoza, K.; Shinmyozu, T. Synthesis, Optical Properties, and Electronic Structures of Fully Core-Modified Porphyrin Dications and Isophlorins *Chem. Eur. J.* **2012**, *18*, 13361-13371. (f) Mack, J.; Asano, Y.; Kobayashi, N.; Stillman, M. J. Application of MCD Spectroscopy and TD-DFT to a Highly Non-Planar Porphyrinoid Ring System. New Insights on Red-Shifted Porphyrinoid Spectral Bands *J. Am. Chem. Soc.* **2005**, *127*, 17697-17711.

(46) Braun, J.; Koecher, M.; Schlabach, M.; Wehrle, B.; Limbach, H.-H.; Vogel, E. NMR Study of the Tautomerism of Porphyrin Including the Kinetic HH/HD/DD Isotope Effects in the Liquid and the Solid State. *J. Am. Chem. Soc.* **1994**, *116*, 6593-6604.

(47) Gentemann, S.; Leung, S. H.; Smith, K. M.; Fajer, J.; Holten, D. Photophysical Consequences Of Porphyrin Tautomerization - Steady-State and Time-Resolved Spectral Investigations Of a Zinc Isoporphyrin. *J. Phys. Chem.* **1995**, *99*, 4330-4334.

(48) Helaja, J.; Stapelbroek-Mo¨llmann, M.; Kilpelaeinen, I.; Hynninen, P. H. NH Tautomerism in the Natural Chlorin Derivatives. *J. Org. Chem.* **2000**, *65*, 3700–3707.

(49) (a) Nemykin, V. N.; Sabin, J. R. "Profiling Energetics and Spectroscopic Signatures in Prototropic Tautomers of Asymmetric Phthalocyanine Analogues". *J. Phys. Chem. A* **2012**, *116*, 7364-7371. (b) Mack, J.; Kobayashi, N. Low symmetry phthalocyanines and their analogues. *Chem. Rev.* **2011**, *111*, 281-321. (c) Kobayashi, N.; Mack, J.; Ishii, K.; Stillman, M. J. Electronic Structure of Reduced SymmetryPeripheral Fused-Ring-Substituted Phthalocyanines. *Inorg. Chem.*, **2002**, *41*, 5350-5363. (d) Ishii, K.; Itoya, H.; Miwa, H.; Kobayashi, N. Selective detection of minor prototropic tautomers in low-symmetry tetraazaporphyrin derivatives by the combined use of electronic absorption, MCD, and CI calculations. *Chem. Commun.* **2005**, 4586-4588. (e) Qi, D.; Zhang, Y.; Cai, X.; Jiang, J.; Bai, M. Inner hydrogen atom transfer in benzo-fused low symmetrical metal-free tetraazaporphyrin and phthalocyanine analogues: Density functional theory studies. *J. Molecular Graphics Modelling* **2009**, *27*, 693-700.

(50) Adler, A. D.; Longo, F. R.; Finarelli, J. D.; Goldmacher, J.; Assour, J.; Korsakoff, L. A simplified synthesis for TPP. *J. Org. Chem.* **1967**, *32*, 476.

(51) Gaussian 09, Revision **D.1**, Frisch, M. J.; Trucks, G. W.; Schlegel, H. B.; Scuseria, G. E.; *et al* Gaussian, Inc., Wallingford CT, **2009**. *For full citation, see Supporting Information*.

(52) Tenderholt, A. L. *QMForge, Version 2.1.* Stanford University, Stanford, CA, USA.

(53) Tao, J. M.; Perdew, J. P.; Staroverov, V. N.; Scuseria, G. E. Climbing the Density Functional Ladder: Nonempirical Meta-Generalized Gradient Approximation Designed for Molecules and Solids. *Phys. Rev. Lett.* **2003**, *91*, 146401/1-146401/4.

(54) McLean, A. D.; Chandler, G. S. Contracted Gaussian basis sets for molecular calculations. I. Second row atoms, Z = 11-18. *J. Chem. Phys.* **1980**, *72*, 5639-5648.

(55) Scalmani, G.; Frisch, M. J.; Mennucci, B.; Tomasi, J.; Cammi, R.; Barone, V. Geometries and properties of excited states in the gas phase and in solution: Theory and application of a time-dependent density functional theory polarizable continuum model. *J. Chem. Phys.*, **2006**, *124*, 094107: 1-15.

Chapter Three References:

(1) (a) Yella, A.; Mai, C. L.; Zakeeruddin, S. M.; Chang, S. N.; Hsieh, C. H.; Yeh, C. Y.; Gratzel, M. *Angew. Chem. Int. Ed.* **2014**, *53*, 2973-2977. (b) Mathew, S.; Yella, A.; Gao, P.; Humphry-Baker, R.; Curchod, B.F. E.; Ashari-Astani, N.; Tavernelli, I.; Rothlisberger, U.; Nazeeruddin, M. K.; Gratzel, M. *Nature Chemistry* **2014**, *6*, 242-247. (c) Yella, A.; Lee, H. W.; Tsao, H. N.; Yi, C. Y.; Chandiran, A. K.; Nazeeruddin, M. K.; Diau, E. W. G.; Yeh, C. Y.; Zakeeruddin, S. M.; Gratzel, M. *Science* **2011**, *334*, 629-634. (d) Sun, Y.; Welch, G. C.; Leong, W. L.; Takacs, C. J.; Bazan, G. C.; Heeger, A.J. *Nature Materials* **2012**, *11*, 44–48. (e) Whittell, G. R.; Hager, M. D.; Schubert, U. S.; Manners, I. *Nature Materials* **2011**, *10*, 176–188. (f) *Electron Transfer in Chemistry*; Balzani, V., Ed.; Wiley-VCH: Weinheim, Germany, 2001; Vol. I-V. (g) Melkozernov, A. N.; Barber, J.; Blankenship, R. E. *Biochemistry* **2006**, *45*, 331–345. (h) Guenes, S.; Neugebauer, H.; Sariciftci, N. S. *Chem. Rev.* **2007**, *107*, 1324–1338. (i) Verreet, B.; Cnops, K.; Cheyns, D.; Heremans, P.; Stesmans, A.; Zango, G.; Claessens, C. G.; Torres, T.; Rand, B. P. *Adv. Energy Mater.* **2014**, *4*, 1301413.

(2) (a) Imahori, H.; Mori, Y.; Matano, Y. *J. Photochem. Photobiol. C* **2003**, *4*, 51–83. (b) Imahori, H.; Tamaki, K.; Araki, Y.; Sekiguchi, Y.; Ito, O.; Sakata, Y.; Fukuzumi, S. *J. Am. Chem. Soc.* **2002**, *124*, 5165–5174. (c) D'Souza, F.; Chitta, R.; Gadde, S.; Islam, D.-M. S.; Schumacher, A. L.; Zandler, M. E.; Araki, Y.; Ito, O. *J. Phys. Chem. B* **2006**, *110*, 25240–25250. (d) Springer, J.; Kodis, G.; De La Garza, L.; Moore, A. L.; Moore, T. A.; Gust, D. *J. Phys. Chem. A* **2003**, *107*, 3567–3575. (e) Gonza´lez-Rodrı´guez, D.; Bottari, G. *J. Porphyrins Phthalocyanines* **2009**, *13*, 624–636.

(3) *Molecular Mechanisms of Photosynthesis*; Blankenship, R. E., Ed.; Blackwell Science: Malden, MA, 2002.

(4) (a) Aratani, N.; Osuka, A. in: *Handbook of Porphyrin Science*. Kadish, K. M.; Smith, K. M.; Guilard, R. (Eds.); World Scientific Publishing Co. Pte. Ltd. 2010, Vol. 1, pp 1 – 132. (b) Balaban, T. S. in: *Handbook of Porphyrin Science*. Kadish, K. M.; Smith, K. M.; Guilard, R. (Eds.); World Scientific Publishing Co. Pte. Ltd. 2010, Vol. 1, pp 221 – 306. (c) Zhao, Z.; Cammidge, A. N.; Cook, M. J. *Chem. Commun.* **2009**, 7530-7532.

(5) (a) Yoon, Z. S.; Yang, J.; Yoo, H.; Cho, S.; Kim, D. in: *Handbook of Porphyrin Science*. Kadish, K. M.; Smith, K. M.; Guilard, R. (Eds.); World Scientific Publishing Co. Pte. Ltd. 2010, Vol. 1, pp 439 – 506. (b) Gonzalez-Rodriguez, D.; Carbonell, E.; Rojas, G. M.; Castellanos, C. A.; Guldi, D. M.; Torres, T. *J. Am. Chem. Soc.* **2010**, *132*, 16488-16500. (c) El-Khouly, M. E.; Shim, S. Hee; Araki, Y.; Ito, O.; Kay, K.-Y. *J. Phys. Chem. B* **2008**, *112*, 3910-3917. (d) Solntsev, P. V.; Sabin, J. R.; Dammer, S. J.; Gerasimchuk, N. N.; Nemykin, V. N. *Chem. Commun.* **2010**, 6581-6583.

(e) Ziessel, R.; Ulrich, G.; Elliott, K. J.; Harriman, A. *Chem. Eur. J.* **2009**, *15*, 4980-4984. (f) Mauldin, C. E.; Piliego, C.; Poulsen, D.; Unruh, D. A.; Woo, C.; Ma, B.; Mynar, J. L.; Frechet, J. M. J. *Appl. Mater. Interf.* **2010**, *2*, 2833-2838. (g) Gonzalez-Rodriguez, D.; Torres, T.; Olmstead, M. M.; Rivera, J.; Angeles Herranz, M.; Echegoyen, L.; Atienza Castellanos, C.; Guldi, D. M. *J. Am. Chem. Soc.* **2006**, *128*, 10680-10681. (h) Sanchez-Molina, I.; Grimm, B.; Calderon, R. M. K.; Claessens, C. G.; Guldi, D. M.; Torres, T. *J. Am. Chem. Soc.* **2013**, *135*, 10503-10511. (i) Sanchez-Molina, I.; Ince, M.; Bottari, G.; Georges, C.; Martinez-Diaz, M. V.; Torres, T. *Turk. J. Chem.* **2014**, *38*, 1006-1012. (j) Ince, M.; Medina, A.; Yum, J. H.; Yella, A.; Claessens, C. G.; Martinez-Diaz, M. V.; Gratzel, M.; Nazeeruddin, M. K.; Torres, T. *Chem. Eur. J.* **2014**, *20*, 2016-2021.

(6) (a) Grimm, B.; Hausmann, A.; Kahnt, A.; Seitz, W.; Spanig, F.; Guldi, D. M. in: *Handbook of Porphyrin Science*. Kadish, K. M.; Smith, K. M.; Guilard, R. (Eds.); World Scientific Publishing Co. Pte. Ltd. 2010, Vol. 1, pp 133 – 220. (b) Araki, Y.; Ito, O. *J. Photochem. Photobiol. C* **2008**, *9*, 93 –110. (c) Guldi, D. M.; Hirsch, A.; Scheloske, M.; Dietel, E.; Troisi, A.; Zerbetto, F.; Prato, M. *Chem. Eur. J.* **2003**, *9*, 4968 – 4979. (d) Albinsson, B.; Eng, M. P.; Pettersson, K.; Winters, M. U. *Phys. Chem. Chem. Phys.* **2007**, *9*, 5847 – 5864. (e) Nieto, C. R.; Guilleme, J.; Villegas, C.; Delgado, J. L.; Gonzalez-Rodriguez, D.; Martin, N.; Torres, T.; Guldi, D. M. *J. Mater. Chem.* **2011**, *21*, 15914-15918. (f) Rohde, G. T.; Sabin, J. R.; Barrett, C. D.; Nemykin, V. N. *New J. Chem.*, **2011**, *35*, 1440-1448. (g) Nemykin, V. N.; Rohde, G. T.; Barrett, C. D.; Hadt, R. G.; Sabin, J. R.; Reina, G.; Galloni, P.; Floris, B. *Inorg. Chem.* **2010**, *49*, 7497-7509. (h) Nemykin, V. N.; Rohde, G. T.; Barrett, C. D.; Hadt, R. G.; Bizzarri, C.; Galloni, P.; Floris, B.; Nowik, I.; Herber, R. H.; Marrani, A. G.; Zanoni, R.; Loim, N. M. *J. Am. Chem. Soc.* **2009**, *131*, 14969-14978. (i) Nemykin, V. N.; Galloni, P.; Floris, B.; Barrett, C. D.; Hadt, R. G.; Subbotin, R. I.; Marrani, A. G.; Zanoni, R.; Loim, N. M. *Dalton Trans.* **2008**, 4233-4246. (j) Nemykin, V. N.; Barrett, C. D.; Hadt, R. G.; Subbotin, R. I.; Maximov, A. Y.; Polshin, E. V.; Koposov, A. Y. *Dalton Trans.* **2007**, 3378-3389. (k) Vecchi, A.; Gatto, E.; Floris, B.; Conte, V.; Venanzi, M.; Nemykin, V. N.; Galloni, P. *Chem. Commun.* **2012**, *48*, 5145-5147. (l) Nemykin, V. N.; Purchel, A. A.; Spaeth, A. D.; Barybin, M. V. *Inorg. Chem.* **2013**, *52*, 11004-11012. (m) Vecchi, A.; Erickson, N. R.; Sabin, J. R.; Floris, B.; Conte, V.; Venanzi, M.; Galloni, P.; Nemykin, V. N. *Chem. Eur. J.* **2015**, *21*, 269-279. (n) Vecchi, A.; Galloni, P.; Floris, B.; Nemykin, V. N. *J. Porphyrins Phthalocyanines* **2013**, *17*, 165-196. (o) Sirbu, D.; Turta, C.; Benniston, A. C.; Abou-Chahine, F.; Lemmetyinen, H.; Tkachenko, N. V.; Wood, C.; Gibson, E. *RSC Advances* **2014**, *4*, 22733-22742.

(7) (a) D'Souza, F.; Ito, O. in: *Handbook of Porphyrin Science*. Kadish, K. M.; Smith, K. M.; Guilard, R. (Eds.); World Scientific Publishing Co. Pte. Ltd. 2010, Vol. 1, pp 307 – 438. (b) El-Khouly, M. E.; Ito, O.; Smith, P. M.; D'Souza, F. *J. Photochem. Photobiol., C* **2004**, *5*, 79–104. (c) Fukuzumi, S. *Phys. Chem. Chem. Phys.* **2008**, *10*, 2283–2297. (d) D'Souza, F.; Ito, O. *Organic Electronics and Photonics*; Nalwa, H. R., Ed.; American Scientific Publishers: Stevenson Ranch, CA, 2008; Vol. 1, Chap. 13. (e) Ohkubo, K.; Fukuzumi, S. *Bull. Chem. Soc. Japan* **2009**, *82*, 303–315.

(8) Ohkubo, K.; Kotani, H.; Shao, J.; Ou, Z.; Kadish, K. M.; Li, G.; Pandey, R.

K.; Fujitsuka, M.; Ito, O.; Imahori, H.; Fukuzumi, S. *Angew. Chem., Int. Ed.* **2004**, *43*, 853-856.

(9) (a) Verreet, B.; Rand, B. P.; Cheyns, D.; Hadipour, A.; Aernouts, T.; Heremans, P.; Medina, A.; Claessens, C. G.; Torres, T. *Adv. Energy Mater.* **2011**, *1*, 565-568. (b) Luhman, W. A.; Holmes, R. J. *Adv. Funct. Mater.* **2011**, *21*, 764-771. (c) Shimizu, S.; Nakano, S.; Hosoya, T.; Kobayashi, N. *Chem. Commun.* **2011**, *47*, 316-318. (d) Gonzalez-Rodriguez, D.; Carbonell, E.; Guldi, D. M.; Torres, T. *Angew. Chem., Int. Ed.* **2009**, *48*, 8032-8036. (e) Verreet, B.; Schols, S.; Cheyns, D.; Rand, B. P.; Gommans, H.; Aernouts, T.; Heremans, P.; Genoe, J. *J. Mater. Chem.* **2009**, *19*, 5295-5297. (f) Gonzalez-Rodriguez, D.; Torres, T.; Herranz, M. A.; Echegoyen, L.; Carbonell, E.; Guldi, D. M. *Chem. Eur. J.* **2008**, *14*, 7670-7679. (g) Kim, J.-H.; El-Khouly, M. E.; Araki, Y.; Ito, O.; Kay, K.-Y. *Chem. Lett.* **2008**, *37*, 544-545. (h) Iglesias, R. S.; Claessens, C. G.; Rahman, G. M. A.; Herranz, M. A.; Guldi, D. M.; Torres, T. *Tetrahedron* **2007**, *63*, 12396-12404. (i) Claessens, C. G.; Gonzalez-Rodriguez, D.; Iglesias, R. S.; Torres, T. *C. R. Chimie* **2006**, *9*, 1094-1099. (j) Claessens, C. G.; Torres, T. *Chem. Commun.* **2004**, 1298-1299. (k) Gonzalez-Rodriguez, D.; Torres, T.; Guldi, D. M.; Rivera, J.; Herranz, M. A.; Echegoyen, L. *J. Am. Chem. Soc.* **2004**, *126*, 6301-6313.

(10) (a) Dammer, S. J.; Solntsev, P. V.; Sabin, J. R.; Nemykin, V. N. *Inorg. Chem.* **2013**, *52,* 9496-9510. (b) Ray, A.; Bauri, A.; Bhattacharya, S. *Spectrochim.Acta A* **2015**, *134*, 566-573. (c) Reddy, B. K.; Gadekar, S. C.; Anand, V. G. *Chem. Commun.* **2015**, *51*, 8276-8279. (d) Mukherjee, S.; Bauri, A. K.; Bhattacharya, S. *Spectrochim. Acta A* **2013**, *115*, 835-839. (e) Bottari, G.; Trukhina, O.; Ince, M.; Torres, T. *Coord. Chem. Rev.* **2012**, *256*, 2453-2477. (f) Vecchi, A.; Galloni, P.; Floris, B.; Dudkin, S. V.; Nemykin, V. N. *Coord. Chem. Rev.* **2015**, *291*, 95-171. (g) Mukherjee, P.; Chattopadhyay, S.; Bhattacharya, S. *J. Porphyrins Phthalocyanines* **2012**, *16*, 14-24.

(11) (a) Sandanayaka, A. S. D.; Subbaiyan, N. K.; Das, S. K.; Chitta, R.; Maligaspe, E.; Hasobe, T.; Ito, O.; D'Souza, F. *ChemPhysChem* **2011**, *12*, 2266-2273. (b) Basiuk, V. A.; Contreras-Torres, F. F.; Bassiouk, M.; Basiuk, E. V. *J. Comput. Theor. Chem.* **2009**, *6*, 1383-1411. (c) Guldi, D. M. *Phys. Chem. Chem. Phys.* **2007**, *9*, 1400-1420. (d) Roquelet, C.; Langlois, B.; Vialla, F.; Garrot, D.; Lauret, J. S.; Voisin, C. *Chem. Phys.* **2013**, *413*, 45-54. (e) Bi, C.; Li, Y. J.; Chen, H. W.; Yin, G.; Zhu, J. J. *Chinese I. Chem.* **2012**, *30*, 1722-1728. (f) Bartelmess, J.; Ballesteros, B.; de la Torre, G.; Kiessling, D.; Campidelli, S.; Prato, M.; Torres, T.; Guldi, D. M. *J. Am. Chem. Soc.* **2010**, *132*, 16202-16211. (g) Maligaspe, E.; Sandanayaka, A. S. D.; Hasobe, T.; Ito, O.; D'Souza, F. *J. Am. Chem. Soc.* **2010**, *132*, 8158-8164. (h) D'Souza, F.; Maligaspe, E.; Karr, P. A.; Schumacher, A. L.; El Ojaimi, M.; Gros, C. P.; Barbe, J. M.; Ohkubo, K.; Fukuzumi, S. *Chem. Eur. J.* **2008**, *14*, 674-681.

(12) (a) Hochmuth, D. H.; Michel, S. L. J.; White, A. J. P.; Williams, D. J.; Barrett, A. G. M.; Hoffman, B. M. *Eur. J. Inorg. Chem.* **2000**, 593-596. (b) Eichhorn, D. M.; Yang, S. L.; Jarrell, W.; Baumann, T. F.; Beall, L. S.; White, A. J. P.; Williams, D. J.; Barreyy, A. G. M.; Hoffman, B. M. *J. Chem. Soc. Chem. Commun.* **1995**, 1703-1704.

(13) (a) Wrobel, D.; Boguta, A.; Mazurkiewicz, P. *Spectrochim. Acta. A* **2003**, *59*,

2841-54. (b) Kobayashi, N. *J. Chem. Soc., Chem. Commun.* **1991**, 1203-1205. (c) Yanagi, H.; Mukai, H.; Nair, M. *Thin Solid Films* **2006**, *499*, 123-128. (d) Xu, S.; Chen, K.; Tian, H. *J. Mater. Chem.* **2005**, *15*, 2676-2680. (e) Gonzalez-Rodriguez, D.; Claessens, C. G.; Torres, T.; Liu, S.; Echegoyen, L.; Vila, N.; Nonell, S. *Chem. Eur. J.* **2005**, *11*, 3881-3893. (f) Ohno-Okumura, E.; Sakamoto, K.; Kato, T.; Hatano, T.; Fukui, K.; Karatsu, T.; Kitamura, A.; Urano, T. *Dyes Pigments* **2002**, *53*, 57-65. (g) Rahman, G. M. A.; Lueders, D.; Rodriguez-Morgade, M. S.; Caballero, E.; Torres, T.; Guldi, D. M. *ChemSusChem* **2009**, *2*, 330-335. (h) Xu, H.; Ng, D. K. P. *Chem. Asian J.* **2009**, *4*, 104-110. (i) Diaz, D. D.; Bolink, H. J.; Cappelli, L.; Claessens, C. G.; Coronado, E.; Torres, T. *Tetr. Lett.* **2007**, *48*, 4657-4660. (j) Geyer, M.; Plenzig, F.; Rauschnabel, J.; Hanack, M.; Del Rey, B.; Sastre, A.; Torres, T. *Synthesis* **1996**, 1139-1151. (k) Medina, A.; Claessens, C. G.; Rahman, G. M. A.; Lamsabhi, A. M.; Mo, O.; Yanez, M.; Guldi, D. M.; Torres, T. *Chem. Commun.* **2008**, 1759-1761. (l) Xu, H.; Jiang, X.-J.; Chan, E. Y. M.; Fong, W.-P.; Ng, D. K. P. *Org. Biomol. Chem.* **2007**, *5*, 3987-3992. (m) Solntsev, P. V.; Spurgin, K. L.; Sabin, J. R.; Heikal, A. A.; Nemykin, V. N. *Inorg. Chem.* **2012**, *51*, 6537-6547. (n) Maligaspe, E.; Hauwiller, M. R.; Zatsikha, Y. V.; Hinke, J. A.; Solntsev, P. V.; Blank, D. A.; Nemykin, V. N. *Inorg. Chem.* **2014**, *53*, 9336-9347.

(14) (a) Cnops, K.; Rand, B. P.; Cheys, D.; Verreet, B.; Empl, M. A.; Heremans, P. *Nature Commun.* **2014**, *5,* 3406. (b) Menke, S. M.; Holmes, R. J. *ACS Appl. Mater. Interfaces* **2015**, *7*, 2912-2918. (c) Takao, Y.; Masuoka, T.; Yamamoto, K.; Mizutani, T.; Matsumoto, F.; Moriwaki, K.; Hida, K.; Iwai, T.; Ito, T.; Mizuno, T.; Ohno, T. *Tetr. Lett.***2014**, *55*, 4564-4567. (d) Verreet, B.; Cnops, K.; Cheyns, D.; Heremans, P.; Stesmans, A.; Zango, G.; Claessens, C.G.; Torres, T.; Rand, B. P. *Adv. Energy Materials* **2014**, *4*, 1301413. (e) Gu, J. Y.; Cui, B.; Chen, T.; Yan, H. J.; Wang, D.; Wan, L. J. *Langmuir* **2013**, *29*, 264-270. (f) Kulshreshtha, C.; Kim, G. W.; Lampande, R.; Huh, D. H.; Chae, M.; Kwon, J. H. *J. Mater. Chem. A* **2013**, *1*, 4077-4082. (g) Ma, B. W.; Woo, C. H.; Miyamoto, Y.; Frechet, J. M. J. *Chem. Mater.* **2009**, *21*, 1413-1417. (h) Verreet, B.; Schols, S.; Cheyns, D.; Rand, B. P.; Gommans, H.; Aernouts, T.; Heremans, P.; Genoe, J. *J.Mater. Chem.* **2009**, *19*, 5295-5297.

(15) Camerel, F.; Ulrich, G.; Retailleau, P.; Ziessel, R. *Angew. Chem., Int .Ed.* **2008**, *47*, 8876-8880.

(16) Sanchez-Molina, I.; Claessens, C. G.; Grimm, B.; Guldi, D. M.; Torres, T. *Chem. Sci.* **2013**, *4*, 1338-1344.

(17) Denis, P. A. *New. J. Chem.* **2014**, *38*, 5608-5616.

(18) Claessens, C. G.; Medina, A.; Torres, T. *Abstracts, ICPP-8*, **2014**, Istanbul, Turkey.

(19) Konarev, D. V.; Troyanov, S. I.; Lyubovskaya, R. N. *CrystEngComm* **2015**, *17*, 3923-3926.

(20) (a) Lukyanets, E. A., Nemykin, V. N. *J. Porphyrins Phthalocyanines* **2010**, *14*, 1 - 40. (b) Nemykin, V. N.; Lukyanets, E. A. in: *Handbook of Porphyrin Science*, K. M. Kadish, K. M. Smith and R. Guilard (Eds.); World Scientific: Singapore, **2010**, *Vol 3*, pp 1 - 323. (c) Kobayashi, N.; Ogata, H.; Nonaka, N.; Luk'yanets, E. A. *Chem. Eur. J.*

2003, *9*, 5123-5134.

(21) (a) Lamsabhi, A.; Yanez, M.; Mo, O.; Trujillo, C.; Blanco, F.; Alkorta, I.; Elguero, J.; Caballero, E.; Rodriguez-Morgade, M. S.; Claessens, C.G.; Torres, T. *J. Porphyrins Phthalocyanines* **2011**, *15*, 1220-1230. (b) Gao, Y.; Solntsev, P. V.; Nemykin, V. N. *J. Mol. Graphics Modelling* **2012**, *38*, 369-374. (c) Mack, J.; Otaki, T.; Durfee, W. S.; Kobayashi, N.; Stillman, M. J. *J. Inorg. Biochem.* **2014**, *136*, 122-129. (d) Ferro, V. R.; de la Vega, J. M. G.; Gonzalez-Jonte, R. H.; Poveda, L. A. *J. Mol. Struct. - THEOCHEM* **2001**, 537, 223-234.

(22) Sastre, A.; Torres, T.; DiazGarcia, M. A.; Agullo-Lopez, F.; Dhenaut, C.; Brasselet, S.; Ledoux, I.; Zyss, J. *J. Am. Chem. Soc.* **1996**, *118*, 2746-2747.

(23) Nonell, S.; Rubio, N.; del Rey, B.; Torres, T. *J. Chem. Soc. Perkin Trans 2* **2000**, *6*, 1091-1094.

(24) (a) Sakamoto, K.; Ohno-Okumura, E. *Materials* **2009**, *2*, 1127-1179 (b) Spurgin, K. L. *M.S. Thesis* **2013**, University of Minnesota Duluth, pp. 1 -126.

(25) Gaussian 09, Revision **A.1**, Frisch, M. J.; Trucks, G. W.; Schlegel, H. B.; Scuseria, G. E.; Robb, M. A.; Cheeseman, J. R.; Scalmani, G.; Barone, V.; Mennucci, B.; Petersson, G. A.; Nakatsuji, H.; Caricato, M.; Li, X.; Hratchian, H. P.; Izmaylov, A. F.; Bloino, J.; Zheng, G.; Sonnenberg, J. L.; Hada, M.; Ehara, M.; Toyota, K.; Fukuda, R.; Hasegawa, J.; Ishida, M.; Nakajima, T.; Honda, Y.; Kitao, O.; Nakai, H.; Vreven, T.; Montgomery, Jr., J. A.; Peralta, J. E.; Ogliaro, F.; Bearpark, M.; Heyd, J. J.; Brothers, E.; Kudin, K. N.; Staroverov, V. N.; Kobayashi, R.; Normand, J.; Raghavachari, K.; Rendell, A.; Burant, J. C.; Iyengar, S. S.; Tomasi, J.; Cossi, M.; Rega, N.; Millam, N. J.; Klene, M.; Knox, J. E.; Cross, J. B.; Bakken, V.; Adamo, C.; Jaramillo, J.; Gomperts, R.; Stratmann, R. E.; Yazyev, O.; Austin, A. J.; Cammi, R.; Pomelli, C.; Ochterski, J. W.; Martin, R. L.; Morokuma, K.; Zakrzewski, V. G.; Voth, G. A.; Salvador, P.; Dannenberg, J. J.; Dapprich, S.; Daniels, A. D.; Farkas, Ö.; Foresman, J. B.; Ortiz, J. V.; Cioslowski, J.; Fox, D. J. Gaussian, Inc., Wallingford CT, 2009.

(26) Yanai, T.; Tew, D.; Handy, N. *Chem. Phys. Lett.* **2004**, *393*, 51-57.

(27) Chai, J.-D.; Head-Gordon, M. *Phys. Chem. Chem. Phys.* **2008**, *10*, 6615-6620.

(28) Tao, J. M.; Perdew, J. P.; Staroverov, V. N.; Scuseria, G. E. *Phys. Rev. Lett.* **2003**, *91*, 146401.

(29) Zhao, Y.; Truhlar, D. G. *Theor. Chem. Acc.* **2008**, *120*, 215-241.

(30) Zhao, Y.; Truhlar, D. G. *J. Phys. Chem.* **2006**, *110*, 5121-5129.

(31) (a) Hehre, W. J.; Ditchfield, R.; Pople, J. A. *J. Chem. Phys.* **1972**, *56*, 2257. (b) Gordon, M. S.; Binkley, J. S.; Pople, J. A.; Pietro, W. J.; Hehre, W. J. *J. Am. Chem. Soc.* **1982**, *104*, 2797-2803. (c) Binning Jr., R. C.; Curtiss, L. A. *J. Comp. Chem.* **1990**, *11*, 1206-1216. (d) Hariharan, P. C.; Pople, J. A. *Theor. Chem. Acc.* **1973**, *28*, 213-222.

(32) Tenderholt, A. L. *QMForge, Version 2.1.* Stanford University, Stanford, CA,

USA.

(33) Otwinowski, Z.; Minor, W. *Methods in Enzymology*, New York: Academic Press; **1997**. Vol. 276, Carter Jr, C. W.; Sweet, R. M. (Eds.), pp. 307—326.

(34) Altomare, A.; Cascarano, G.; Giacovazzo, C.; Guagliardi, A.; Burla, M. C.; Polidori, G.; Camalli, M. *J. Appl. Cryst.* **1994**, *27,* 435.

(35) Oszlanyi G., Suto A. *Acta Crystallogr.* **2004**, *A60*, 134-141.

(36) Betteridge, P. W., Carruthers, J. R., Cooper, R. I., Prout, K., Watkin, D. J. *J. Appl. Cryst.*, **2003**, 36, 1487.

(37) (a) Sheldrick, G. M. *Acta Cryst.* **2008**, *A64*, 112-122. (b) Hübschle, C. B., Sheldrick, G. M., Dittrich, B. *J. Appl. Cryst.*, **2011**, *44*, 1281-1284.

(38) Spek, A. L. *Acta Cryst.* **2009**, *D65*, 148-155.

(39) Underwood, D. F.; Blank, D. A. *Journal of Physical Chemistry A*, **2003**, *107*, 956–961.

(40) (a) Del Rey, B.; Keller, U.; Torres, T.; Rojo, G.; Agullo-Lopez, F.; Nonell, S.; Marti, C.; Brasselet, S.; Ledoux, I.; Zyss, J. *J. Am. Chem. Soc.* **1998**, *120*, 12808-12817. (b) Kasuga, K.; Idehara, T.; Handa, M.; Ueda, Y.; Fujiwara, T.; Isa, K. *Bull. Chem. Soc. Japan* **1996**, *69*, 2559-2563. (c) Gonzalez-Rodriguez, D.; Torres, T.; Denardin, E. L. G.; Samios, D.; Stefani, V.; Correa, D. S. *J. Organomet. Chem.* **2009**, *694*, 1617-1622. (d) Morse, G. E.; Paton, A. S.; Lough, A.; Bender, T. P. *Dalton Trans.* **2010**, 3915 – 3922. (e) Lapok, L.; Claessens, C. G.; Woehrle, D.; Torres, T. *Tetr. Lett.* **2009**, *50*, 2041-2044. (f) Claessens, C. G.; Gonzalez-Rodriguez, D.; del Rey, B.; Torres, T.; Mark, G.; Schuchmann, H.-P.; von Sonntag, C.; MacDonald, J. G.; Nohr, R. S. *Eur. J. Org. Chem.* **2003**, 2547-2551. (g) Guilleme, J.; Gonzalez-Rodriguez, D.; Torres, T. *Angew. Chem., Int. Ed.* **2011**, *50*, 3506-3509. (h) Potz, R.; Goldner, M.; Huckstadt, H.; Cornelissen, U.; Tutass, A.; Homborg, H. *Z. Anorg. Allg. Chem.* **2000**, *626*, 588-596. (i) Engel, M. K.; Yao, J.; Maki, H.; Takeuchi, H.; Yonehara, H.; Pac, C.; *Report of Kawamura Institute of Chem. Res.*, **1997**, *9,* 53-128. (j) Tippmann, E. M.; Schultz, P. G. *Tetrahedron* **2007**, *63*, 6182-6184. (k) Kato, T.; Tham, F. S.; Boyd, P. D. W.; Reed, C. A. *Heteroatom Chem.* **2006**, *17*, 209 – 216.

(41) (a) Lee, M. H.; Geva, E.; Dunietz, B. D. *J. Phys. Chem. C* **2014**, *118*, 9780-9789. (b) Wilcox, D. E.; Lee, M. H.; Sykes, M. E.; Niedringhaus, A.; Geva, E.; Dunietz, B. D.; Shtein, M.; Ogilvie, J. P. *J. Phys. Chem. Lett.* **2015**, *6*, 569-575.

(42) Schalley, C. A.; Springer, A. *Mass Spectrometry of Non-Covalent Complexes: Supramolecular Chemistry in the Gas Phase* 1st Ed., Wiley, New York, **2009**, pp. 1-571.

(43) Wang, Y.-B.; Lin, Z. *J. Am. Chem. Soc.* **2003**, *125*, 6072-6073.

(44) (a) Jung, S.; Seo, J.; Shin, S. K. *J. Phys. Chem. A* **2010**, *114,* 11376-11385. (b) Jung, S.; van Paauwe, J. D.; Boyd, P. D. W.; Shin, S. K. *Phys. Chem. Chem. Phys.* **2011**, *13*, 20248-20254.

(45) (a) Claessens, C. G.; Gonzalez-Rodriguez, D.; Torres, T. *Chem. Rev.* **2002**, *102*, 835-853. (b) Claessens, C. G.; Gonzalez-Rodriguez, D.; Rodriguez-Morgade, M. S.; Medina, A.; Torres, T. *Chem. Rev.* **2014**, *114*, 2192-2277. (c) Kobayashi, N. in: The Porphyrin Handbook. Kadish, K. M.; Smith, K. M.; Guilard, R. (Eds.), Academic Press, New York, 2003, Vol 15, pp 161 – 262.

(46) Fukuda, T.; Kobayashi, N. in: *Handbook of Porphyrin Science*, Kadish, K. M.; Smith, K. M.; Guilard, R. (Eds.), World Scientific, Singapore, **2010**, *9*, pp. 1-644.

(47) (a) Arbogast, J. W.; Foote, C. S.; Kao, M. *J. Am. Chem. Soc.* **1992**, *114*, 2277-2279. (b) Watanabe, A.; Ito, O. *J. Phys. Chem.* **1994**, *98*, 7736-7740. (c) Horie, R.; Araki, Y.; Ito, O.; Lee, Y.; Kitagawa, T.; Komatsu, K. *J. Phys. Chem. A* **2005**, *109*, 6140-6146.

(48) Mahyuddin, M. H.; Belosludov, R. V.; Khazaei, M.; Mizuseki, H.; Kawazoe, Y. *J. Phys. Chem. C* **2011**, *115*, 23893-23901.